# Building, Testing and Modelling of a Pulse Tube Cryogenic Cooler

by
GR Smith


Supervisor Mr RT Dobson

Thesis presented in partial fulfilment of the requirements for the degree in Master of Science in Engineering at the University of Stellenbosch

December 2006

Department of Mechanical and Mechatronic Engineering

University of Stellenbosch

## DECLARATION

I, the undersigned, hereby declare that the work contained in this thesis is my own original work and has not previously, in its entirety or in parts been submitted at any University or institution for a degree.

Date: 08/12/2006

## SUMMARY

Pulse tube cryogenic coolers (cryocoolers) are among the latest innovations of cryogenic coolers. They fall in the same category as the reversed Stirling cycle cryocoolers that have been used for decades to cool infrared detectors in military and space applications. Pulse tube cryocoolers will replace most of the Stirling cryocoolers in future applications, because they have no moving parts at its cold point and therefore are subject to less vibrations, and hence has a longer service life.

Pulse tube coolers, like domestic refrigerators, are also driven by a compressor. The type of compressor used in this project is of the reciprocating type which is driven by a linear, resonant motor which is similar to a loudspeaker mechanism. This project is about the building, testing and mathematical modelling of a pulse tube cryogenic cooler.

The pulse tube cryocooler and its reciprocator (reciprocating compressor) was designed and manufactured. Numerous tests were conducted to evaluate the reciprocator. A complete mathematical model is presented for the reciprocator which was compared with the data obtained from the tests. The pulse tube cryocooler was modelled with a one-dimensional, time dependant CFD (computational fluid dynamics) model by solving the discretized conservation equations which were derived in this project from first principles. The discussions and conclusions regarding these results are presented, together with recommendations for future work.

## OPSOMMING

Pulsbuis kreogeniese koelers (kreokoelers) is een van die nuutste innovasies van kreogeniese koelers. Hul val in dieselfde kategorie as die verkeerdom Stirling siklus kreogeniese koelers wat al vir dekades in gebruik is vir die verkoeling van infrarooi detektors in militêre en buiteruim toepassings. Pulsbuis kreogeniese koelers sal Stirling koelers in die toekoms vervang omdat hul geen bewegende dele in hul koue punt het nie. Gevolglik het hul 'n langer werkings lewe en veroorsaak hulle baie minder vibrasies.

Net soos huishoudelike koelers het pulsbuis koelers ook 'n kompressor. Die tipe kompressor wat gebruik is in hierdie projek is van die resiprokeerende soort wat gedryf word deur 'n lineêre, resonante motor soortgelyk aan 'n luidspreker meganisme. Hierdie projek handel oor die bou· toets en wiskundige modelering van 'n pulsebuis kreogeniese koeler asook sy resiprokeerende kompressor (resiprokeerder).

Die pulsbuis kreokoeler en sy resiprokeeder was ontwerp en vervaardig en verskeie toetse was daarop uitgevoer. 'n Volledige wiskundige model is ontwikkel vir die resiprokeerder wat vergelyk was met die toets resultate. Die pulsbuis kreokoeler was gemodeleer met 'n een dimensionele, tyd afhanklike, NV (numeriese vloeimeganika) program. In hierdie program word die behoudsvergelykings opgelos wat van eerste beginsels afgelei is. Besprekings en gevolgtrekkings word gemaak na gelang van die resultate en waarnemings asook toekomstige voostellings vir verdere navorsings werk.

## ACKNOWLEDGEMENTS

I would like to thank and acknowledge a few people for their support and guidance during this project. A special thanks to my parents for supporting and believing in me. Many thanks to my supervisor, Mr Dobson, for his guidance and friendship. Thank you to Prof Harms for his support and many helpful discussions. On the technical side I would like to thank the personnel of SMD for the excellent manufacturing and Peter Bruins for all his helpful suggestions. Thanks to Cobus Zietsman for his assistance during testing and manufacturing. And lastly, but most importantly, I would like to thank my God, Jesus Christ, in whom all things are possible.

# TABLE OF CONTENTS

Declaration ..... i

Summary ..... i

Opsomming ..... ii

Acknowledgements ..... iii

Table of Contents ..... iv

List of Figures ..... vi

Nomenclature ..... ix

Nomenclature ..... ix

1 Introduction ..... 1.1

1.1 Cryocoolers ..... 1.1
1.2 Stirling Cooling ..... 1.2
1.3 Pulse Tube Cooling ..... 1.3
1.4 Stirling Type Reciprocators ..... 1.9
1.5 Applications ..... 1.10
1.6 Introduction to this Thesis ..... 1.11

2 Cryocooler Design ..... 2.1

2.1 Reciprocator Design ..... 2.1
2.2 Cold Finger Design ..... 2.6
2.3 Manufacturing Considerations ..... 2.9

3 Mathematical Modelling ..... 3.1

3.1 Reciprocator ..... 3.1
3.2 Cold Finger ..... 3.8
3.3 Cooling of Electronics ..... 3.12

4 One-dimensional CFD Simulation ..... 4.1

4.1 Model ..... 4.1
4.2 Algorithm ..... 4.4
4.3 Verification and Convergence ..... 4.6
4.4 Results ..... 4.7

5 Experimental Evaluation ..... 5.1

5.1 Reciprocator Characteristics ..... 5.1
5.2 Reciprocator Performance ..... 5.9
5.3 Cooler Performance ..... 5.13
6 Discussions and Conclusions ..... 6.1
6.1 Reciprocator ..... 6.1
6.2 Cold Finger ..... 6.7
7 References ..... 7.1

Appendix A: Derivation of Conservation Equations
Appendix B: Discretization of Conservation Equations

# LIST OF FIGURES

**Figure 1.1** Schematic of Stirling cryocooler ..... 1.3
**Figure 1.2** Schematic of a pulse tube ..... 1.3
**Figure 1.3** Schematic of a basic pulse tube refrigerator (BPTR) ..... 1.3
**Figure 1.4** Schematic of the orifice pulse tube refrigerator (OPTR) ..... 1.4
**Figure 1.5** Schematic of the double inlet orifice pulse tube refrigerator .... 1.4
**Figure 1.6** Schematic of an inertance pulse tube refrigerator (IPTR) ..... 1.5
**Figure 1.7** Schematic of the GM type orifice pulse tube refrigerator ..... 1.5
**Figure 1.8** Idealized form of the pressure in a GM pulse tube refrigerator 1.6
**Figure 1.9** Temperature and pressure versus position in the regenerator, hot heat exchanger and pulse tube for a gas particle during one cycle ..... 1.8
**Figure 2.1** Exploded isometric view of linear motor ..... 2.2
**Figure 2.2** Pictures of moving plunger ..... 2.2
**Figure 2.3** Picture of stationary magnet assembly attached to the outer cylinder ..... 2.3
**Figure 2.4** Diagram showing flux paths of magnetic circuit ..... 2.3
**Figure 2.5** Diagram showing right hand rule ..... 2.4
**Figure 2.6** Exploded isometric view of the linear bearing system ..... 2.5
**Figure 2.7** Parts of Flexure bearing ..... 2.5
**Figure 2.8** Displaced flexure unit during testing ..... 2.6
**Figure 2.9** Schematic of pulse tube cooler ..... 2.7
**Figure 2.10** Exploded isometric view of the cold finger (pulse tube, regenerator tube and cold heat exchanger) ..... 2.7
**Figure 2.11** Picture of a cut pulse tube ..... 2.8
**Figure 2.12** Exploded view of reservoir and cold finger base ..... 2.8
**Figure 2.13** (a) Regenerator mesh sheets, (b) interchangeable inertance tube ..... 2.9
**Figure 2.14** Picture showing cryocooler being charged with helium ..... 2.10
**Figure 3.1** Schematic presentation of reciprocator connected to a compression chamber showing all the forces acting on the moving plunger ..... 3.1
**Figure 3.2** Schematic presentation of reciprocator connected to a compression chamber showing linear motor dimensions .... 3.4

**Figure 3.3** Operating point of the NdFeB magnet (grade N42) on its demagnetization curve (magnetomotive force versus flux density) (Organ, 1999) ..... 3.5
**Figure 3.4** Schematic of the piston and compression space ..... 3.7
**Figure 3.5** Schematic of a pulse tube cold finger integrated with a spherical approximated multi chip module ..... 3.12
**Figure 3.6** Thermal resistance diagram for heat flow from the environment to the MCM ..... 3.13
**Figure 3.7** Schematic showing two concentric spheres..... 3.15
**Figure 4.1** One dimensional staggered grid ..... 4.2
**Figure 4.2** Schematic of an inertance pulse tube refrigerator (IPTR) ..... 4.2
**Figure 4.3** Flow chart of the solving process of the CFD simulation..... 4.5
**Figure 4.4** Numerical grid of pulse tube cooler model ..... 4.6
**Figure 4.5** Temperature versus position for converged solutions in regenerator for various numbers of regenerator cells, 40, 30, 20 and 10 ..... 4.7
**Figure 4.6** Pressure and velocity versus time of the gas particle inside the cooler during one cycle. ..... 4.8
**Figure 4.7** Diameter, time, pressure and temperature versus position in the regenerator and pulse tube for a gas particle during one cycle ..... 4.9
**Figure 4.8** Velocity, pressure, density and temperature versus position in the regenerator and pulse tube at an instance after some cooling has taken place..... 4.11
**Figure 4.9** Normalized pressure and velocity versus time for the gas inside the cold heat exchanger..... 4.12
**Figure 5.1** Vertical and horizontal flexure testing setup..... 5.2
**Figure 5.2** Force-displacement curve for linear bearings ..... 5.3
**Figure 5.3** Forces diagram of the moving plunger..... 5.3
**Figure 5.4** Linear motor testing setup in vertical and horizontal positions 5.4
**Figure 5.5** Calculated flux density versus piston position..... 5.4
**Figure 5.6** Voltage and current wave forms for an inductive circuit..... 5.5
**Figure 5.7** Coil inductance testing setup ..... 5.6
**Figure 5.8** Graph showing coil inductance versus frequency ..... 5.6
**Figure 5.9** Strain gauge calibration curve for displacement ..... 5.7

**Figure 5.10** Generated voltage test setup ..... 5.8
**Figure 5.11** Displacement and generated voltage versus time for hand-moved plunger ..... 5.9
**Figure 5.12** Graphs of displacement and current versus time for a frequency of 10Hz and a maximum voltage of 8.5 V ..... 5.10
**Figure 5.13** Graphs of displacement and current versus time for a frequency of 15Hz and a maximum voltage of 12V ..... 5.10
**Figure 5.14** Testing setup for reciprocator performance testing ..... 5.11
**Figure 5.15** Absolute pressure versus time for a frequency of 10 Hz and applied voltage of 10.6 V ..... 5.12
**Figure 5.16** Absolute pressure versus time for a frequency of 20 Hz and applied voltage of 9.6 V ..... 5.12
**Figure 5.17** Absolute pressure versus time for a frequency of 30 Hz and applied voltage of 9V ..... 5.13
**Figure 5.18** Picture of complete cryocooler during performance testing5.13
**Figure 5.19** Schematic of testing setup for cooler performance testing 5.14
**Figure 5.20** Picture of cooler performance testing setup ..... 5.14
**Figure 5.21** Cool-down curve of cryocooler for 20 Hz with inertance tube of diameter 0.6 mm and length 30 mm ..... 5.15
**Figure 5.22** Cool-down curve of cryocooler driven at 15, 20 and 25 Hz with inertance tube of diameter 0.6 mm length 20 mm ..... 5.15
**Figure 6.1** Diagram showing the directions of the magnetic flux in moving core ..... 6.2
**Figure 6.2** Absolute pressure versus time for a frequency of 10 Hz and 10 W input power ..... 6.3
**Figure 6.3** Absolute pressure versus time for a frequency of 20 Hz and 10 W input power ..... 6.4
**Figure 6.4** Absolute pressure versus time for a frequency of 30 Hz and 10 W input power ..... 6.4
**Figure 6.5** Pressure amplitude (a) and loss factor (b) versus frequency .. 6.5
**Figure 6.6** Voltage amplitude (a) and current amplitude (b) versus frequency for an input power of 10 W ..... 6.5
**Figure 6.7** Graph showing optimal operating point of a magnet ..... 6.7
**Figure 6.8** Picture of cryocooler cold zone during operation ..... 6.8

# NOMENCLATURE

| | |
|---|---|
| $\mathfrak{R}$ | magnetic reluctance, At/Wb |
| $\mathfrak{I}$ | magnetomotive force, At |
| $A$ | area, $m^2$ |
| $B$ | magnetic flux density, T |
| $\overline{B}$ | magnetic flux density averaged over area, T |
| $C_f$ | friction coefficient |
| $c$ | specific heat, J/kgK |
| $c_p$ | isobaric specific heat of gas, J/kgK |
| $c_v$ | isochoric specific heat of gas, J/kgK |
| $d$ | diameter, m |
| $E$ | energy, J |
| $e_v$ | void fraction |
| $F$ | force, N |
| $f$ | frequency, Hz |
| $f$ | friction coefficient |
| $g$ | gravitational acceleration, $kg/ms^2$ |
| $H$ | magnetic field strength, A/m |
| $h$ | heat transfer coefficient, $W/m^2K$ |
| $h$ | enthalpy, J/kg |
| $i$ | current, A |
| $i$ | internal energy, J |
| $K$ | leakage factor |
| $k$ | spring constant, N/m |
| $k$ | thermal conductivity, W/mK |
| $k$ | specific heat ratio |
| $L$ | inductance, H |
| $\ell$ | length, m |
| $m$ | mass, kg |
| $m$ | matrix |
| $\dot{m}$ | mass flow rate, kg/s |
| $N$ | number of turns, t |
| $N$ | north |
| $P$ | pressure, Pa |

| | | |
|---|---|---|
| $Pr$ | Prantl number | $Pr = \frac{c_p \mu}{k}$ |
| $\dot{Q}$ | heat flow rate, W | |
| $R$ | electrical resistance, $\Omega$ | |
| $R$ | ideal gas constant for helium, J/kgK | |
| $r$ | radius, m | |
| $Re$ | Reynolds number | $Re = \frac{\rho u d}{\mu}$ |
| $S$ | surface area, $m^2$ | |
| $S$ | south | |
| $St$ | Stanton number | $St = \frac{h_m}{c_p u \rho}$ |
| $T$ | temperature, K | |
| $t$ | time, s | |
| $u$ | velocity, m/s | |
| $V$ | voltage, V volume, $m^3$ | |
| $W$ | work, J | |
| $x$ | displacement, m | |

**Greek symbols**

| | |
|---|---|
| $\mu_0$ | permeability of free space $4\pi \times 10^{-7}$ H/m |
| $\mu$ | dynamic viscosity, kg/ms |
| $\phi$ | magnetic flux, Wb |
| $\rho$ | density, $kg/m^3$ |
| $\nu$ | specific volume, $m^3/kg$ |
| $\Delta$ | spatial difference operator |

**Subscripts**

| | |
|---|---|
| *0* | initial |
| *MCM* | multi chip module |
| *MLI* | multilayer insulation |
| *a* | ambient |
| *b* | boundary |
| *bp* | back-pressure |
| *c* | cross sectional, conduction |
| *cf* | cold finger |
| *cu* | copper |

| | |
|---|---|
| *e* | enclosure |
| *e* | environment |
| *ex* | external |
| *f* | flow |
| *f* | friction |
| *g* | gap, gas |
| *h* | hydraulic |
| *i* | inside |
| *in* | internal |
| *m* | magnetic, matrix |
| *mt* | matrix and tube (gas surroundings) |
| *max* | maximum |
| *n* | natural |
| *o* | outside |
| *p* | piston |
| *pp* | piston-pressure |
| *r* | radiation |
| *reg* | regenerator |
| *s* | spring |
| *t* | tube |
| *w* | wire, wetted |

**Abbreviations**

| | |
|---|---|
| AC | alternating current |
| BPTR | basic pulse tube refrigerator |
| CFD | computational fluid dynamics |
| DC | direct current |
| DIOPTR | double inlet orifice pulse tube refrigerator |
| EMI | electromagnetic interference |
| FEM | finite element methods |
| GM | Gifford-McMahon |
| HTS | high temperature superconducting |
| hx | heat exchanger |
| IPTR | inertance pulse tube refrigerator |
| MCM | multi-chip module |

| | |
|---|---|
| MLI | multi layer insulation |
| MTBF | mean time between failures |
| OPTR | orifice pulse tube refrigerator |
| PTR | pulse tube refrigerator |
| RF | radio frequency |
| RMS | root mean square |
| SQUID | superconductive quantum interference device |
| TDMA | Thomas tri-diagonal matrix algorithm |

# 1 INTRODUCTION

The Pulse tube cryogenic cooler (cryocooler) operates with a closed gas cycle. It has no moving parts at its cooling point and therefore has low levels of vibration and electromagnetic noise. The Stirling-type pulse tube cryocoolers have very long maintenance-free operation when driven with a frictionless free-piston reciprocator. This makes the pulse tube cryocooler one of the best suited cryocoolers for the cooling of sensitive electronic devices in military, space and other applications.

## 1.1 Cryocoolers

There are many types of cryocoolers each specified in terms of its cooling power and cold tip temperature. These cryocoolers are application specific because every application requires a cryocooler to fit a different set of specifications. Some of the important specifications are: size, weight, cost, vibrations at cold point, efficiency, cooling power, cold point temperature, operating environment, reliability and electromagnetic interference.

Cryocoolers can be classified as either recuperative or regenerative (Radebaugh, 2000). Recuperative cryocoolers use only recuperative heat exchangers and operate with a steady flow of working fluid through the system. The compressor operates with a fixed inlet pressure and a fixed outlet pressure. If the compressor is a reciprocating type, it must have inlet and outlet valves to provide steady flow. The most common recuperative refrigerator is the Joule-Thompson refrigerator which is used in domestic applications.

The regenerative cryocoolers use at least one regenerative heat exchanger, or regenerator, and operate with oscillating flow and pressure. Regenerative cryocoolers are analogues to AC electrical systems, whereas the recuperative cryocoolers are analogues to DC electrical systems. In such an analogy, pressure is analogous to voltage, and mass flow or volume flow is analogous to current (Radebaugh, 2000).

In a regenerator, hot incoming gas transfers heat to the matrix of the regenerator, where the heat is stored for a half cycle in the heat capacity of the matrix. In the second half of the cycle, the returning cold gas, flowing in the opposite direction through the same channel, picks up heat from the matrix and returns the matrix to its original temperature before the cycle is repeated. At equilibrium, one end of the regenerator is at room temperature while the other end is at the cold temperature. Enhanced heat transfer is obtained in regenerators through the use of stacked fine-mesh screens or packed spheres because of their large surface areas. The most common regenerative cryocoolers are Stirling and Pulse Tube cryocoolers which will be discussed in sections 1.2 and 1.3.

## 1.2 Stirling Cooling

The Stirling cycle was invented by Robert Stirling in 1815 and was first utilized as a driving mechanism. In 1834 John Herschel proposed its use as a refrigerator for the production of ice. It was not until about 1861 that Alexander Kirk put the concept of using the Stirling cycle as a refrigerator to practice. Air was used as the working fluid in these early regenerative systems. Very little development of Stirling coolers occurred until 1946 when a Stirling engine at the Philips Company in Holland was run in reverse using a motor and was found to liquefy air on the cold tip. This engine used helium as the working fluid. Research then began on the use of Stirling refrigerators and about ten years later it was used to cool an infrared sensor to about 80K (Radebaugh, 2000).

The Stirling cooler consists of a reciprocator and a cooler (cold finger). The reciprocator is a valve-less type compressor which generates pressure oscillations. The freestanding reciprocator is connected to the cold finger by a thin pipe, called a transfer tube (see figure 1.1). The cold finger consists of a regenerator, helical spring, and a moving displacer. The moving regenerator (displacer) is made out of cascaded sheets (discs) of very fine mesh or packed spheres.

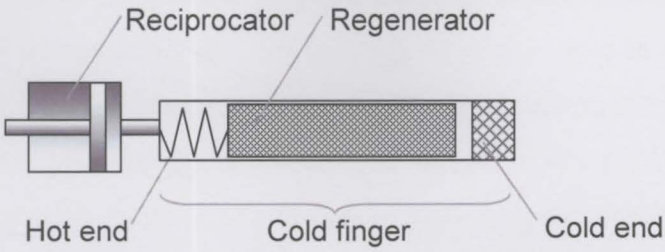


***Figure 1.1*** *Schematic of Stirling cryocooler*

## 1.3 Pulse Tube Cooling

Pulse Tubes are among the latest innovations of cryogenic coolers. Their development started at Syracuse University in 1964. Gifford and Longsworth observed that a metallic tube closed at one end, and the other end being connected to a pressure wave generator, increased in temperature at the closed end (Popescu, 2001). This device is known as the pulse tube and is shown in figure 1.2.

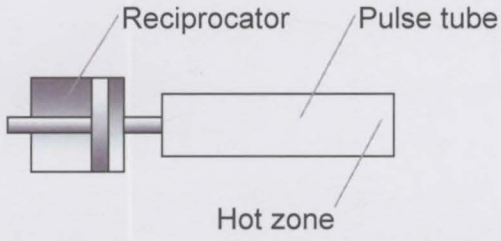


***Figure 1.2*** *Schematic of a pulse tube*

Further research undertaken at Syracuse University proved that placing a thermal regenerator between the reciprocator and the pulse tube causes an increase in temperature at the closed end (hot zone) in addition to cooling at the other end (cold zone). This concept was named Basic Pulse Tube Refrigerator (BPTR) (figure 1.3) and achieved a minimum temperature of 124K. However, it was found that the BPTR was too inefficient, and was abandoned as a useful cooler at the end of the sixties.

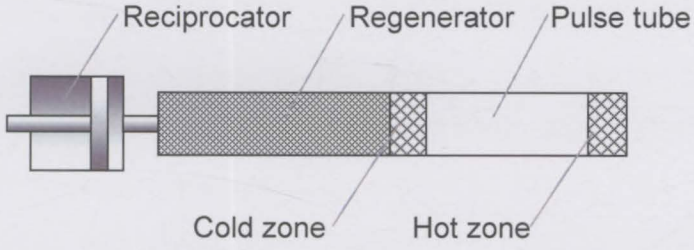


***Figure 1.3*** *Schematic of a basic pulse tube refrigerator (BPTR)*

A breakthrough for Pulse tube cryocoolers came in 1983, when Mikulin demonstrated that inserting an orifice and reservoir at the hot zone would increase the cooling efficiency of the cryocooler (Popescu, 2001). This led to the Orifice Pulse Tube Refrigerator (OPTR) which is shown in figure 1.4. The OPTR has become a standard technique for cryogenic cooling and between 1980 and 1994 temperatures between 30 and 3.6 K were reached using single and multiple stage systems.

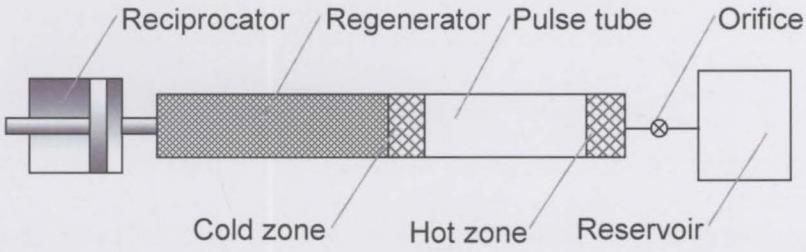


***Figure 1.4*** *Schematic of the orifice pulse tube refrigerator (OPTR)*

In 1990 Zhu (Radebaugh, 2000) increased the OPTR efficiency by adding a bypass with a second orifice between the pressure wave generator and the hot zone. This configuration is called the Double Inlet Orifice Pulse Tube Refrigerator (DIOPTR). The DIOPTR proved to be more efficient but it was found that it was not always reproducible for commercial purposes (Radebaugh, 2000). Figure1.5 shows a diagram of the major parts of a double inlet pulse tube refrigerator.

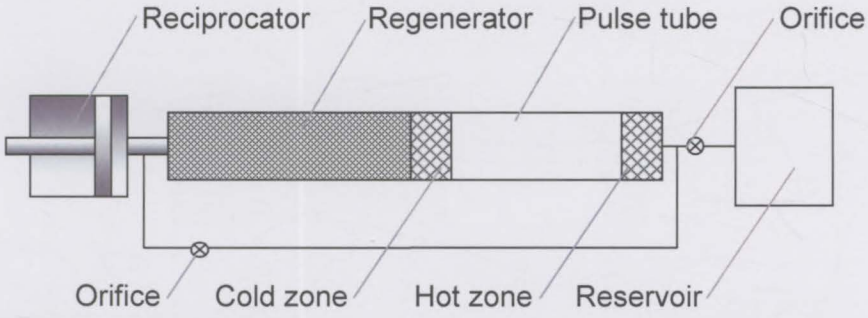


***Figure 1.5*** *Schematic of the double inlet orifice pulse tube refrigerator*

The latest innovation in pulse tube cryocoolers was reported by Zhu SW et al. (1997). It was shown that the performance of the pulse tube cryocooler can be improved by replacing the single orifice by a long thin tube (figure 1.6). The gas in the tube is subjected to inertia, and the resulting device has become known as the inertance pulse tube refrigerator (De Boer, 2002). As a result of

these improvements, pulse tube cryocoolers have become competitive with Stirling cryocoolers for many space and terrestrial applications (Radebaugh, 2000). The earliest use of an inertance pulse tube refrigerators seems to be Kanao (1994) who concluded that neither the single orifice nor the double inlet configuration provided better performance than the inertance configuration.

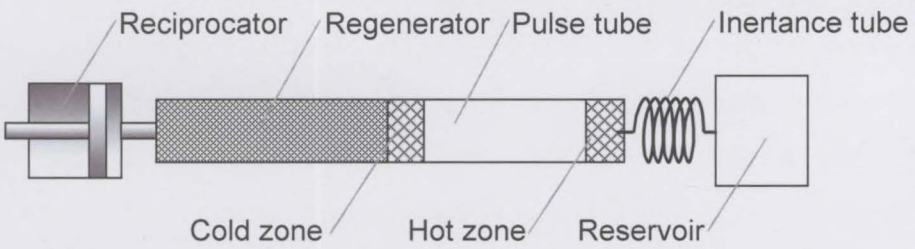


***Figure 1.6*** *Schematic of an inertance pulse tube refrigerator (IPTR)*

Pulse tube cryooolers can be classified according to the way their pressure oscillations are generated. According to this classification there are two main types of pulse tube cryocoolers. The first type is known as a Gifford-McMahon type (GM) pulse tube cryocooler. The GM compressor produces continuous high and low pressures (like a recuperative compressor) and makes use of a rotary valve to generate pressure oscillations. They use relatively high pressure ratios (1:5) and low frequencies (<5Hz) (Tanaeva, 2004). A schematic of the GM-type cryocooler is shown in figure 1.7.

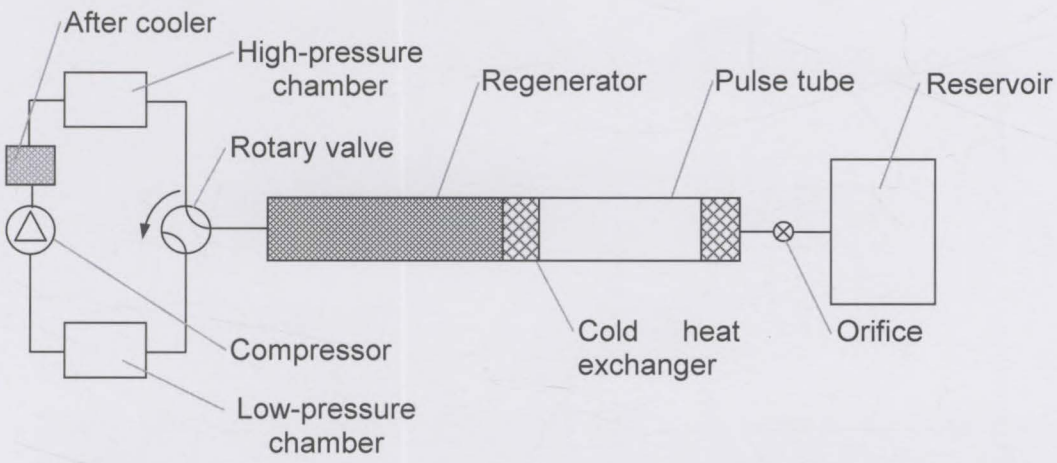


***Figure 1.7*** *Schematic of the GM type orifice pulse tube refrigerator*

The focus will be on the second type of Pulse Tube cryocoolers, known as high-frequency or Stirling type Pulse tube cryocoolers. They are driven by reciprocators which generate pressure oscillations within the pulse tube.

Stirling type pulse tube refrigerators use pressure ratios of between 1.2 and 1.4 and are charged with helium at pressures between 2 and 3 MPa. These reciprocators will be explained in section 1.4 in more detail.

### 1.3.1 Operating Principle of an Ideal GM Pulse Tube Refrigerator

The Pulse Tube cooling cycle is a closed cycle, and the operating principle of a GM-type pulse tube cryocooler (figure 1.7) will now be explained by making a few assumptions. The first assumption is that the pressure in the pulse tube is considered to be cyclic with a shape according to figure 1.8 (Tanaeva, 2004). The orifice is closed during phases 1 and 3 and open during phases 2 and 4. The reservoir is assumed to be infinitely large and therefore its pressure is constant and equal to a pressure which is equal to the charge pressure of the system. The processes in the tube are assumed to be adiabatic and therefore there is no heat transfer between the tube and the gas. There is also assumed to be no conduction within or along the tube. The heat exchangers are assumed to be perfect which means the temperature of the gas flowing out of the heat exchanger is equal to the temperature of the heat exchanger. The heat exchanger temperature is also taken as constant in the axial direction.

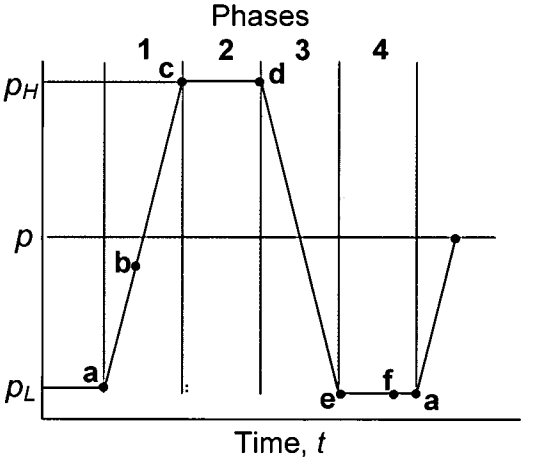


***Figure 1.8*** *Idealized form of the pressure in a GM pulse tube refrigerator*

*Phase1:* This is the compression phase of the cycle where the system is connected to the high-pressure chamber while the orifice is closed. The pressure in the pulse tube increases from the low pressure $p_L$ to the high pressure $p_H$.

*Phase2:* The orifice is opened. The pressure in the pulse tube is higher than the pressure in the reservoir and the gas flows from the pulse tube into the reservoir. The pressure in the system is constant and equal to $p_H$ during this phase because the system is still connected to the high-pressure chamber of the compressor.

*Phase3:* This is the expansion step where the system is connected to the low-pressure chamber while the orifice is closed. The pressure in the pulse tube decreases from the high pressure $p_H$ to the low pressure $p_L$.

*Phase4:* The orifice is opened again. The pressure in the reservoir is higher than the pressure in the tube and gas flows from the reservoir back into the tube. In this phase the pressure in the system is constant and equal to $p_L$ because the system is still connected to the low-pressure chamber of the compressor.

A gas particle will be followed in order to explain how cooling is generated during a cycle in the pulse tube cryocooler. This cycle starts after some cooling has occurred which means that the regenerator has a temperature gradient and the temperature of the cold heat exchanger is equal to $T_L$. The gas particle starts it cycle from within the generator (point **a** in figure 1.8 and 1.9).

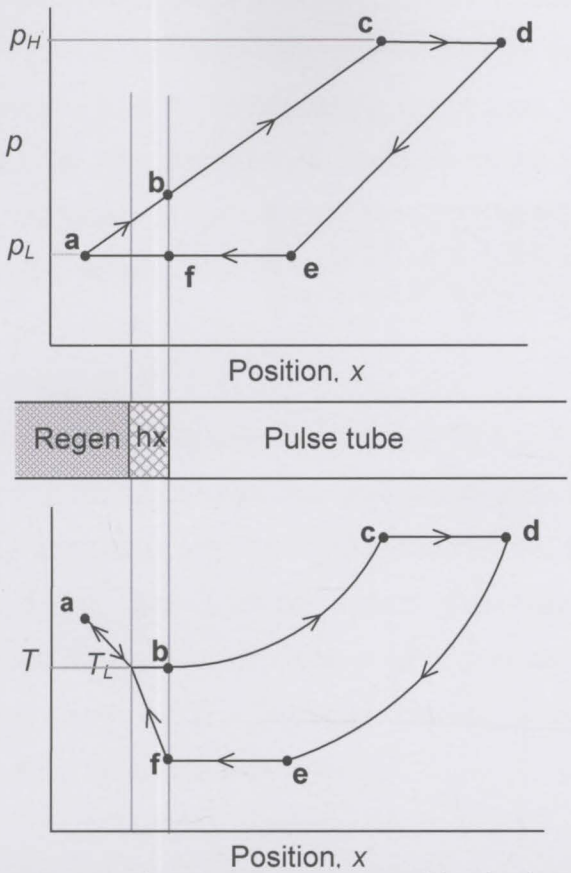


***Figure 1.9*** *Temperature and pressure versus position in the regenerator, hot heat exchanger and pulse tube for a gas particle during one cycle*

*Phase 1:* The gas particle moves from point **a** via **b** to point **c**. During the first part of the compression phase the gas particle moves through the regenerator towards the heat exchanger. This movement is due to the fact that the compressor is forcing more gas into the pulse tube. Work is done on the gas particle and its pressure increases while its temperature decreases due to heat exchange with the regenerator. The gas particle then leaves the heat exchanger and enters the tube at the temperature of $T_L$ at point **b**. From **b** to **c** the gas particle is adiabatically compressed, while it moves towards the orifice. The temperature of the gas particle then increases together with its pressure.

*Phase 2:* The gas particle moves from **c** to **d**, because gas flows from the tube into the reservoir. Its temperature is constant because its pressure is constant.

*Phase 3*: The gas particle moves from **d** to **e** and back toward the heat exchanger, because gas is removed from the system by the compressor. The gas particle is expanded and its temperature decreases. The gas particle is still inside the pulse tube after expansion, because of the flow which occurred in phase 2. The temperature of the particle is now lower than $T_L$, because of the heat rejection to the regenerator at the first part of the compression phase (phase 1).

*Phase 4:* The gas particle moves from **e** via **f** to **a**. The orifice is opened again and gas flows from the reservoir into the tube. From **e** to **f** the particle is still inside the tube and the pressure is constant therefore the temperature is also constant. At point **f** the gas particle enters the heat exchanger at a temperature lower that $T_L$ and therefore heat is absorbed by the gas particle and its temperature rises to $T_L$. The gas particle then moves into the regenerator back to its original starting point, **a**.

The function of the pulse tube is to insulate the processes at the two ends. It has to be large enough that gas flowing from the warm end traverses only part way through the pulse tube before flow is reversed. Likewise, flow from the cold end never reaches the warm end.

The operating principle of the non-ideal IPTR is somewhat more complex. The pressure wave created by the compressor is practically sinusoidal and the inertance tube is always open. The working of the IPTR relies on a phase shift between the pressure and the mass flow which is created by the inertance effect in the pulse tube. This phase shift mechanism and the working of the non-ideal IPTR will be explained later in chapter 4.

## 1.4 Stirling Type Reciprocators

The choice of gas compression method for a pulse tube cryocooler depends on the intended temperature range. In the case of this project where a single stage pulse-tube cryocooler is used for the 20 to 80 K temperature range the Stirling type compressor (reciprocator) is more appropriate (Tanaeva, 2004). It has a high efficiency which results in a lower total weight. The typical driving

frequency of the Stirling type PTR is 25-50 Hz. It was decided to only focus on the Stirling type reciprocator which was used in this project.

Reciprocators are currently built with two pistons situated on the same axis which operate with counter movements to neutralize the reciprocator vibration. The Oxford-type reciprocators make use of linear bearings called flexures to position the piston accurately during operation so that the piston does not touch the cylinder. This is also known as the free piston type reciprocator. The gap between the piston and cylinder has to be very small so that the leakage past the piston does not affect the pressure inside the pulse tube. This gap between the piston and cylinder in most reciprocators is in the order of 20 microns. These free-piston type reciprocators are known to have very long operation lifetimes of more than 5 years MTBF (Radebaugh, 2000).

The driving force behind the piston is produced by a linear motor which is similar to an audio speaker. The stiffness of the flexures together with the mass of the moving parts in the reciprocator determines the natural operating frequency of the system. The displacement amplitude of the piston in the reciprocator will be at a maximum at the natural frequency of the system. Reciprocators are therefore most efficient when driven at their natural frequencies. Chan, C K and Nguyen, T (1998) reported a reciprocator with an efficiency of 90%, which is electrical power converted to PV work.

## 1.5 Applications

Pulse tube cryocooler technology is relatively new. The specific properties of the pulse tube cryocooler, namely low vibrations and electromagnetic noise makes it possible to use in a variety of applications. Pulse tube cryocoolers will therefore replace most Stirling cryocoolers in future applications. Multiple stage pulse tube cryocoolers can reach temperatures below 4 K which brings about new applications (Xu, et al., 1999) (Wang and Thummes, 1997). This project will only focus on the applications of single stage pulse tube cryocoolers with a cooling temperature of about 70 K.

The latest application for cryocoolers and IPTR is the cooling of high temperature superconducting (HTS) devices which has to be cooled to about

77K. One of these is a SQUID (Superconducting Quantum Interference Device) which is the most sensitive device for measuring magnetic fields (Lienerth, et al., 2000). Rijpma et al. (2000) successfully constructed and tested a heart monitor which measured the magnetic fields of the human heart with SQUIDs. These SQUIDs where cooled by two Stirling cryocoolers because pulse tube cryocoolers where not readily available yet. The other superconducting application of pulse tube cryocoolers is the cooling of HTS RF filters (Ju et al., 2003) in wireless telecommunication technology. Yuan and Jung (2000) developed a pulse tube cryocooler for the cooling of a computer's CPU.

Pulse tube cryocoolers are widely used in infrared night vision equipment (Kuo, and Loc, 1997, Yuan and Kuo, 1998, Radebaugh, 2000). Space-borne infrared devices cooled by pulse tube cryocoolers are reported by Liang and Zhou (2000), Raab, et al., (2001) and Tward and Chan (1999). Marquardt and Radebaugh (2000) have built a prototype version of a pulse tube oxygen liquefier to demonstrate the technology of liquefying and storing oxygen on Mars.

## 1.6 Introduction to this Thesis

The aim of the project is to gain a better understanding and deeper insight into the development of a single-stage inertance pulse tube cryocooler. A pulse tube cryocooler including its reciprocator was designed, manufactured, tested and mathematically modelled.

In chapter 2 the design and manufacturing of the reciprocator and the cryocooler is explained. The mathematical modelling of the reciprocator and the cooler are explained in chapter 3. Chapter 4 explains the one-dimensional CFD modelling of the pulse tube cryocooler. In chapter 5 the experimental evaluation of the reciprocator and the cooler are discussed. In chapter 6 discussions are made and conclusions are drawn.

# 2 CRYOCOOLER DESIGN

The mechanical design, manufacturing and assembly of the pulse tube cryocooler are explained in this chapter. The Cryocooler is divided into two parts namely the reciprocator and the cooler part (cold finger). The design of the reciprocator will be explained first and thereafter the design of the cold finger.

## 2.1 Reciprocator Design

Reciprocators are usually specified in terms of their displaced volume during one stroke and their operating frequency. This reciprocator generates pressure oscillations by a moving cylinder configuration. The moving cylinder moves back and forth over a stationary piston, compressing and expanding the gas.

The reciprocator design will be explained in two sections, the linear motor and the linear bearings. The latter provides mechanical stiffness to the system and ensures that the movement of the cylinder is straight with respect to the piston. The linear motor provides the power for the movement of the moving cylinder to compression the gas.

### 2.1.1 Linear Motor

The linear motor consists of two parts namely the moving plunger and the fixed magnet assembly. The fixed magnet assembly consists of a rare-earth Neodymium permanent magnet (NdFeB) ring sandwiched between two mild steel rings (figure 2.1). The N42 grade permanent magnet ring is axially magnetized, and Nickel coated. The function of the mild steel rings is to form a path for the magnetic flux. The fixed magnet assembly is attached to the outer cylinder (figure2.4) via 6 threaded attachment holes (diameter 5 mm) shown in figure 2.1.

The moving plunger consists of two copper coils wounded around a lamination stack and a moving cylinder. The lamination stack consists of 0.5 mm magnetic steel rings which are held together by a cylindrical clamp.

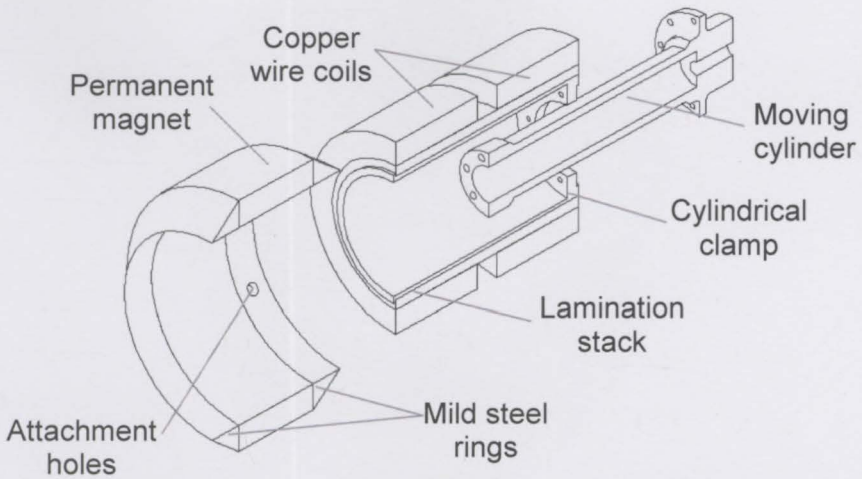


***Figure 2.1*** *Exploded isometric view of linear motor*

***Figure 2.2*** *Pictures of moving plunger*

***Figure 2.3*** *Picture of stationary magnet assembly attached to the outer cylinder*

The mild steel rings together with the lamination stack manipulate the magnetic flux such that the majority of the magnetic flux passes through the coil windings. Figure 2.4 shows the flux paths in the axial-symmetric magnetic circuit.

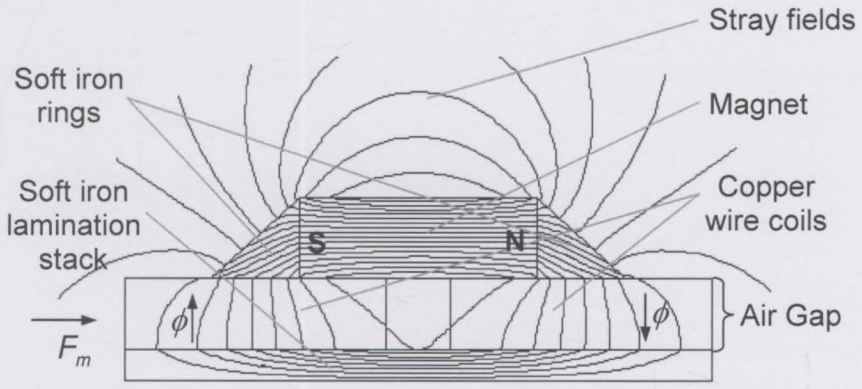


***Figure 2.4*** *Diagram showing flux paths of magnetic circuit*

The principle by which the linear motor operates given by equation 2.1, where $F_m$ is the electromagnetic force, $\ell$ the length of the conductor, $i$ the current that flows in the conductor and B the magnetic flux density (Nasar, 1998).

$$F = Bi\ell \tag{2.1}$$

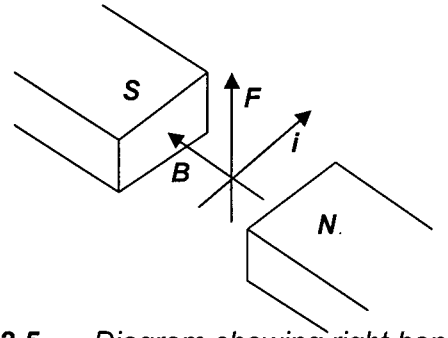


***Figure 2.5*** *Diagram showing right hand rule*

Figure 2.5 illustrates the directions of the vectors (right-hand-rule) given in equation 2.1. The perpendicular component of the magnetic flux that crosses the coils multiplied with the current that flows inside the coils results in a force in the axial direction. The direction of the current in the coils determines the direction of the force. It is shown in figure 2.4 that the magnetic flux, $\phi$ passing through each copper wire coil is of opposite direction. Thus the direction of the current in each coil has to be of opposite directions to ensure that the electromagnetic force $F_m$ on these coils is in the same direction.

### 2.1.2 Linear Bearing Design

The function of the linear bearing system is to ensure linear movement of the cylinder over the stationary piston and to provide mechanical stiffness. Two precision manufactured flexure units were accurately assembled on both sides of the stationary outer cylinder and the moving cylinder (figure 2.6). The stationary piston part then locates accurately over the outer cylinder onto the locating flange. In this way the piston is assembled inside the moving cylinder. A *dead end* set screw can be adjusted to set the top dead end of the cylinder (figure 2.6).

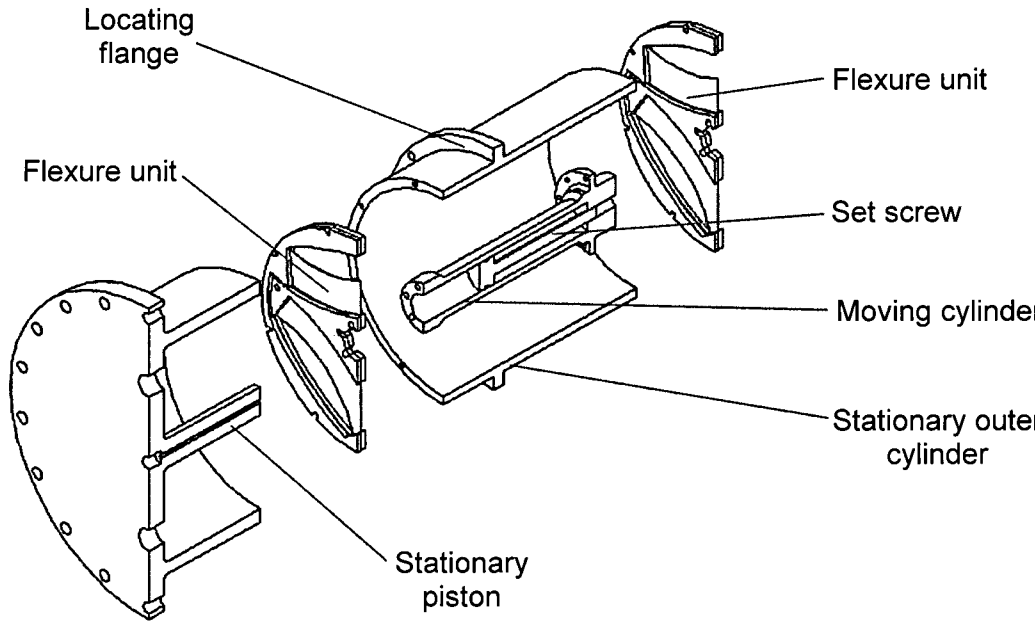


***Figure 2.6*** *Exploded isometric view of the linear bearing system*

Each flexure unit is a pre-assembled stack of precision cut plates. There are three types of plates namely spring steel flexure, moving rigid spider and stationary rigid clamp and are shown in figure 2.7. The moving rigid spider and the stationary rigid clamp are both called constrainer plates. The spring steel flexure is sandwiched between two of each constrainer plate in such a way that only the moving parts of the flexure are free to bend and translate axially when the moving rigid spider is displaced.

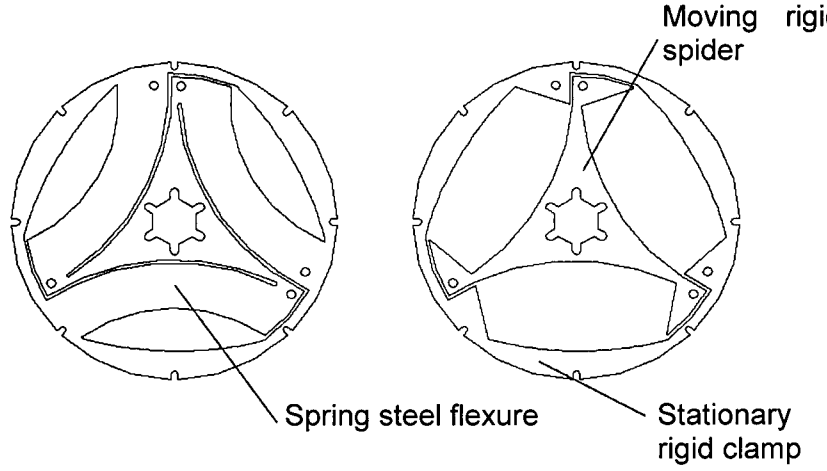


***Figure 2.7*** *Parts of Flexure bearing*

These flexures are very stiff in the radial direction and relatively flexible in the axial direction and they work together to ensure accurate linear movement.

The flexures were precision wire-cut to a tolerance of 3 microns and accurately assembled inside the reciprocator. The linear accuracy achieved is such that the cylinder does not touch the piston over a stroke of 15 mm during operation. The clearance gap between the piston and cylinder is 30 microns. This small gap ensures that the leakage through the gap is low during operation. Figure 2.8 shows a photo of a displaced flexure unit during operation.

***Figure 2.8*** *Displaced flexure unit during testing*

The flexure bearings were designed for the required maximum stroke, radial stiffness and axial stiffness. The axial stiffness is one of the determining factors of the natural frequency (resonance frequency) of the reciprocator. At this frequency the displacement of the reciprocator will be at a maximum and the reciprocator will operate most efficiently. At resonance the stored energy is constant and the system exchange energy internally between kinetic and potential energy. The equation for the natural frequency of the reciprocator is derived in section 3.1.6.

## 2.2 Cold Finger Design

The cold finger consists of seven parts namely the transfer tube, regenerator, u-tube, cold heat exchanger, pulse tube, inertance tube and reservoir.

Figure 2.9 shows a schematic of the cold finger and figures 2.10 and 2.11 show sectioned isometric views of the parts of the cold finger.

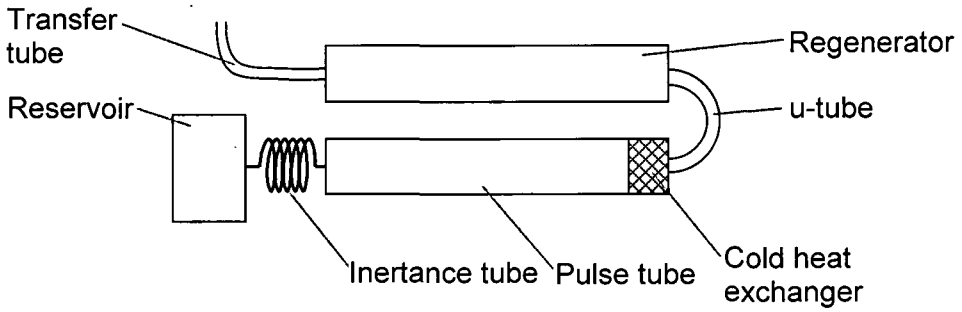


***Figure 2.9*** *Schematic of pulse tube cooler*

The regenerator is connected to the reciprocator via a relatively thin tube called the transfer tube. This allows the cold point to be positioned some distance apart from the reciprocator to minimise the EMI and vibrations that can be transferred from the reciprocator to the object being cooled. The u-tube splits the regenerator and the cold heat exchanger and permits the cold point to be near the tip of the cold finger.

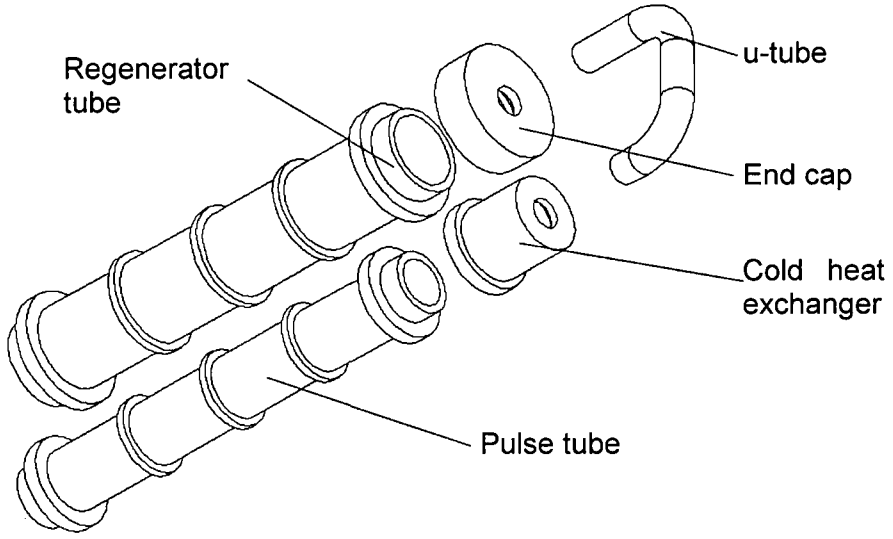


***Figure 2.10*** *Exploded isometric view of the cold finger (pulse tube, regenerator tube and cold heat exchanger)*

The wall thickness of the pulse tube and the regenerator has to be as thin as structurally possible to minimise the heat conduction from the cold to the hot side. It also has to be structurally strong enough to withstand pressures of 4 MPa. The wall thickness of both the pulse tube and the regenerator is 0.15 mm. Figure 2.11 shows a picture of a pulse tube with a wall thickness

0.15 mm cut in half. This particular tube failed under a pressure test, because it was not honed sufficiently in the inside. Stainless steel (grade 304) was used because of its relatively low thermal conductivity and for ease of manufacture.

***Figure 2.11*** *Picture of a cut pulse tube*

The regenerator was filled with cascaded discs of stainless steel mesh (gauge 500) also known as woven wire cloth which has a wire thickness of 25 microns, figure 2.13 (a). The cold heat exchanger is filled with a cascaded copper mesh (gauge 100) and it has a wall thickness of 0.2 mm.

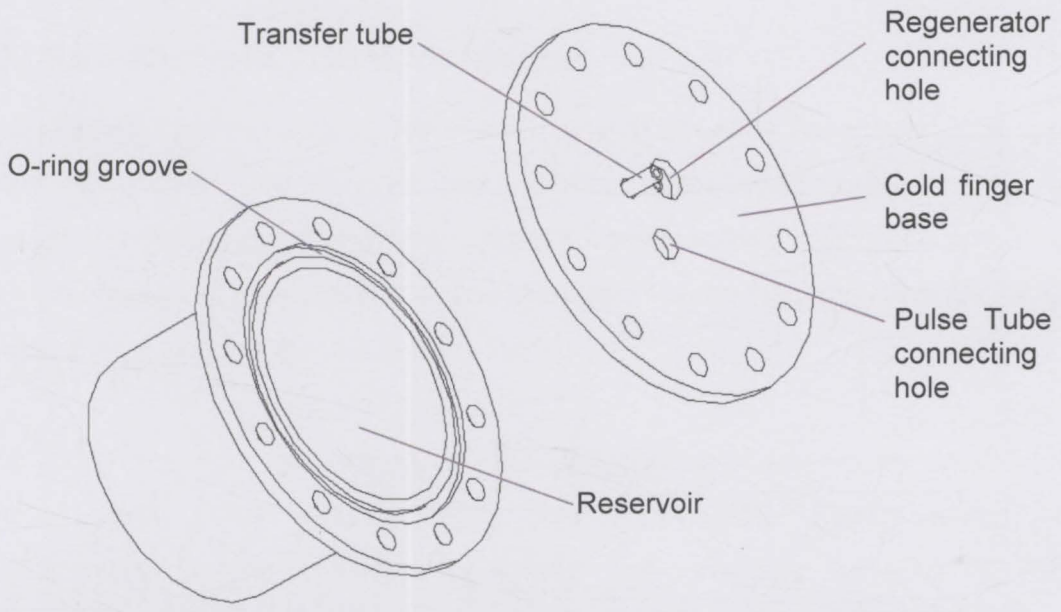


***Figure 2.12*** *Exploded view of reservoir and cold finger base*

The function of the cold finger base is to serve as a base for assembly for most of the cold finger parts. The reservoir, pulse tube, regenerator tube, split tube and inertance tube are all assembled to the cold finger base. Small

flanges were machined on both ends of the regenerator and pulse tube for easy welding. The reservoir is attached to the cold finger base and sealed with an O-ring. The transfer tube feeds through the cold finger base and connects to the regenerator. The inertance tube (figure 2.13b) is interchangeable for testing purposes and screws into the back of the cold finger base and seals with an end-seal. The end cap connects the u-tube to the regenerator tube. All the metal parts of the cold finger were manufactured from stainless steel (grade 304).


(a) (b)

***Figure 2.13*** *(a) Regenerator mesh sheets, (b) interchangeable inertance tube*

## 2.3 Manufacturing Considerations

All threaded fasteners were fixed with glue (Lock-tite) to ensure that they would not loosen due to vibrations. Only one electrical connection is fed through the helium-tight chamber with an epoxy sealed and insulated feed-through. The other terminal of the coil is earthed to the housing, thus there are no need for a second electrical feed-through.

It is important that the Helium in the cryocooler is very pure when it is charged. Any other gasses could condense and/or freeze which will contaminate the cooler during operation. The charging process involves several repeated charging and purging steps. The cryocooler is charged to the operating pressure and then purged to a pressure just above the atmospheric pressure. This process is repeated four times to ensure adequate concentration of Helium. Figure 2.14 shows a picture of the cryocooler during the charging process.


***Figure 2.14*** *Picture showing cryocooler being charged with helium*

# 3 MATHEMATICAL MODELLING

The mathematical modelling of the reciprocator and the pulse tube cooler is explained in this chapter. The reciprocator modelling will be explained first and thereafter the pulse tube cooler modelling. The modelling results will be compared with the experimental results of chapter 5.

## 3.1 Reciprocator

The reciprocator is modelled by solving the equations derived in this chapter. The first is the equation of motion which is derived from the conservation of momentum for a moving mass and spring system. The second is the equation for the applied voltage to the linear motor of the reciprocator. The third derivation is the analytical flux density of the linear motor and the fourth is the calculation of the pressure in the compression chamber.

### 3.1.1 Conservation of Momentum

Consider the reciprocator to consist of a moving mass m subjected to a number of linear forces *F* as shown in figure 3.1.

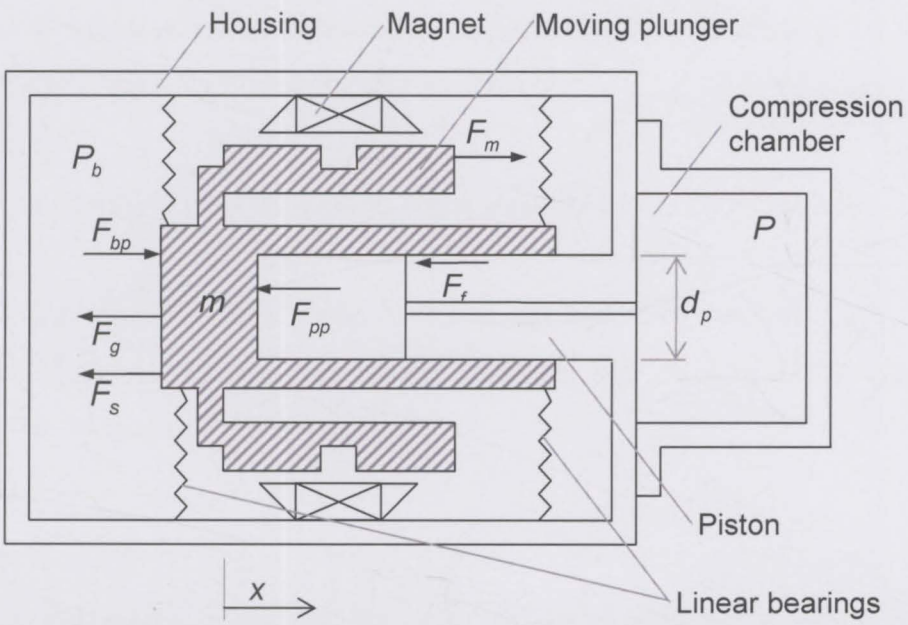


***Figure 3.1*** *Schematic presentation of reciprocator connected to a compression chamber showing all the forces acting on the moving plunger*

From the conservation of momentum, the change in momentum of a mass is equal to the sum of all the forces acting on the mass:

$$m\frac{\Delta u}{\Delta t} = -F_{pp} + F_{bp} - F_g - F_s - F_f + F_m \tag{3.1}$$

Equation 3.1 is also known as the equation of motion. The force due to the gas pressure on the piston area $A_p$ is:

$$F_{pp} = PA_p \tag{3.2}$$

where $A_p = \pi D_p^2/4$. The force on the back of the piston due to the charge pressure $P_{fill}$ is:

$$F_{bp} = P_{fill}A_p \tag{3.3}$$

The resultant force due to the gas pressure is thus:

$$F_p = (P - P_{fill})A_p \tag{3.4}$$

The gravitational force ($F_g = 0$ for horizontal operation) is:

$$F_g = mg \tag{3.5}$$

where $m$ is the mass of the moving parts and $g$ the gravitational acceleration. The force due to the linear bearings is:

$$F_s = k_s x \tag{3.6}$$

where $x$ is the deflection of the linear bearings and $k_s$ the spring constant of the linear bearings which was determined experimentally in section 5.1.1. The force due to damping and friction on the system is:

$$F_f = cu \tag{3.7}$$

where c is the damping coefficient and u the velocity of the moving mass.

The operating principle of the linear motor is explained in section 2.1.1. The electromagnetic force is a function of the average flux density in the coil $\overline{B}$ the current $i$ and length of coil wire $\ell$.

$$F_m = \overline{B}i\ell \tag{3.8}$$

The flux density $\overline{B}$ is averaged over the air gap in the area which the coil is. It is a function of position, because the coil is moving through a non-uniform magnetic field. The mathematical function for the average magnetic flux density is determined later by three methods namely analytical, finite element analyses and experimentally. The analytical expression for the flux density in

the air gap is derived in section 3.1.3 and an experimental expression together with the finite element results are shown in section 5.1.2.

### 3.1.2 Voltage

The equation for the applied voltage $V$ to the linear motor is shown in equation 3.9. The applied voltage is equal to the sum of three voltage drops. The first term is the induced back emf due to the moving coil the magnetic field. The second is the induced voltage due to the electromagnetic inductance and the last term is the voltage drop over the coil due to its resistance $R$.

$$V = \bar{B}\ell u + L\frac{\Delta i}{\Delta t} + Ri \tag{3.9}$$

Equation 3.1 and 3.9 are interconnected by the velocity of the moving plunger and the current in the coil. The voltage, $V$ is the input into the system and the velocity and current are the results. These two equations can be solved simultaneously to calculate the velocity and current versus time of the system.

### 3.1.3 Analytical Flux Density

The magnetic flux density in the air gap $B_g$ in a magnetic circuit is equal to the total magnetic flux $\phi$ in the magnetic circuit divided by the cross sectional area of the air gap $A_{c,m}$ (equation 3.10).

$$B_g = \frac{\phi}{A_{c,m}} \tag{3.10}$$

Stray fields are always present in magnetic circuits which mean that the flux through the copper coils in the air gaps is less than the flux through the magnet. A leakage factor $k_m$ is introduced to accommodate the flux leakage and equation 3.11 shows the relation between the flux densities inside the magnet and the air gaps. This leakage factor is only relevant for a particular magnetic circuit configuration. The effects of fringing, iron saturation and hysteresis losses are neglected in the model.

$$\phi = B_m A_{c,m} = k_m B_g A_{c,g} \tag{3.11}$$

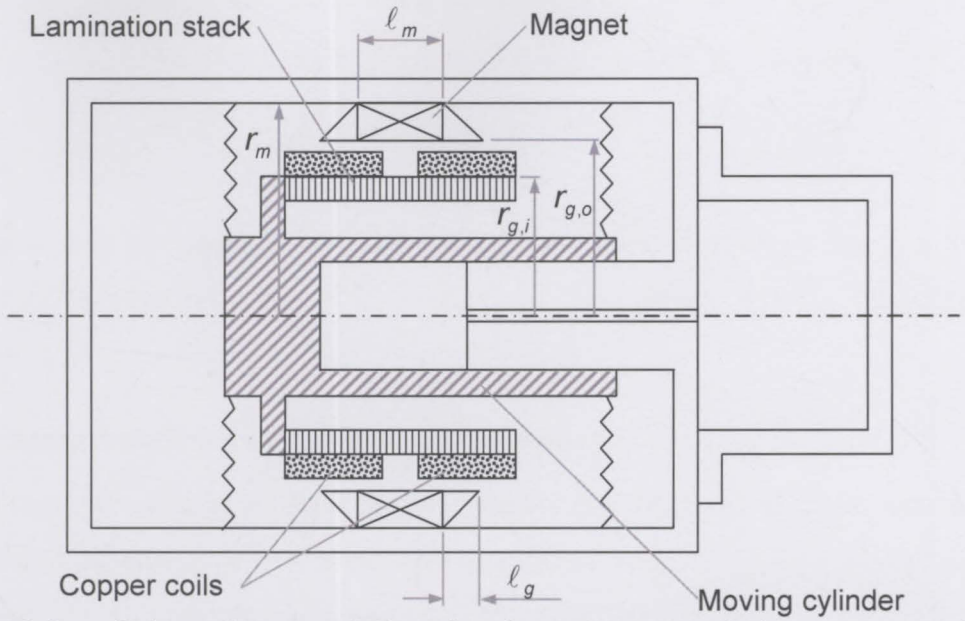


***Figure 3.2*** *Schematic presentation of reciprocator connected to a compression chamber showing linear motor dimensions*

The magnetic flux $\phi$ is equal to the magnetomotive force $\Im$ divided by the total reluctance $\Re$ of the magnetic circuit which is assumed to be only the reluctance of the air gap because the reluctance of soft iron is relatively small compared with the reluctance of air (Nasar, 1998).

$$\phi = \frac{\Im}{\Re} \tag{3.12}$$

The relation for the magnetic reluctance in one air gap is shown in equation 3.13 where $r_{g,o}$ and $r_{g,i}$ are the outside and inside radii of the air gap (figure 3.2). The cross sectional area of the air gap $A_{c,g}$ is taken as an average cross sectional area between the inside and outside diameters of the air gap (equation 3.14).

$$\Re = \frac{r_{g,o} - r_{g,i}}{\mu_0 A_{c,g}} \tag{3.13}$$

$$A_{c,g} = \ell_g \pi \left(r_{g,o} + r_{g,i}\right) \tag{3.14}$$

The relation for the magnetomotive force $\Im$ is shown in equation 3.15 where $H_m$ is the magnetic field strength of the magnet and $\ell_m$ the length of the magnet. The magnetic field strength of the magnet is determined by its position on the magnetic circuit and will be derived in the following section.

$$\Im = H_m \ell_m \tag{3.15}$$

Eliminating $\Im$, $\Re$ and $\phi$ by combining equations 3.11, 3.12, 3.13 and 3.15, gives the relation for the flux density inside each air gap $B_g$ (equation 3.16).

$$B_g = \mu_0 \frac{H_m \ell_m}{2(r_{g,o} - r_{g,i})k_m} \tag{3.16}$$

There are two air gaps in the magnetic circuit and therefore the magnetic reluctance (equation 3.13) is multiplied by two when it is substituted in equation 3.16.

### 3.1.4 Operating Point of a Permanent Magnet

An equation for the load line of the permanent magnet is obtained when equations 3.11 and 3.16 are combined (equation 3.17).

$$B_m = -\mu_0 \frac{A_{c,g} \ell_m}{2(r_{g,o} - r_{g,i})A_{c,m}} H_m \tag{3.17}$$

Equation 3.17 plots as a straight line of negative gradient on the B-H plane of a permanent magnet (Organ, 1999). The working point is where this load line intersects with demagnetization (B-H) curve of the permanent magnet (figure 3.3). The magnetic field strength and the magnetic flux density of the magnet are then represented by the coordinates of working point on the B-H curve.

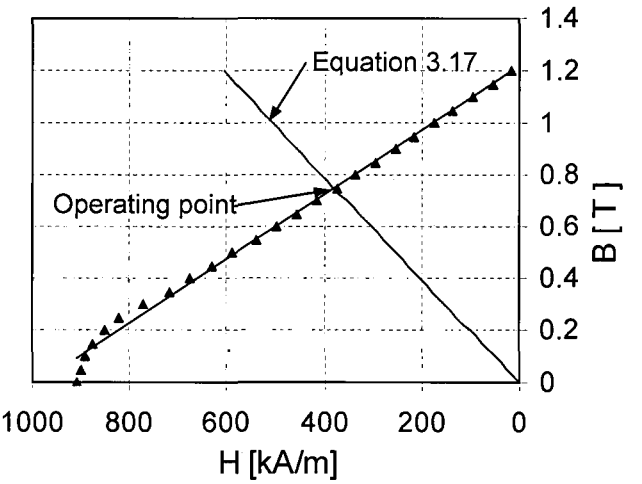


***Figure 3.3*** *Operating point of the NdFeB magnet (grade N42) on its demagnetization curve (magnetomotive force versus flux density) (Organ, 1999)*

### 3.1.5 Pressure Chamber

From the ideal gas law the pressure, $P$ (equation 3.18) and the initial mass of the gas inside the pressure chamber $m_0$ (equation 3.19) can be calculated

$$P = \frac{mRT}{V} \tag{3.18}$$

$$m_0 = \frac{P_0 V_0}{RT_0} \tag{3.19}$$

The volume of the gas within the compression volume can be expressed as

$$V = V_0 - xA_p \tag{3.20}$$

The change of energy of the gas is equal to the rate by which boundary work $\dot{W}_b$ is done on the gas minus the rate that heat $\dot{Q}_{out}$ is removed from the gas.

$$\frac{\partial E}{\partial t} = \dot{W}_b - \dot{Q}_{out} \tag{3.21}$$

The energy is substituted with the product of the mass of the gas $m$, the specific heat $c_v$ and the change in temperature $\Delta T$ :

$$\frac{mc_v \partial T}{\partial t} = \dot{W}_b + \dot{Q}_{out} \tag{3.22}$$

Equation 3.22 can be solved explicitly when discretized as:

$$T^{new} = T^{old} + \frac{\Delta t}{mc_v}\left(\dot{W}_b + \dot{Q}_{out}\right) \tag{3.23}$$

where the boundary work (Neveu, P and Babo, C, 2000) is equal to:

$$\dot{W}_b = -p\frac{\Delta V}{\Delta t} \tag{3.24}$$

### 3.1.6 Natural Frequency

The natural frequency $f_n$ of the reciprocation system is determined by the mass of the moving plunger and the mechanical stiffness (spring constant) of the system. The gas can be modelled as a mechanical spring due to its compressibility. The spring constant of the system is the sum of the linear bearing spring constant and the spring constant of the gas spring. The relations for the spring constant of the gas and the natural frequency of the reciprocator will now be derived in this section.

The reciprocator and pulse tube system is symbolized by a moving piston with mass $m$ and a compression space with a volume $V$. The compression space represents the volume in the cold finger (pulse tube, regenerator, heat exchangers and split tube) and the volume in the reciprocator. The piston reciprocates between its maximum and minimum displacements compressing and expanding the gas. The back pressure (pressure behind the piston) $p_b$ is assumed to be constant and equal to the charge pressure $p_{fill}$. The initial pressure $p$ at $t=0$ in the compression space is also equal to the charge pressure. The initial volume of the compression space is $V_0$ at time $t=0$.

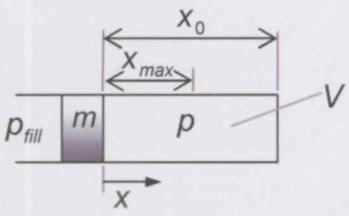


***Figure 3.4*** *Schematic of the piston and compression space*

The relation for the gas spring will be derived from an isentropic relation for an ideal gas (equation 3.25) where $k$ is the specific heat ratio for the gas, $p$ the pressure in the compression space and $v$ the specific volume of the gas.

$$\left(\frac{p}{p_{fill}}\right)=\left(\frac{v_0}{v}\right)^k \tag{3.25}$$

Assuming that the mass in the compression space is constant in other words, the mass flow rate in the inertance tube and leakage passed the piston is zero then the specific volume can be replaced by the volume $V$. From equation 3.25 the pressure in the compression space can be written as

$$p=\left(\frac{V_0}{V}\right)^k p_{fill} \tag{3.26}$$

The compression volume $V$ at any time is equal to the initial compression volume $V_0$ minus the product of the piston area $A_p$ and piston displacement $x$.

$$V=V_0-A_p x \tag{3.27}$$

Substitute equation 3.27 into equation 3.25 and hence an equation for the pressure in the compression space in terms of the initial volume $V_0$, charge pressure $P_{fill}$, piston area $A_p$ and displacement $x$.

$$p = \left( \frac{V_0}{V_0 - A_p x} \right)^k p_{fill} \tag{3.28}$$

The spring constant of the gas spring $k_g$ is equal to the force due to the pressure $F_p$ divided by the displacement $x$

$$k_g = \frac{F_p}{x} \tag{3.29}$$

Substituting the relation for the force due to the pressure (equation 3.4) into equation 3.29 where the pressure $p$ is the pressure acting on the piston when the piston is at a displacement of $x$

$$k_g = \frac{(p - p_{fill})A_p}{x} \tag{3.30}$$

The natural frequency $f_n$ of the reciprocator system can be written in terms of the spring constant of the flexure system $k_s$ and the gas spring $k_g$ as:

$$f_n = \frac{1}{2\pi} \sqrt{\frac{k_s + k_g}{m}} \tag{3.31}$$

Substituting equation 3.30 into equation 3.31:

$$f_n = \frac{1}{2\pi} \sqrt{\frac{k_s + \frac{(p - p_{fill})A_p}{x}}{m}} \tag{3.32}$$

When the piston is at its maximum displacement, the pressure will also be at a maximum and the natural frequency can be calculated from equation 3.32 when the pressure and displacement amplitudes are known. This relation for the natural frequency of the reciprocator, equation 3.32, is also given by Koh et al (2002). It can be seen from equation 3.32 and the relation for the pressure (equation 3.28) that the natural frequency of the reciprocator is dependant on the charge pressure, piston area, piston displacement and the volume of the compression space.

## 3.2 Cold Finger

The gas flow in the cold finger is modelled as one dimensional compressible flow. The characteristics of regenerators and heat exchanger, for example, wetted area of mesh, hydraulic diameter and heat transfer coefficient is essential to model the cold finger and is derived in section 3.2.1. The

conservation equations, continuity, momentum and energy for one dimensional compressible flow are shown in section 3.2.2. The conservation equations are derived in Appendix A and discretized and linearized in Appendix B. A computer simulation program is used to solve and discretized conservation equations and is explained in section 4.

### 3.2.1 Characteristics of Regenerator and Heat Exchangers

Regenerators and heat exchangers are packed with a matrix of porous media and can be modelled as a tube with a smaller, superficial flow area, larger friction coefficient and a larger heat transfer (wetted) area between the tube and the working fluid. The matrix material can be either metal spheres or metal wire screens. Sphere packed regenerators are less common in single stage 70 K cryocoolers and will not be discussed.

Wire screen matrices are specified in terms of their void fraction and wire diameters. The void fraction $e_v$ is defined as the ratio between the void volume and the total volume of the regenerator or heat exchanger. The void volume is equal to the total volume minus the volume of the matrix material $(V_0 - V_m)$.

$$e_v = \frac{V_0 - V_m}{V_0} \tag{3.33}$$

The volume of the gas in the regenerator $V$ is equal to the void volume of the matrix and can be written in terms of the void fraction $e_v$ and the total volume $V_0$.

$$V = e_v V_0 \tag{3.34}$$

The volume of the matrix material is also written in terms of the void fraction and total volume of the regenerator

$$V_m = (1 - e_v) V_0 \tag{3.35}$$

The volume of a wire screen matrix $V_m$ can also be rewritten as a length multiplied by the cross sectional area of the screen wires (Barron, 1999)

$$V_m = \frac{\pi d_w^2 \ell}{4} \tag{3.36}$$

The wetted area between the fluid and the matrix $A_w$ is equal to the surface area of the wire which is equal to the length of the wire $\ell$ times the circumference of the wire $\pi D_w$

$$A_w = \ell \pi d_w \tag{3.37}$$

Combining equations 3.35, 3.36 and 3.37 eliminating $\ell$ yields:

$$A_w = \frac{4V_0(1-e_v)}{d_w} \tag{3.38}$$

The cross sectional area of the control volume $A_c$ is equal to the total volume divided the length of the control volume $\Delta x$

$$A_c = \frac{V_0}{\Delta x} \tag{3.39}$$

The flow area $A_f$ of the gas is equal to the void fraction times the cross sectional area $A_c$

$$A_f = e_v A_c \tag{3.40}$$

The mass of the gas in the control volume is equal to the flow area $A_f$ times the length of the control volume $\Delta x$ times the density of the gas $\rho$

$$m = \rho A_f \Delta x \tag{3.41}$$

The mass of the matrix material in the control volume is equal to the density of the matrix material $\rho_m$, times the volume of the matrix material.

$$m_m = \rho_m(1-e_v)A_c \Delta x \tag{3.42}$$

From equation 3.41 the mass flow rate can be written in terms of the velocity

$$\dot{m} = \rho A_f u \tag{3.43}$$

The wetted perimeter $P_w$ is equal to the wetted area of the matrix divided by length of the control volume $\Delta x$

$$P_w = \frac{A_w}{L} \tag{3.44}$$

Substitute equations 3.40 and 3.41:

$$P_w = \frac{4A_c(1-e_v)}{d_w} \tag{3.45}$$

The hydraulic diameter $d_h$ is equal to four times the flow area divided by the wetted perimeter

$$d_h = \frac{4A_f}{P_w} \tag{3.46}$$

Substitute equation 3.42 and 3.45:

$$d_h = \frac{e_v d_w}{(1-e_v)} \tag{3.47}$$

The Reynolds number based on the hydraulic diameter and equivalent velocity is shown in the following relation:

$$Re_h = \frac{\rho u d_h}{\mu} \tag{3.48}$$

The heat transfer characteristics in terms of the Reynolds number *Re* for a porosity of 0.67 is approximated by the following relation (Kays and London, 1984)

$$\log\left(StPr^{2/3}\right) = -0.4041 \times \log(Re_h) - 0.22 \tag{3.49}$$

The heat transfer coefficient $h_m$ is a factor of the Stanton number *St* and can be calculated from

$$h_m = StPr^{2/3} \frac{c_p^{1/3} u \rho k^{2/3}}{(c_p \mu)^{2/3}} \tag{3.50}$$

Since the regenerator in the cryocooler typically experiences bi-directional oscillating flow and large pulsating pressure conditions, there is a fundamental discrepancy in calculating the friction factor with the analysis based on steady flow for oscillating flow conditions. Until recently, only steady flow relations for the pressure drop over regenerators from Kays (1984) were used. Recent efforts have been made to improve the predictions of the pressure drop over the regenerator in oscillating flow conditions. Helvensteijn (1998) presented the friction factor for 36 through 70 Hz. There was no clear indication found for frequency dependence of the friction factor over the tested frequency range. Ju (1998) presented a correlation for the friction factor at a fixed frequency of 50 Hz. The relationship of the phase shifts between the velocity and the pressure wave was also presented. It was found that the cycle averaged pressure drop of oscillating flow is two to three times higher than the steady

flow at the same Reynolds number based on the cross sectional mean velocity. Choi (2004) investigated the pressure drop and phase shift over the regenerator with accurate experimental results. His relation for the friction coefficient (Darcy) in the regenerator in oscillating flow and pulsating pressure conditions is preferred and is given in equation 3.51.

$$f_{reg} = \frac{39.52}{Re_h} + 0.01 \qquad (5 \le Re_h \le 100) \tag{3.51}$$

## 3.3 Cooling of Electronics

One of the applications of cryocoolers is the cooling of sensitive and/or superconducting electronics. It is envisaged that these electronics to be cooled by a cryocooler will be package in multi-chip modules (MCM's). The multichip module will then be connected to the cold point and insulated with a vacuum enclosure.

The enclosure for the MCM should be designed to minimise the heat flow from the environment to the MCM. The enclosure and MCM are modelled as spheres to simplify the radiative heat flow modelling. The simplified enclosure and its components are shown in figure 3.5. Multilayer insulation (MLI) is used to minimize radiative heat flow from the enclosure to the MCM.

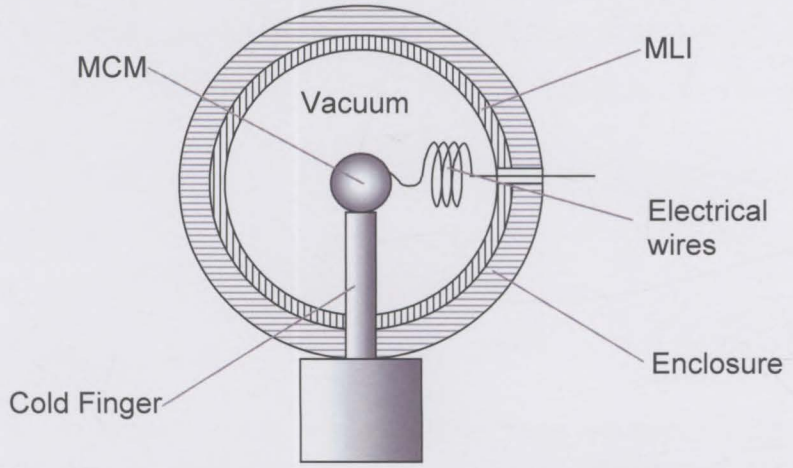


***Figure 3.5*** *Schematic of a pulse tube cold finger integrated with a spherical approximated multi chip module*

The cryocooler removes heat from the MCM and cools the MCM from room temperature to the required cryogenic temperature. The heat load on the cooler is the sum of the heat sources which are the heat flow from the

environment through the enclosure $\dot{Q}_e$, internal heat generation in the MCM $\dot{Q}_{MCM}$, heat conduction from the environment through the electrical wires $\dot{Q}_w$ and heat conduction through the wall of the cold finger $\dot{Q}_{cf}$. The temperature of the environment is depicted by $T_e$ and the required cryogenic temperature of the multi chip is $T_{MCM}$. Figure 3.6 shows a thermal resistance diagram for the heat flow to the MCM, where $\dot{Q}_{cooler}$ is the required cooler load.

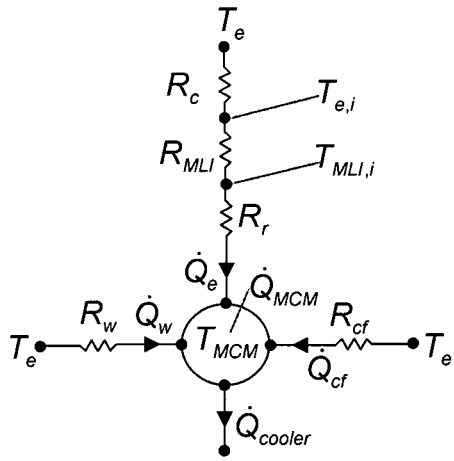


***Figure 3.6*** *Thermal resistance diagram for heat flow from the environment to the MCM*

### 3.3.1 Heat Flow Through the Electrical Wires

Equation 3.58 is the relation for the conductive heat flow through the electrical wires where the relation for the thermal resistance $R_w$ is given in equation 3.59.

$$\dot{Q}_w = \frac{-(T_{MCM} - T_e)}{R_w} \tag{3.58}$$

$$R_w = \frac{\ell_w}{k_w A_{c,w}} \tag{3.59}$$

where $\ell_w$ is the length of the wire, $A_{c,w}$ the cross sectional area of the wires and $k_w$ the thermal conductivity of the wire material.

### 3.3.2 Heat Flow Through the Enclosure

The heat flow from the environment to the MCM is equal to the temperature difference between the MCM and the environment divided by the sum of all the thermal resistances:

$$\dot{Q}_e = -\frac{(T_a - T_{MCM})}{R_c + R_{MLI} + R_r} \tag{3.60}$$

where $R_c$ is thermal resistance of the enclosure wall, $R_{MLI}$ the thermal resistance of the multi-layer insulation and $R_r$ the thermal resistance of the vacuum. The thermal resistance for the conductive heat flow through the enclosure $R_c$ is:

$$R_c = \frac{t_e}{k_e A_e} \tag{3.61}$$

where $t_e$ is the wall thickness of the enclosure, $k_e$ the thermal conductivity, $A_e$ the average area of the spherical enclosure and $T_{e,i}$ the inside temperature of the enclosure. The heat flow through the MLI can be written as

$$\dot{Q}_{MLI} = \frac{T_{e,i} - T_{MLI,i}}{R_{MLI}} \tag{3.62}$$

Weisend (1998) shows that the heat flux through five layers of aluminized shields using double layers of silk net for spacing is about 10 W/m$^2$ when the temperature at the warm end is 278 K and the cold end is 77 K. Substituting the heat flux and the temperature difference into equation 3.62 and rearranging the formula yields:

$$\frac{10W}{A_{MLI}} = \frac{278K - 77K}{R_{MLI}} \tag{3.63}$$

A relation for the thermal resistance of the MLI (equation 3.64) is obtained by rearranging equation 3.63

$$R_{MLI} = 20.1 A_{MLI} \tag{3.64}$$

Figure 3.7 and equation 3.65 shows the convention and the view factor relation for radiative heat flow between two concentric spheres.

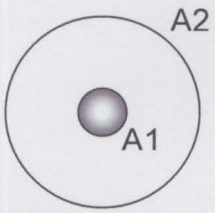


***Figure 3.7*** *Schematic showing two concentric spheres*

$$F_{21} = \frac{A_1}{A_2} \tag{3.65}$$

The relation for the heat flow from the outer sphere to the inner sphere is given in equation 3.66 (Mills, 1995)

$$\dot{Q}_{21} = \frac{\sigma\left(T_2^4 - T_1^4\right)}{\frac{1-\varepsilon_2}{\varepsilon_2 A_2} + \frac{1}{A_2 F_{21}} + \frac{1-\varepsilon_1}{\varepsilon_1 A_1}} \tag{3.66}$$

Substituting equation 3.65 into 3.66

$$\dot{Q}_{21} = \frac{\sigma\left(T_2^4 - T_1^4\right)}{\frac{1-\varepsilon_2}{\varepsilon_2 A_2} + \frac{1}{A_1} + \frac{1-\varepsilon_1}{\varepsilon_1 A_1}} \tag{3.67}$$

Equation 3.67 is rewritten in terms of the radiative heat flow between the enclosure and the MCM

$$\dot{Q}_r = \frac{\sigma\left(T_{MLI}^4 - T_{MLI}^4\right)}{\frac{1-\varepsilon_{MLI}}{\varepsilon_{MLI} A_{MLI}} + \frac{1}{A_{MCM}} + \frac{1-\varepsilon_{MCM}}{\varepsilon_{MCM} A_{MCM}}} \tag{3.68}$$

From equation 3.68 the thermal resistance for the heat flow from the inside surface of the MLI to the MCM can be written as

$$R_r = \frac{\frac{1-\varepsilon_{MLI}}{\varepsilon_{MLI} A_{MLI}} + \frac{1}{A_{MCM}} + \frac{1-\varepsilon_{MCM}}{\varepsilon_{MCM} A_{MCM}}}{\sigma\left(T_{MLI} + T_{MCM}\right)\left(T_{MLI}^2 + T_{MCM}^2\right)} \tag{3.69}$$

We are only interested in the total heat load on the cryocooler and from this we can determine what the minimum cooling power should be. The thermal capacity (mass and the specific heat) of the MCM and all other parts connected to the cold point will determine the cool down time of the MCM for a specified cooling power.

### 3.3.3 Heat Flow Through the Cold Finger Wall

Equation 3.70 is the relation for the conductive heat flow through the cold finger wall where the relation for the thermal resistance $R_{cf}$ is given in equation 3.71.

$$\dot{Q}_{cf} = \frac{-(T_{MCM} - T_e)}{R_{cf}} \tag{3.70}$$

$$R_{cf} = \frac{\ell_{cf}}{k_{cf} A_{c,cf}} \tag{3.71}$$

where $\ell_{cf}$ is the length of the cold finger, $A_{c,cf}$ the cross sectional area of the cold finger walls and $k_{cf}$ the thermal conductivity of the cold finger material.

# 4 ONE-DIMENSIONAL CFD SIMULATION

The objective is to write a computer program with the aim of capturing the flow mechanisms inside the inertance pulse tube refrigerator (IPTR). This is not to be an accurate mathematical model of the IPTR. It should only be adequate enough to demonstrate the operating principle of the IPTR. The program could later be developed further towards a more exact model and design tool.

## 4.1 Model

Various simplified simulations have been undertaken to model the IPTR. Muralidhar and Suzuki (2001) analysed the flow and heat transfer in the regenerator by using a harmonic analyses technique and non-dimensionalized parameters. Roach and Kashani (1997) wrote a computer model for an IPTR by using an electrical analogy. Zhu and Matsubara (2004) modelled an IPTR using a one dimensional compressible fluid flow method. The conservation equations were solved using a finite difference method and a staggered grid. They used a second order upwind scheme for the time terms except for the boundaries, where a first order upwind scheme was used.

In the current project the pulse tube cooler is modelled with a one-dimensional time dependant CFD model for compressible flow using the SIMPLE method suggested by Patankar (1980). The equation of state and the conservation equations namely the conservation of mass, momentum and energy were derived in Appendix A and are shown in the following section. These conservation equations are discretized and linearized in Appendix B. The discretized conservation equations are solved implicitly with a numerical algorithm programmed in FORTRAN. The output of the program was plotted using Matlab.

A staggered grid (figure 4.1) is used to prevent pressure decoupling. Pressure-velocity coupling is the dominant feature of the conservation equations and staggered grids are the most efficient way of handling it on Cartesian meshes. Each cell in figure 4.1 represents one control volume

where the point in the middle is its nodal point *i*. The scalar properties namely pressure, density, temperature mass, and gas properties are saved at these nodal points. The mass flow rate and velocity are saved on the interfaces of these control volumes and are represented by *j*'s.

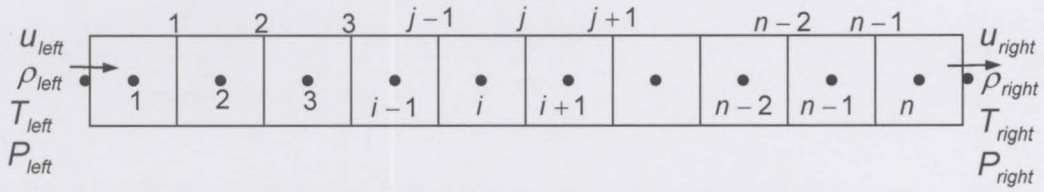


***Figure 4.1*** *One dimensional staggered grid*

The pulse tube cooler (figure 4.2) in its simplest form is a series of tube sections each with various diameters and lengths that are connected to a separate volume or reservoir. Some of these tube sections represents the regenerator and the heat exchangers and are filled with porous media. The reservoir and reciprocator are treated as left and right boundary conditions.

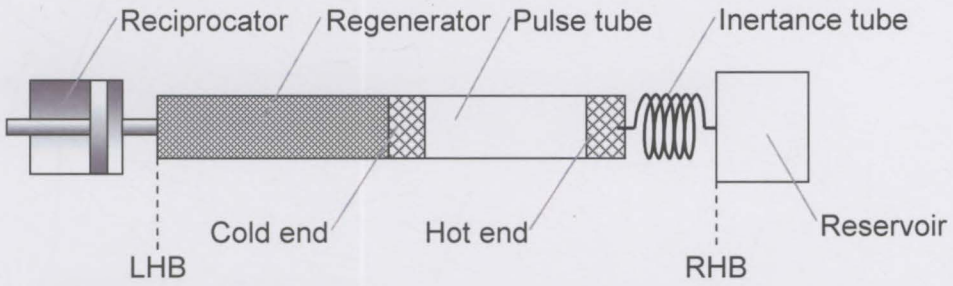


***Figure 4.2*** *Schematic of an inertance pulse tube refrigerator (IPTR)*

### 4.1.1 Equations

The working gas, Helium, is assumed to be ideal and the equation of state is written in terms of the pressure $p$, temperature $T$, density $\rho$ and ideal gas constant of Helium $R$.

$$p = \rho RT \tag{4.1}$$

Conservation equations as derived in Appendix A from first principles are given in equations 4.2 to 4.6.

Continuity:

$$\frac{\partial(\rho u)}{\partial x} + \frac{\partial \rho}{\partial t} = 0 \tag{4.2}$$

Momentum:

$$\frac{\partial(\rho u)}{\partial t}+\frac{\partial(\rho u u)}{\partial x}=-\frac{\partial p}{\partial x}-\frac{C_f \rho u|u|S}{2V} \tag{4.3}$$

Energy for gas:

$$\begin{aligned}&(c_p-R)\rho\frac{\partial T}{\partial t}=-c_p\frac{\partial \rho u T}{\partial x}+\frac{\partial}{\partial x}\left(k\frac{\partial T}{\partial x}\right)\\&-(c_p-R)T\frac{\partial \rho}{\partial t}-\frac{S_{in}h_{in}}{V}(T-T_t)-\frac{A_w h_m}{V}(T-T_m)\end{aligned} \tag{4.4}$$

The last term of equation 4.4 is zero when there is no mesh inside the tube. The temperatures of the tube wall and mesh (gas surroundings) are assumed to be equal and are treated as one thermal mass where the temperature is denoted by $T_{mt}$. The energy equation for gas surroundings is:

$$\begin{aligned}&\left((1-e_v)\rho_m A_c c_m+\rho_t A_{c,t} c_t\right)\frac{\partial T_{mt}}{\partial t}=k_t A_{c,t}\frac{\partial}{\partial x}\left(\frac{\partial T_{mt}}{\partial x}\right)+\pi d_{in}h_{in}(T-T_{mt})\\&-\pi d_{ex}h_{ex}(T_{mt}-T_{ex})+\frac{4A_c(1-e_v)}{d_w}h_m(T-T_{mt})\end{aligned} \tag{4.5}$$

When there is no mesh in the tube equation 4.5 reduces to:

$$\rho_t A_{c,t} c_t\frac{\partial T_{mt}}{\partial t}=k_t A_{c,t}\frac{\partial}{\partial x}\left(\frac{\partial T_{mt}}{\partial x}\right)+\pi d_{in}h_{in}(T-T_{mt})-\pi d_{ex}h_{ex}(T_{mt}-T_{ex}) \tag{4.6}$$

### 4.1.2 Boundary Conditions

Both the left and right hand boundaries are pressure boundaries, where the pressure is given and mass is allowed to cross the boundary. The mass flow rate is then calculated due to a pressure difference between the left and right-hand boundaries. The pressure at the left hand boundary (equation 4.7) is a sinusoidal, time dependant function which represents the reciprocator. At the right hand boundary the momentum effects of the gas are ignored in the reservoir and the temperature of the gas is assumed to be constant. These assumptions are realistic when its volume is large and when its walls are subjected to cooling by the environment. The right hand boundary pressure is calculated from the equation of state (equation 4.8) and only the mass change inside the volume affects the pressure.

$$p_{left}=p_{max}\sin(2\pi ft) \tag{4.7}$$

$$p_{right} = \frac{mRT}{V} \tag{4.8}$$

The boundary conditions for the temperature are shown in equations 4.9 and 4.10 where $T_e$ is the temperature of the environment which is constant.

$$T_{left} = \begin{cases} T_1 & \dot{m}_{left} < 0 \\ T_e & \dot{m}_{left} > 0 \end{cases} \tag{4.9}$$

$$T_{right} = \begin{cases} T_e & \dot{m}_{right} < 0 \\ T_n & \dot{m}_{right} > 0 \end{cases} \tag{4.10}$$

The boundary conditions for the density are given in equations 4.11 and 4.12.

$$\rho_{left} = \begin{cases} \rho_1 & \dot{m}_{left} < 0 \\ \dfrac{p_{left}}{RT_{left}} & \dot{m}_{left} > 0 \end{cases} \tag{4.11}$$

$$\rho_{right} = \begin{cases} \dfrac{m_R}{V_R} & \dot{m}_{right} < 0 \\ \rho_n & \dot{m}_{right} > 0 \end{cases} \tag{4.12}$$

## 4.2 Algorithm

The algorithm employed is shown in figure 4.3 and will now be explained. In step 1 the geometry input is given where the number of tube sections with their parameters is specified. These parameters include number of elements, length, diameter, wall thickness, heat transfer coefficient to environment, material type of mesh and tube, and the porosity and wire diameter of mesh.

In step 2 the grid is calculated from the geometry input. This includes the volumes and flow and heat transfer areas of the control volumes. In step 3 the program inputs are given which are: the initial values for $p$, $T$, $u$ and $\rho$, boundary conditions, length and number of the time increments, convergence criteria, and relaxation and flux blending factors, and the material and gas properties. The conservation equations are discretized with flux blending factors which blend the central difference and the upstream values, where interpolation is needed to calculate the velocity, temperature and density. When the flux blending factor is 0, the upstream value is used and when it is 1, central differencing.

The program starts with a time loop. The pressure on the left hand boundary is calculated as a function of time. At each time step a new pressure is calculated and then the iteration loop starts. In step 4 the coefficients are calculated which includes the Reynolds number, friction coefficients and heat transfer coefficients. Then in steps 5 and 6 the discretized momentum and mass conservation equations (the latter in the form of a pressure correction equation) are solved with a tri-diagonal matrix algorithm (TDMA). In step 7 the velocities and densities are updated with their respective corrections, resulting from their pressure corrections.

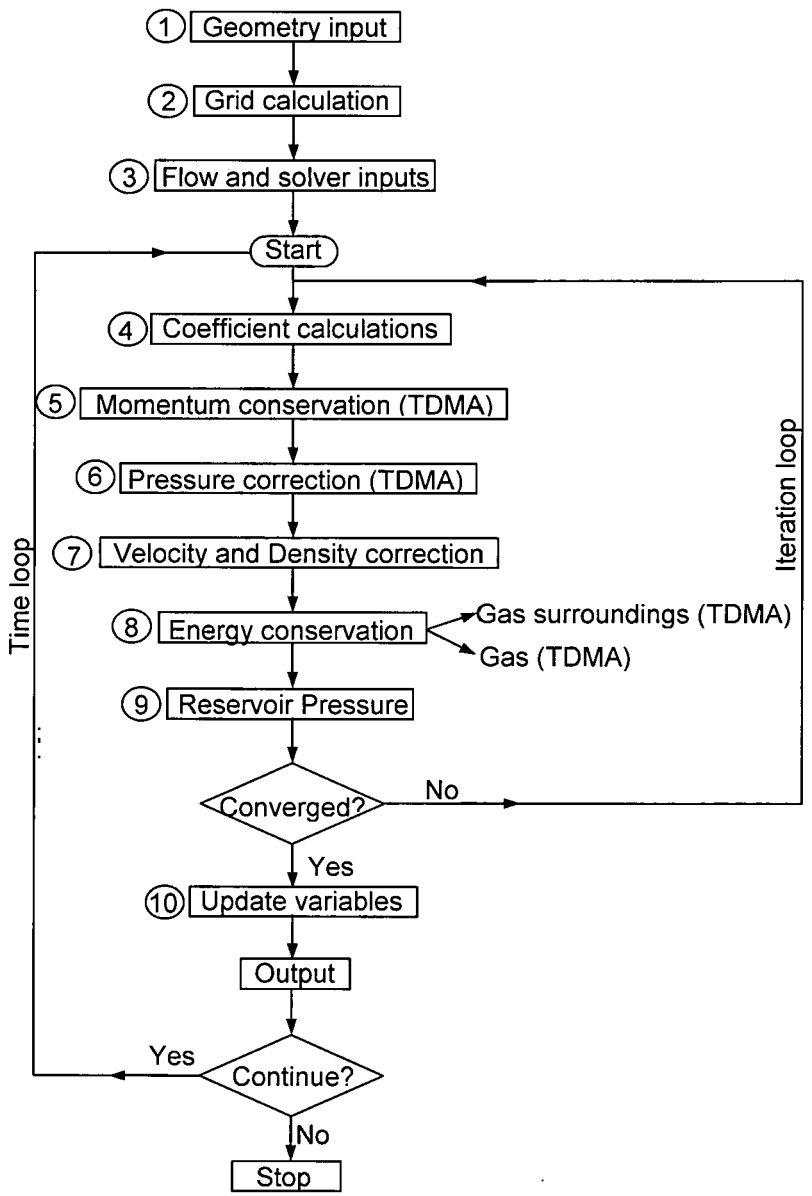


***Figure 4.3*** *Flow chart of the solving process of the CFD simulation*

In step 8 the energy equations for the gas and the gas surroundings are solved. Then in step 9 the pressure at the right hand boundary (reservoir) is calculated. Steps 4 to 9 are repeated until the convergence criteria are satisfied. The variables are updated and the output is written in the form of a text file before it continues to the next time layer.

For stability and consistent discretization of the transition from one section diameter to the next, a conical control volume was introduced at these interfaces which can be seen from figure 4.4.

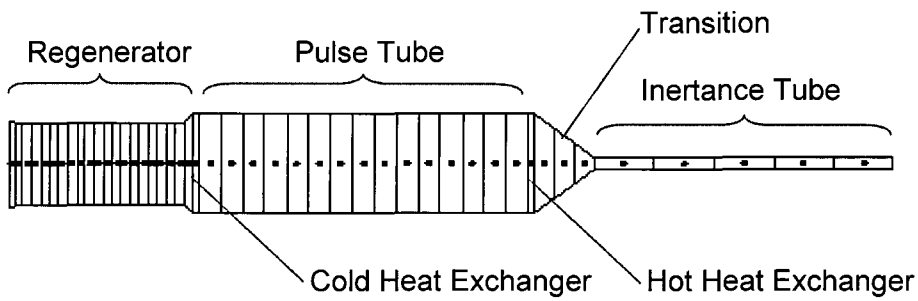


***Figure 4.4*** *Numerical grid of pulse tube cooler model*

## 4.3 Verification and Convergence

The simulation program was verified with simple flow models for which analytical solutions are known. One tube section was simulated at first with flow in both directions and constant pressure difference over its boundaries. The steady state solution of the program was then verified with the analytical solution of various tube sections each with a different diameter and length.

Grid convergence was verified by monitoring the converged solution in the regenerator while increasing the number of control volumes in the pulse tube model. Figure 4.5 indicates grid convergence and shows that the solution tends to converges when the grid is refined.

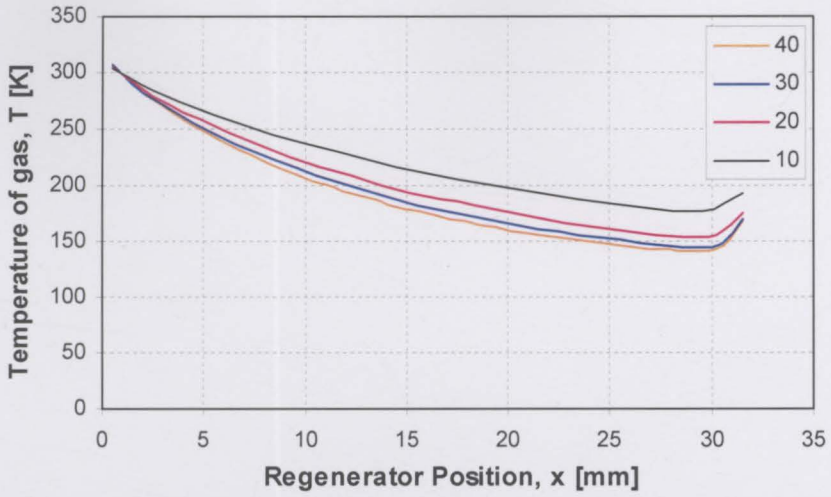


***Figure 4.5*** *Temperature versus position for converged solutions in regenerator for various numbers of regenerator cells, 40, 30, 20 and 10*

## 4.4 Results

The operating principle of an ideal GM-type pulse tube cooler was explained in section 1.4.1. A gas particle was followed during one cycle where it started from a point within the regenerator. The operating principle of the IPTR is somewhat different to the ideal GM-type pulse tube refrigerator and it will now be explained using the simulation program results. The four phases by which it was explained (section 1.4.1) will now be revisited and modified to explain the operation principle of the IPTR. The pressure wave and the velocity (mass flow) are shown in figure 4.5. Multiple plots of the diameter, time, pressure and temperature versus position of the particle in the regenerator and pulse tube is shown in figure 4.6.

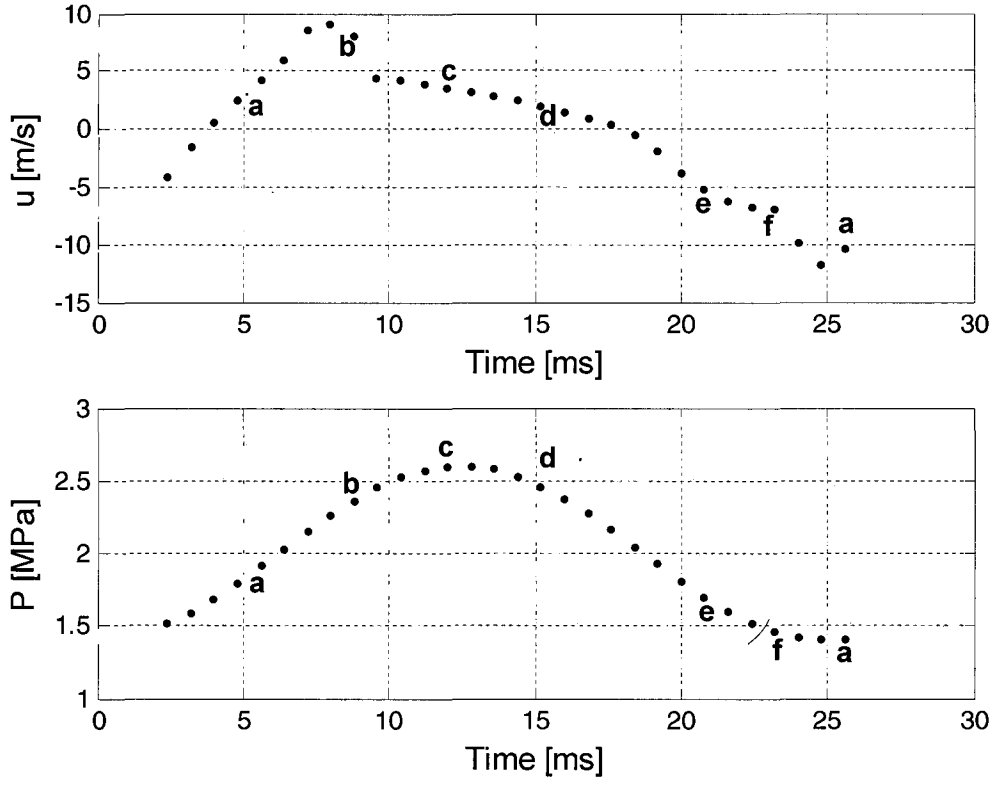


***Figure 4.6*** *Pressure and velocity versus time of the gas particle inside the cooler during one cycle.*

It can be seen from the time versus position graph in figure 4.6 that the particle starts off some distance inside the regenerator then moves through the regenerator, hot heat exchanger and into the pulse tube. It then moves almost to the middle of the pulse tube before it returns back to where it came from initially in the regenerator.

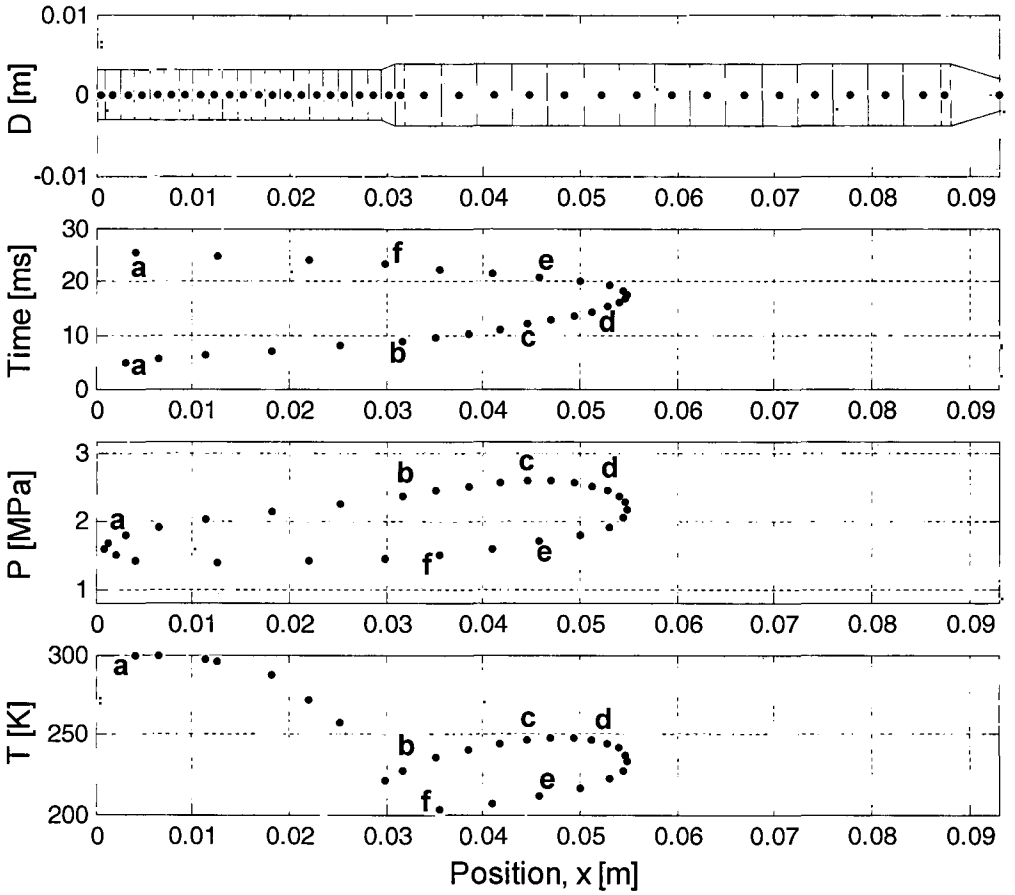


***Figure 4.7*** *Diameter, time, pressure and temperature versus position in the regenerator and pulse tube for a gas particle during one cycle*

### 4.4.1 Operating Principle of the Non-ideal IPTR

*Phase 1:* The gas particle moves from point **a** via **b** to point **c**. During the first part of the compression phase the gas particle moves through the regenerator towards the heat exchanger. This movement is due to the fact that the piston is forcing more gas into the system. Work is done on the gas particle and its pressure increases while its temperature decreases due to heat exchange with the regenerator. The gas particle then leaves the heat exchanger and enters the tube at the temperature of $T_L$ at point **b**. At this point a discontinuity in the velocity wave can be seen in figure 4.6. There is a sudden decrease in velocity due to the sudden increase in the flow area when it enters the pulse tube. From **b** to **c** the gas particle is compressed near adiabatically, while it moves towards the inertance tube. Its temperature increases together with its pressure. During this phase very little gas is flowing into the reservoir via the

inertance tube, because the initial pressure difference across the inertance tube is small.

*Phase 2:* The gas particle moves from **c** to **d** at almost constant pressure and temperature. At this stage the pressure difference between the pulse tube and the reservoir is at a maximum and gas flows through the inertance tube into the reservoir.

*Phase 3*: The gas particle moves from **d** to **e** and back towards the heat exchanger. It can be seen from figure 4.6 that the velocity is still positive during the first part of this phase although the pressure is decreasing. This is because the pressure in the pulse tube is still higher than the pressure in the reservoir and gas flows from the pulse tube into the reservoir. It is clear that the flow lags the pressure and there is a slight phase difference between the mass flow and the pressure. This is ideal, because the particle needs to be moved away from the regenerator before expansion takes place so that the expansion occurs mostly inside the pulse tube like the ideal GM pulse tube cooler.

During the second part of this phase the flow direction reverses because the pressure in the pulse tube has dropped further and is lower than the pressure in the surge volume. The pressure decreases near adiabatically together with the temperature. The gas particle is still inside the pulse tube after expansion, because of the flow which occurred previously. The temperature of the particle is now lower than $T_L$ (point **b**) because it is at a lower pressure and because of the heat rejection to the regenerator at the first part of the compression phase (phase 1).

*Phase 4:* The gas particle moves from **e** via **f** and back to its starting point, **a**. From **e** to **f** the particle is still inside the tube while the piston moves back further to its minimum. The temperature and pressure decreases slightly more. The pressure is now at its minimum in the pulse tube and gas flows from the reservoir into the pulse tube. At point **f** the gas particle enters the heat exchanger at a temperature lower than $T_L$ and therefore heat is absorbed

by the gas particle and its temperature rises to $T_L$. The same discontinuity is visible in the velocity like point b because of the area decrease from the pulse tube to the regenerator. The gas particle then moves into the regenerator back to its original starting point **a** and absorbs heat from the regenerator.

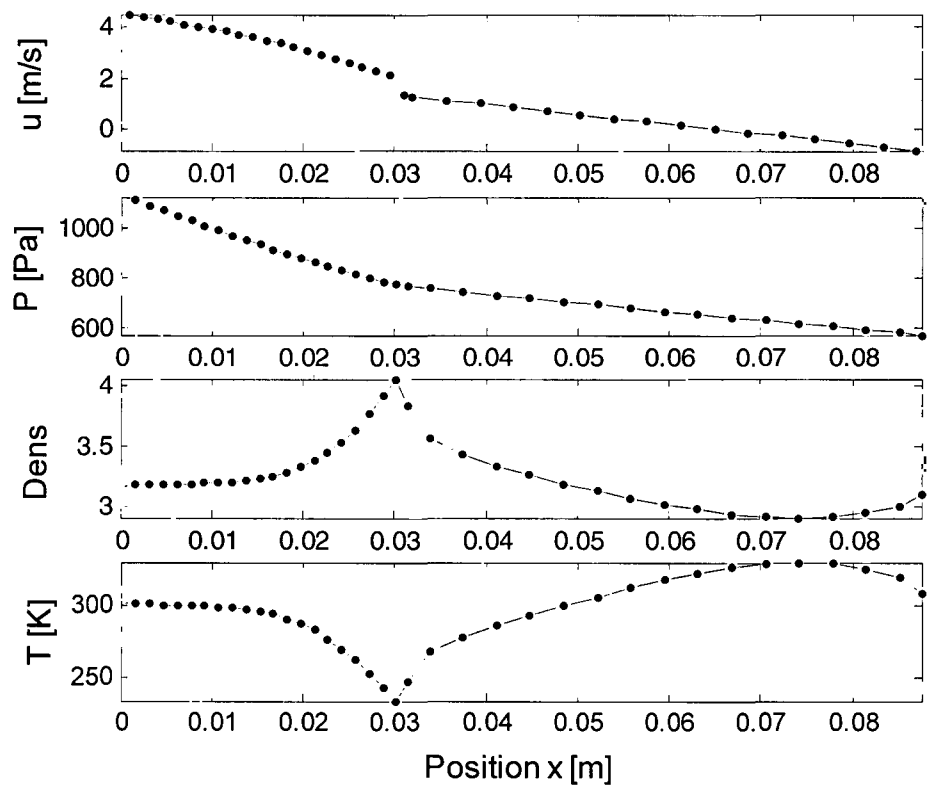


***Figure 4.8*** *Velocity, pressure, density and temperature versus position in the regenerator and pulse tube at an instance after some cooling has taken place*

Figure 4.7 is plotted during the start of the compression, phase 1. It can be seen from the velocity plot in figure 4.7 that the velocity is positive at the beginning of the pulse tube ($x = 0.03$) and negative at the end of the pulse tube ($x = 0.09$). The positive flow at the beginning of the pulse tube is because of the reciprocator forcing gas into the cooler and pulse tube. The negative flow at the end of the pulse tube is due to the phase shift effect caused by the inertance tube. The pressure inside the reservoir is still higher than the pressure inside the pulse tube and gas flows from the reservoir into the pulse tube. This phase shift effect can also be seen from figure 4.6. The velocity, $u$ lags the pressure, $p$ by about 30 degrees which is the ideal phase

shift at the cold heat exchanger for a pulse tube cryocooler (Radebaugh, 2000).

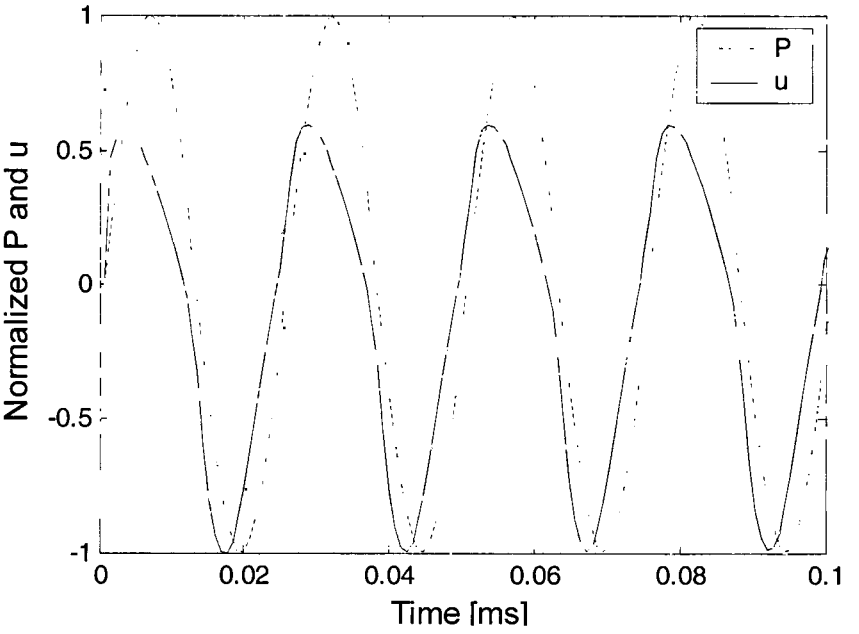


***Figure 4.9*** *Normalized pressure and velocity versus time for the gas inside the cold heat exchanger*

# 5 EXPERIMENTAL EVALUATION

The reciprocator and cold finger are evaluated experimentally to validate the design and mathematical model which was discussed in sections 2 and 3. Experimental results can identify shortcomings in the mathematical model and bring about a new understanding of the particular design. Empirical relations that are proved to be accurate can replace analytical relations where applicable. The experimental evaluation of the reciprocator is explained in two sections, the characteristics tests and the performance tests which will now be explained. Thereafter the cold finger performance tests will be discussed.

## 5.1 Reciprocator Characteristics

The reciprocator characteristics namely the spring constant of the flexures, the magnetic flux density in the coil and the coil inductance is determined experimentally. A description of the reciprocator characteristics tests together with the generated voltage and piston position measurement will be given in the following section.

### 5.1.1 Linear Bearings Spring-constant, $k_s$

The reciprocator is enclosed in a helium tight container when completely assembled and it is not possible to access the moving plunger in order measure its displacement. Therefore, the tests on the flexures were performed on a partially assembled reciprocator. The displacement of the plunger in the axial direction results in a force in the opposite direction due to the stiffness of the flexures and the magnetic forces between the lamination stack and the magnet.

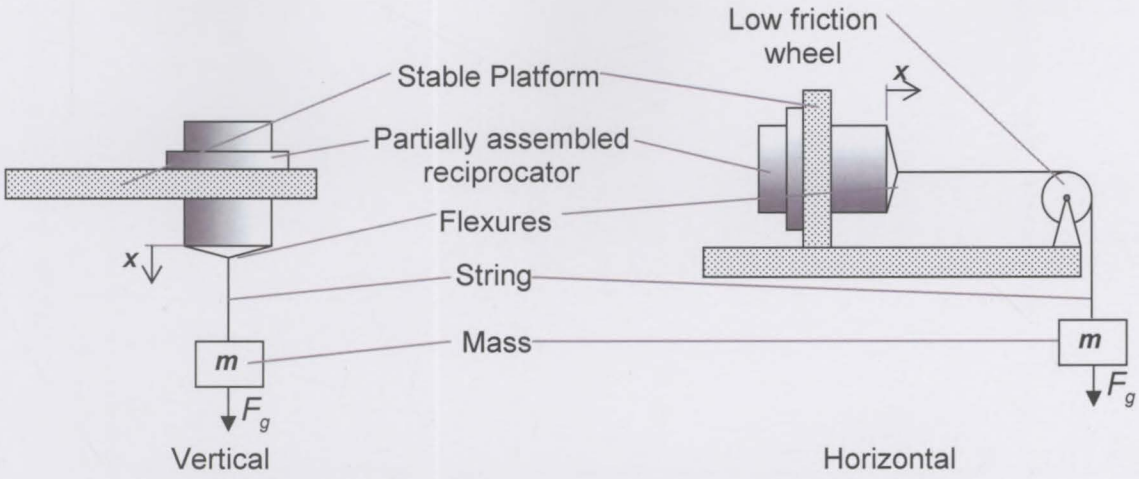


***Figure 5.1*** *Vertical and horizontal flexure testing setup*

The partially assembled reciprocator was clamped to a stable platform as can be seen from figure 5.1. A piece of string connected the moving cylinder to a metal tray of known mass, m. The string was passed over a low friction wheel (pulley) in the case of the horizontal setup. Mass pieces were then added to the tray and the corresponding displacements of the flexures were measured by hand with a vernier calliper. The test was conducted in both a vertical and horizontal configuration (figure 5.1) in order to determine whether the friction on the wheel has a significant influence. The magnet was removed and the tests were repeated. This is necessary to eliminate the effect of the attraction between the lamination stack and the magnet.

The results shown in figure 5.2 are both for the vertical and horizontal configurations and it was found that the friction on the wheel was unelectable in this case. The relations for the force $F$ as a function of displacement are given in figure 5.2 for both cases namely with and without the magnet. It can be seen from figure 5.2 that the spring constant $k_s = F/x$ for the flexures is not constant. In figure 5.2 it is also seen that the difference between the setup with, and the setup without, the magnet is about 10 N at a displacement of 10 mm.

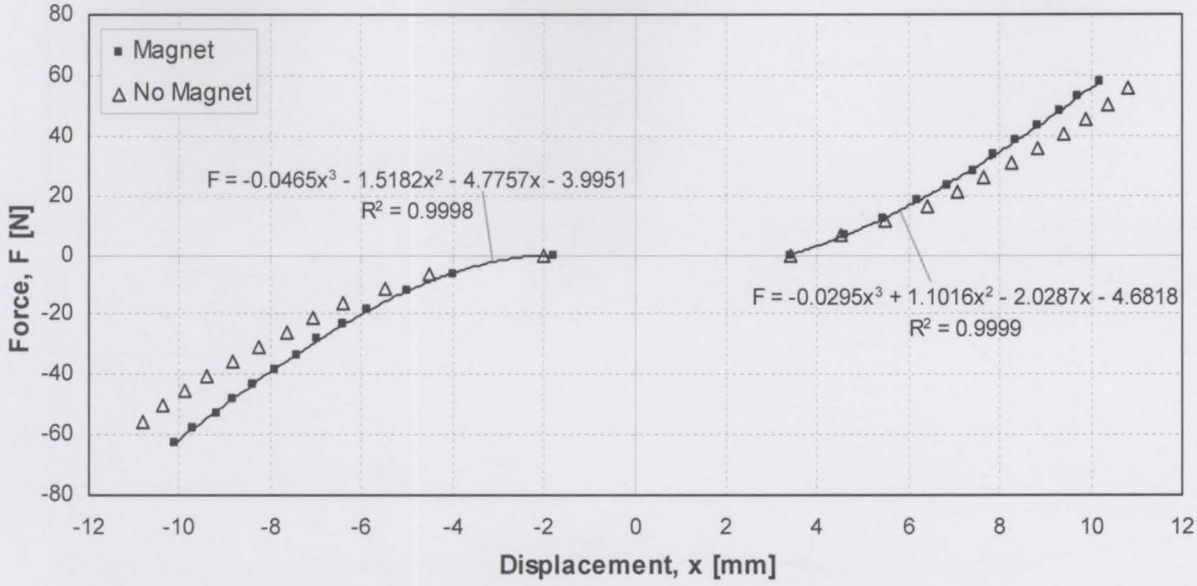


***Figure 5.2*** *Force-displacement curve for linear bearings*

### 5.1.2 Average Magnetic Flux-density in Coil, $\overline{B}$

The average flux density over the coil is determined empirically to validate the results of the finite element model and the analytical model for the magnetic field strength. This test was also conducted in a horizontal and vertical position.

The same apparatus was used for these tests with one addition and that is that a known voltage was applied to the coil of the reciprocator. The voltage was applied using a Tektronix TDS 2014 DC voltage supply. The voltage was kept constant, mass pieces were added and the displacement measured. The electromagnetic force $F_m$ is calculated from equation 5.1 and the average magnetic flux density $\overline{B}$ in coil using equation 3.8.

$$F_m = F_{mg} - F_s \tag{5.1}$$

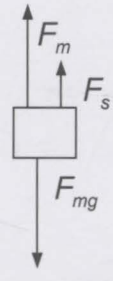


***Figure 5.3*** *Forces diagram of the moving plunger*

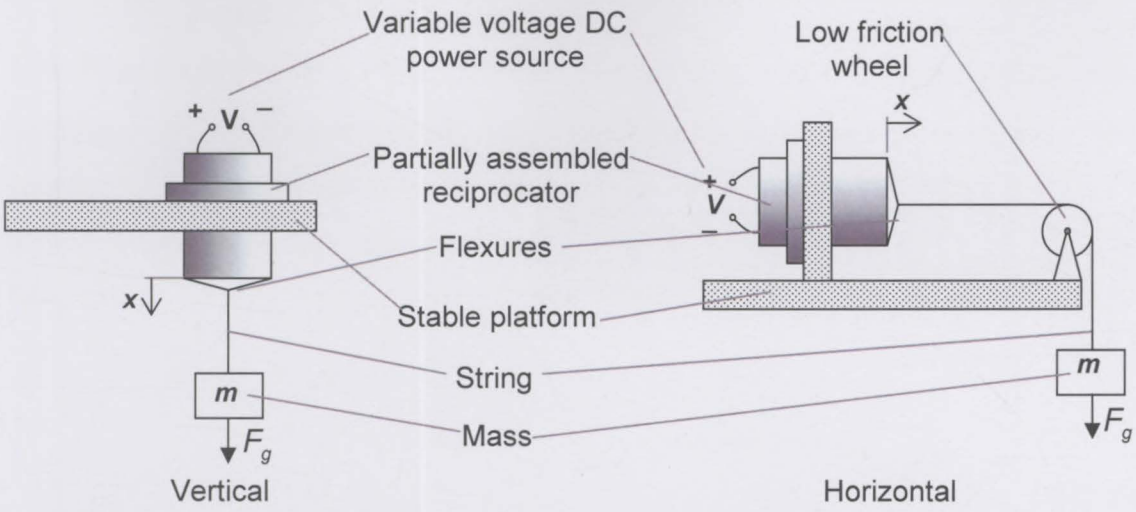


***Figure 5.4*** *Linear motor testing setup in vertical and horizontal positions*

The average flux density $\overline{B}$ as calculated from equation 3.8 is given in figure 5.5 for both the horizontal and vertical configurations. It is assumed that the asymmetry of the graph is due to the attachment holes in one of the mild steel rings shown in figure 2.1. Non-magnetic stainless steel fasteners were used to attach the stationary magnet assembly to the housing. The results from the FEM model are also shown in figure 5.5 and correspond well with experimentally correlated results except where the data deviates from symmetry as just explained.

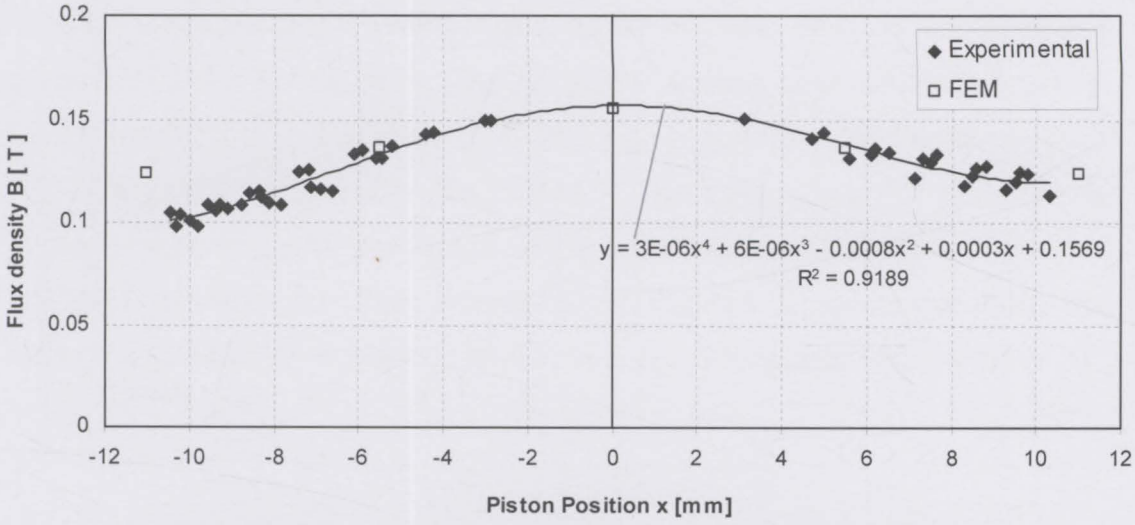


***Figure 5.5*** *Calculated flux density versus piston position*

### 5.1.3 Coil Inductance, *L*

There exists a phase shift $\phi$ between the voltage and the current in an AC inductive circuit where the current lags the voltage as shown in figure 5.6. The relation for the inductance of the coil is given in equation 5.2 (Boctor, *et al.*, 1997) where $R$ is the electrical resistance of the coil and $f$ the operating frequency.

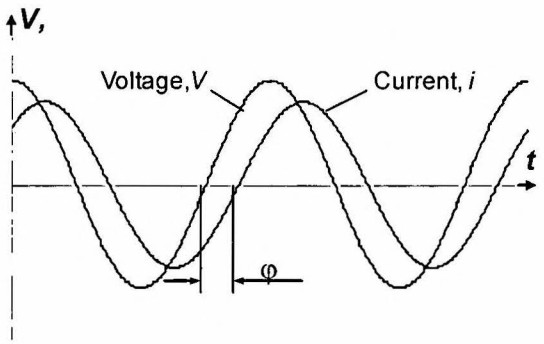


***Figure 5.6*** *Voltage and current wave forms for an inductive circuit*

$$L = \frac{R \tan \phi}{2\pi f} \tag{5.2}$$

The coil inductance was tested before the moving plunger was assembled into the reciprocator. The test setup (figure 5.7) is a simple series circuit where a 1 ohm resistor is connected in series with the coil and an AC power source with variable frequency. The AC power source consists of a sinusoidal signal generated by a Tektronix CFG 250 signal generator and amplified with a 12 V Targa DC car amplifier (Tag 2080C). The voltage over the resistor and the power source, and the phase angle was measured using a Tektronix TDS 2014 oscilloscope. The inductance of the coil is calculated from the readings and equation 5.2 and is shown in figure 5.8 as Exp 1 (experiment 1).

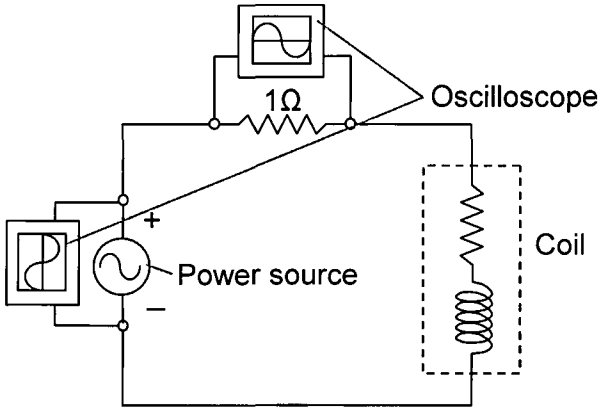


***Figure 5.7*** *Coil inductance testing setup*

The phase shift can also be calculated from the performance tests explained in section 5.2. The performance tests were run at different frequencies and at different charge pressures. The RMS values of the voltage and current, and the power input was measured with a Tektronix TDS 3014 oscilloscope. The relation for the phase angle as a function of RMS voltage, RMS current and input power is given in equation 5.3 (Boctor, *et al.*, 1997). The inductance was then calculated for the coil during operation and is given in figure 5.8 as Exp 2 (experiment 2).

$$\phi = \cos^{-1}\frac{P}{Vi} \tag{5.3}$$

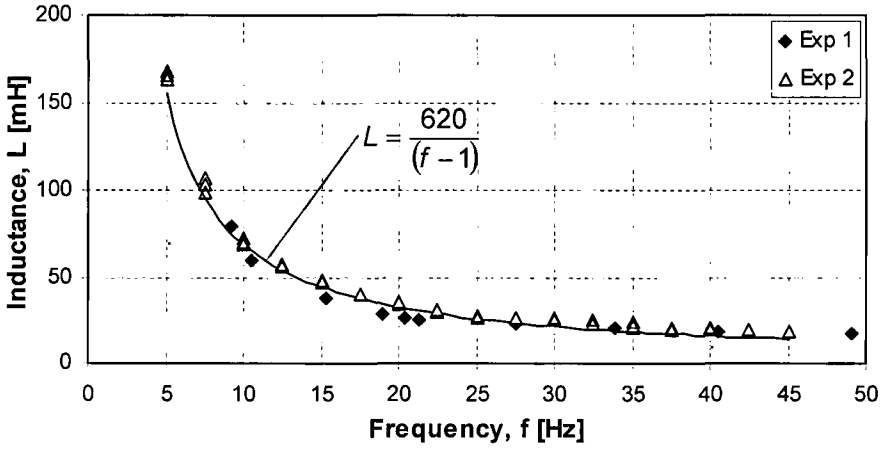


***Figure 5.8*** *Graph showing coil inductance versus frequency*

It can be seen from the results shown in figure 5.8 that the inductance varies extensively between the 10 Hz and 20 Hz region. The inductance calculated from experiment 1 (Exp 1) and experiment 2 (Exp 2) corresponds well. A slight deviation between the two experiments can be seen between 10 Hz and

30 Hz region. The inductance can thus be accurately approximated by the following experimentally correlated relation:

$$L = \frac{620}{f - 1} \tag{5.4}$$

### 5.1.4 Piston Position Measurement

The position of the piston is measured with two strain gauges which were attached to opposite sides of the moving spring steel flexures. The strain gauges were connected to a bridge amplifier in a half Wheatstone bridge configuration so as to compensate for temperature changes.

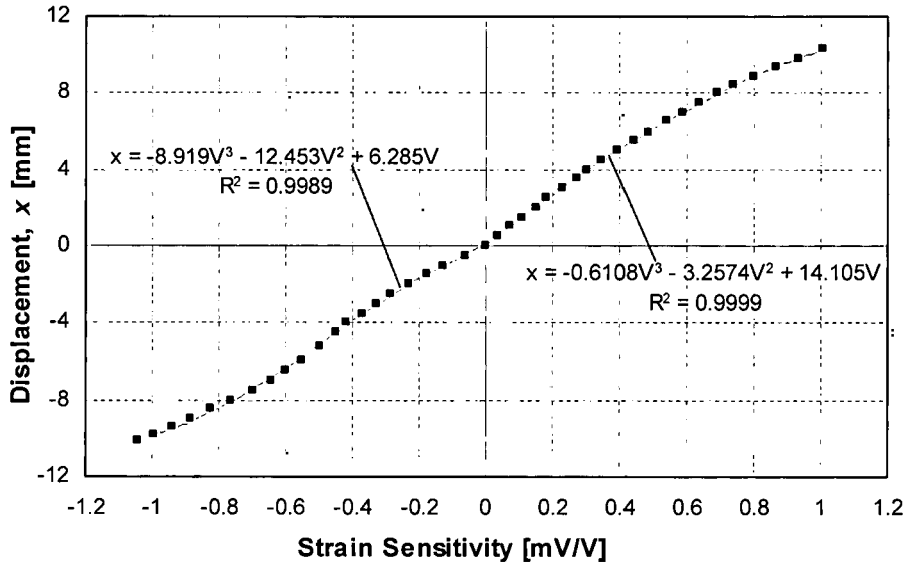


***Figure 5.9*** *Strain gauge calibration curve for displacement*

Figure 5.9 shows the graph of displacement versus strain. It can be seen that the relation between strain and displacement is almost linear. The deviation from a linear relation is due to the fact that the flexures were not only subjected to pure bending, but also twisting. Two curves were fitted through the data, one for positive and one for negative displacement and are shown in figure 5.9.

### 5.1.5 Generated Voltage

The reciprocator is not only an electrical drive, but also an electric generator. A potential difference can be measured over the terminals of the reciprocator when in an open circuit configuration and the plunger is moved by an external force. This potential difference is known as the generated voltage (Boctor et

al., 1997). As no current is flowing in the coil because of the open circuit, equation 3.9 reduces to:

$$V = \overline{B}\ell u \tag{5.5}$$

A Tektronix TDS 2014 oscilloscope was connected over the two terminals of the reciprocator (figure 5.10). The Reciprocator was clamped in a stable platform and the coil of the reciprocator is displaced by hand to cause a near sinusoidal displacement versus time. The potential difference over the reciprocator terminals and the resulting voltage from the bridge amplifier of the strain gauges was recorded with respect to time.

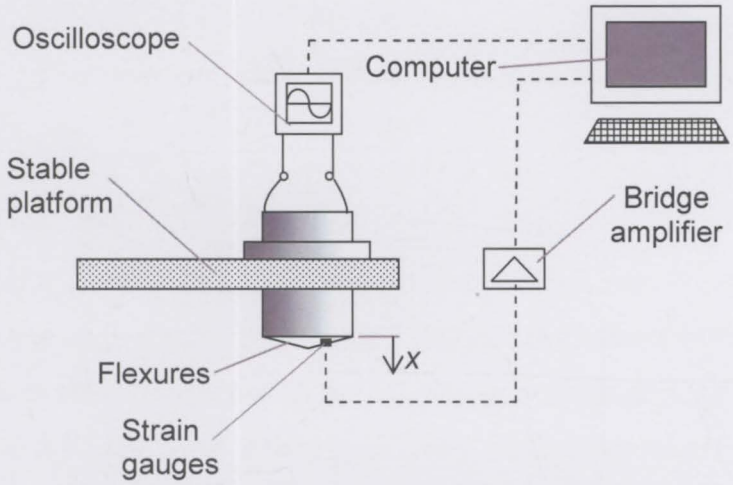


***Figure 5.10*** *Generated voltage test setup*

The velocity of the moving plunger can be calculated from the displacement versus time graph figure 5.11. The generated voltage can then be calculated from equation 5.5 when the plunger velocity and the empirical relation for the magnetic flux density (figure 5.5) are known. Figure 5.11 shows the generated voltage versus time for both the simulated and experimental data. The simulated and experimental results for the generated voltage correspond well.

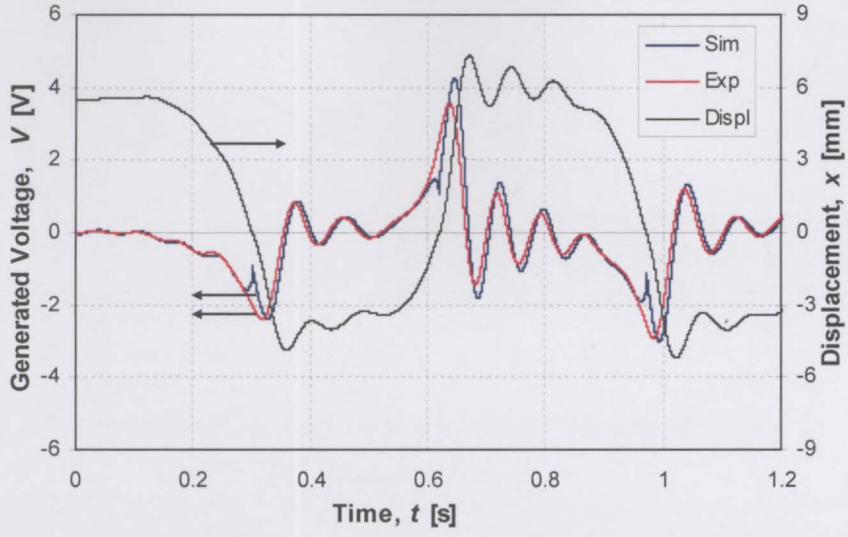


***Figure 5.11*** *Displacement and generated voltage versus time for hand-moved plunger*

## 5.2 Reciprocator Performance

Two reciprocator performance tests were conducted. The first was the open setup, where the reciprocator was tested without the piston being assembled. The linear motor was connected to an AC power source and the displacement of the moving plunger was measured with calibrated strain gauges. The second reciprocator performance test is the closed setup where the piston is assembled, the reciprocator closed and charged with helium.

### 5.2.1 Open Setup

The aim of this experiment is to investigate the accuracy of the mathematical model in the solving of the two governing equations which are the equation for the voltage (equation 3.9) and the equation of motion (equation 3.1).

The same experimental setup was used as in the previous section (figure 5.10). The current was measured with a Tektronix TCP 202 current probe connected to a Tektronix TDS 3014 oscilloscope which set up is shown in figure 5.15.

Figures 5.12 and 5.13 show the simulated and experimental data for the displacement and current versus time for frequencies of 10 and 15 Hz.

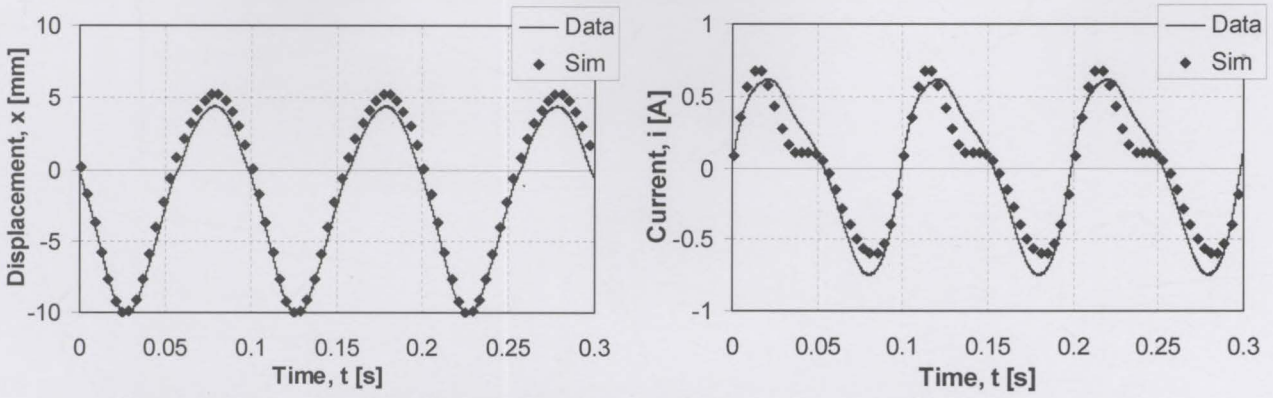


***Figure 5.12*** *Graphs of displacement and current versus time for a frequency of 10Hz and a maximum voltage of 8.5 V*

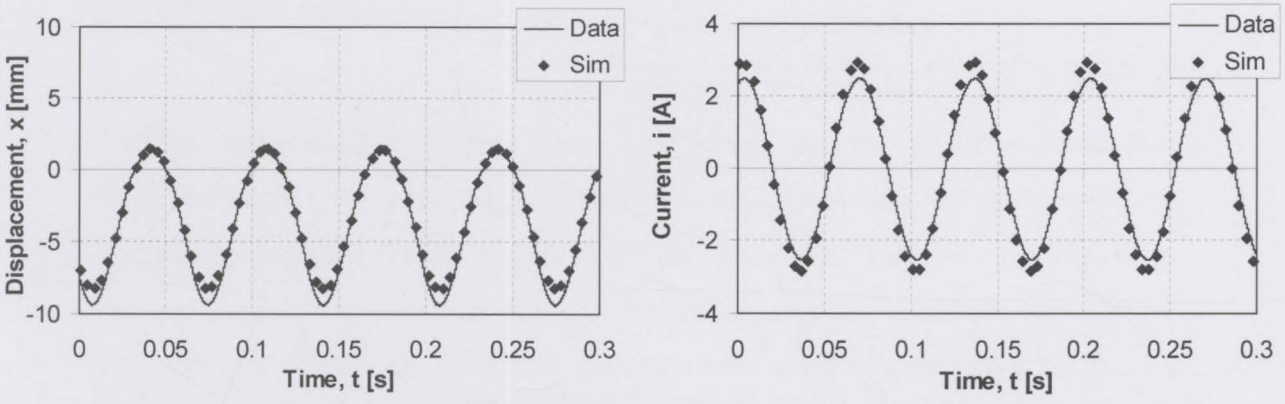


***Figure 5.13*** *Graphs of displacement and current versus time for a frequency of 15Hz and a maximum voltage of 12V*

### 5.2.2 Closed Setup

The reciprocator is completely assembled, connected to the pressure chamber and charged with Helium. A sinusoidal voltage is applied to the terminals of the reciprocator. The frequency is adjusted and fixed before each run and then the absolute pressure, voltage and current is measured versus time. The input power was calculated from the voltage and current with the multiplication function of a Tektronix TDS 3014 oscilloscope. The applied voltage was adjusted during each run so that the input power is equal to 10 W.

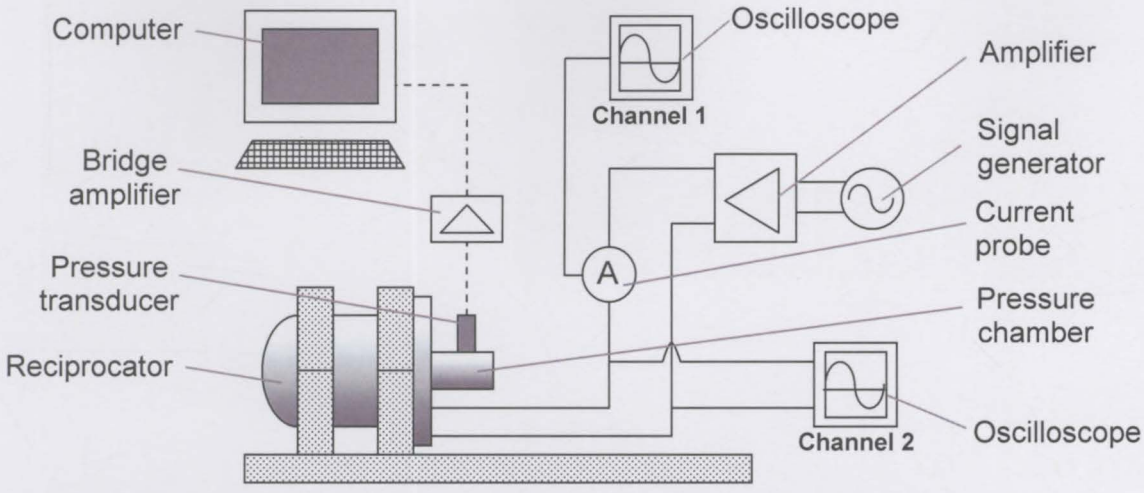


***Figure 5.14*** *Testing setup for reciprocator performance testing*

The volume of the pressure chamber is 4 $cm^2$ and is calculated to be equal to the total volume of the pulse tube, split tube, and the dead volume of the regenerator and the heat exchanger. The pressure chamber is connected to the reciprocator via the threaded split tube hole and is sealed with an o-ring. The pressure is measured with a P8-type Hottinger Baldwin Messtechnik pressure probe with an accuracy of ±2% which is connected via a bridge amp to a computer. The current is measured with a Tektronix TCP202 current probe connected to a TDS3014 Tektronix oscilloscope. The voltage and frequency is measured, and the input power is calculated with the multiplication function of the oscilloscope. Figures 5.15, 5.16 and 5.17 show the absolute pressure versus time for frequencies of 10, 20 and 30 Hz. It can be seen that the pressure amplitude decreases with an increase in frequency.

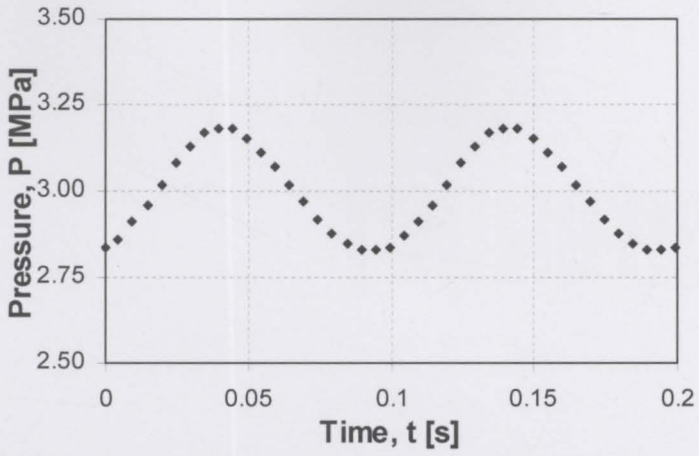


***Figure 5.15*** *Absolute pressure versus time for a frequency of 10 Hz and applied voltage of 10.6 V*

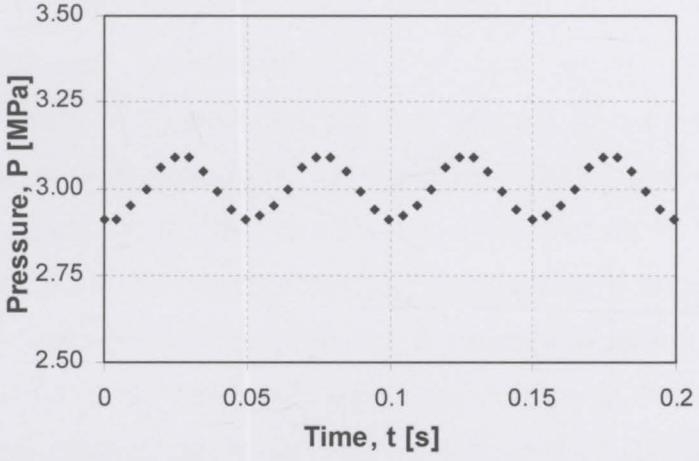


***Figure 5.16*** *Absolute pressure versus time for a frequency of 20 Hz and applied voltage of 9.6 V*

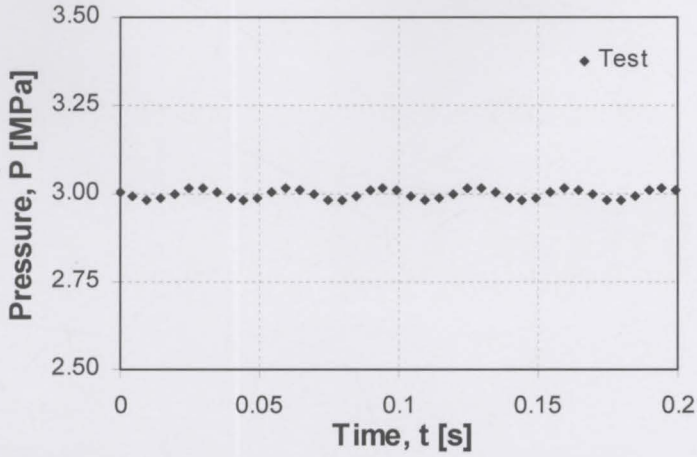


***Figure 5.17*** *Absolute pressure versus time for a frequency of 30 Hz and applied voltage of 9V*

## 5.3 Cooler Performance

The cryocooler was assembled with the cold finger connected to the reciprocator (figure 5.18) and charged with Helium to a pressure of 3 Mpa. The reciprocator was connected to the power amp, driven by the signal generator. A schematic of the setup for the cryocooler performance testing is shown in figure 5.19. The cold finger was enclosed in a vacuum chamber to minimise heat flow from the environment. A vacuum feed-though was used to connect the wires of the thermocouple to the cold point through the vacuum enclosure. The thermocouple was connected to the computer via a data logger. Figure 5.20 illustrates a photo of the cryocooler testing setup. Two performance tests were conducted will now be explained.

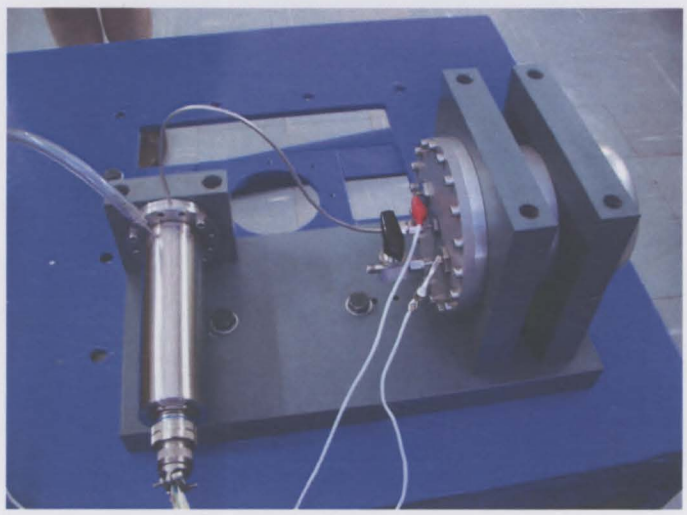

***Figure 5.18*** *Picture of complete cryocooler during performance testing*

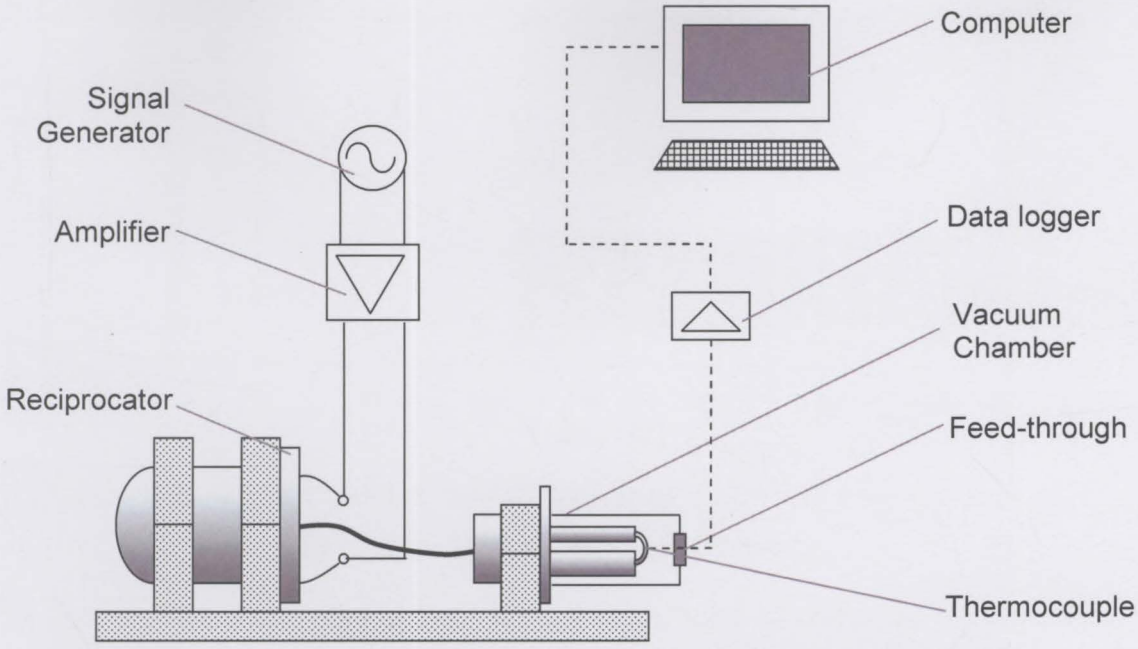


***Figure 5.19*** *Schematic of testing setup for cooler performance testing*

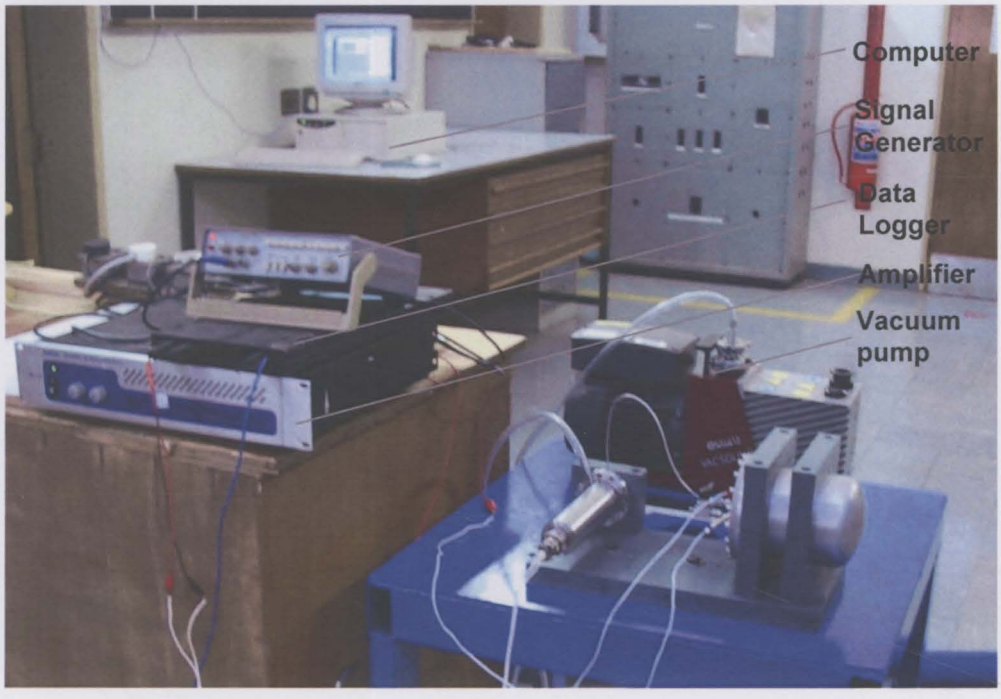


***Figure 5.20*** *Picture of cooler performance testing setup*

An inertance tube with a diameter of 0.6 mm and a length of 30 mm was attached for the first performance test, and the cryocooler charged with Helium at 3 MPa. The cryocooler was run at 20 Hz and the temperature measured with time. The cool-down curve is shown in figure 5.21 and a temperature of 220 K was obtained.

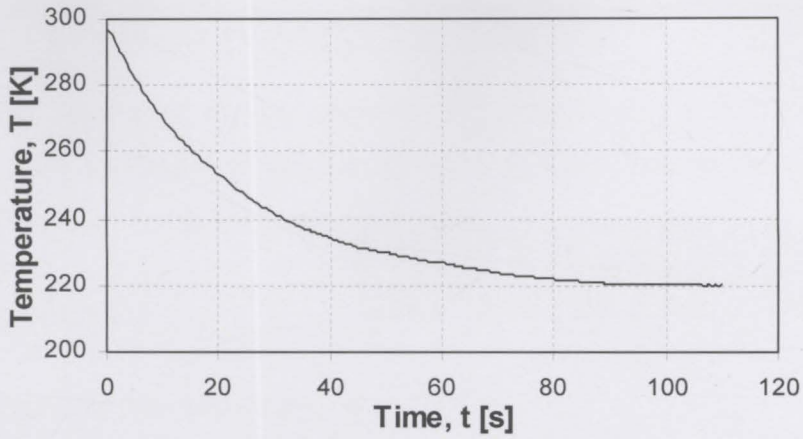


***Figure 5.21*** *Cool-down curve of cryocooler for 20 Hz with inertance tube of diameter 0.6 mm and length 30 mm*

For the second performance test, an inertance tube of diameter 0.6 mm and length of 20 mm was used and a pressure of 3 MPa Helium. The cryocooler was run and the frequency adjusted every 100 seconds while the temperature was measured with time. The cool-down curve for the second performance test is shown in figure 5.22. A minimum temperature of 180 K was reached for this setup.

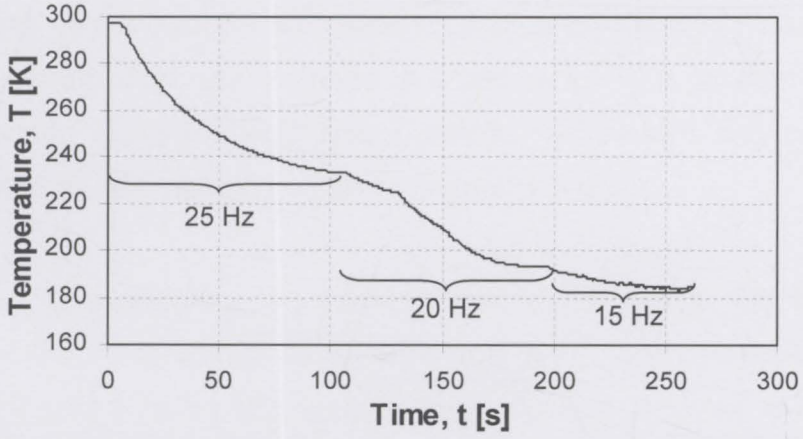


***Figure 5.22*** *Cool-down curve of cryocooler driven at 15, 20 and 25 Hz with inertance tube of diameter 0.6 mm length 20 mm*

# 6 DISCUSSIONS AND CONCLUSIONS

The project is discussed in two sections, the reciprocator and the cold finger. Conclusions will be drawn at the end of each section. The reciprocator will be discussed first and thereafter the cold finger.

## 6.1 Reciprocator

### 6.1.1 Design and Manufacture

The force versus displacement relation for the flexures is not linear and the stiffness is practically zero for displacements smaller than 4 mm. Small fatigue cracks were visible on the flexures after the tests were completed on the reciprocator. The fatigue cracks developed due to stress concentrations inside the flexures. The flexures need to be redesigned by doing a thorough FEM analysis to minimize the stress concentrations. The only real success of the flexures was their accurate assembly and manufacturing where a non-contact operation was achieved for a stroke of 15 mm and a gap of 30 microns.

The vibration of the reciprocator was a bit of a problem to deal with even though the reciprocator was clamped to a test bench. It is recommended that a dual opposite (coaxial) reciprocator, where two pistons are running 180 degrees out of phase, should be used in future designs.

The concept of connecting the one terminal of the coil to the reciprocator body, using the reciprocator as an electrical earth, worked well. Only one feed-through and moving connection was required. Another design which should be investigated is the moving magnet configuration for the linear motor. The advantage of this design is that no moving connections (flying leads) are required and that the coils could be situated outside the Helium tight environment of the reciprocator. This will eliminate the chances of compressor contamination due to out-gassing of the coil.

### 6.1.2 Linear Motor

The reason why the moving core of the linear motor is laminated is to reduce the eddy current losses in the moving core. Eddy currents will occur in the moving core due to a dynamic change of magnetic field. The laminated core consists of 0.5 mm thick electrically insulated soft iron rings which are stacked to form a cylindrical core. This type of lamination only reduces eddy current losses caused by the change of magnetic flux in the radial direction $\phi_r$ (figure 6.1). It can be seen from figure 6.1 that the majority of the magnetic flux in the moving core is orientated in the axial direction ($\phi_a$). Therefore eddy currents would occur in the moving core due to changes of magnetic flux in the axial direction. This means that the lamination of the core is orientated in the wrong direction and that extensive eddy current losses would occur in the moving core. In addition the electric insulation between the rings of the laminated core worsens the situation because it adds to the magnetic reluctance of the magnetic circuit. Therefore the lamination of the moving core has no positive function and a solid piece of moving iron would have been just as good. The correct orientation of the core lamination is in the radial direction which will reduce eddy current losses in the core effectively.

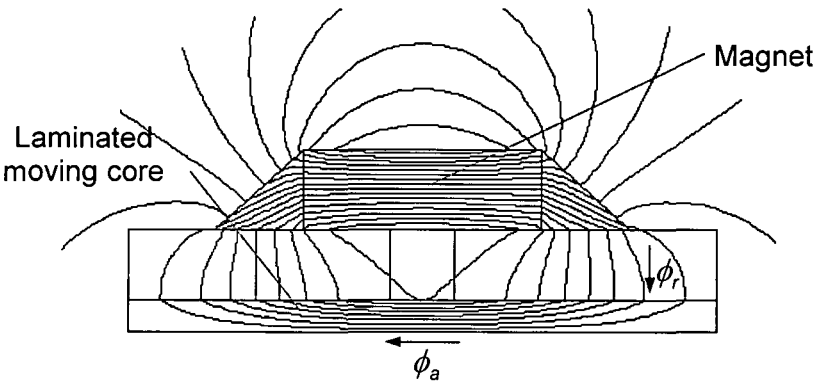


***Figure 6.1*** *Diagram showing the directions of the magnetic flux in moving core*

### 6.1.3 Eddy Current Hypothesis

It was found that the reciprocator could be modelled accurately for frequencies below 15 Hz but not for higher frequencies. The performance of the reciprocator was far less than predicted by the mathematical model for the

frequency range between 15 Hz to 50 Hz. Figures 6.2 (a), 6.3 (a) and 6.4 (a) show the experimental and simulated results for the pressure versus the time at frequencies of 10 Hz, 20 Hz and 30 Hz for an input power of 10 W. It can be seen from these figures that difference between the experimental and simulated results increases with the frequency.

The reason for this phenomenon is assumed to be due to eddy current losses present in the moving core of the linear motor which was explained in the previous section. A hypothesis is introduced to determine the magnitude of the eddy current losses in the reciprocator. A flux density loss factor was determined iteratively by adjusting only the flux density in the model. The magnetic flux density was divided by a loss factor which was adjusted until the simulated pressure, current and applied voltage were close to the experimental results. Figures 6.2 (b), 6.3 (b), 6.4 (b) show the results of the simulation (simulation 2) for the pressure versus time after a loss factor (eddy current hypothesis) was introduced. It can be seen that the results of simulation 2 is much closer to the experimental results when compared to the results of the initial model (simulation 1).

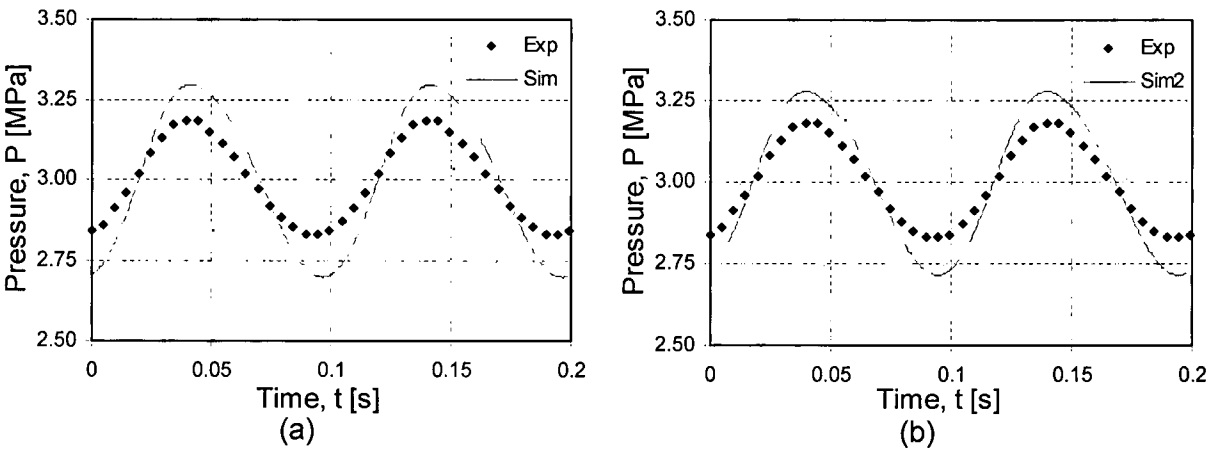


***Figure 6.2*** *Absolute pressure versus time for a frequency of 10 Hz and 10 W input power*

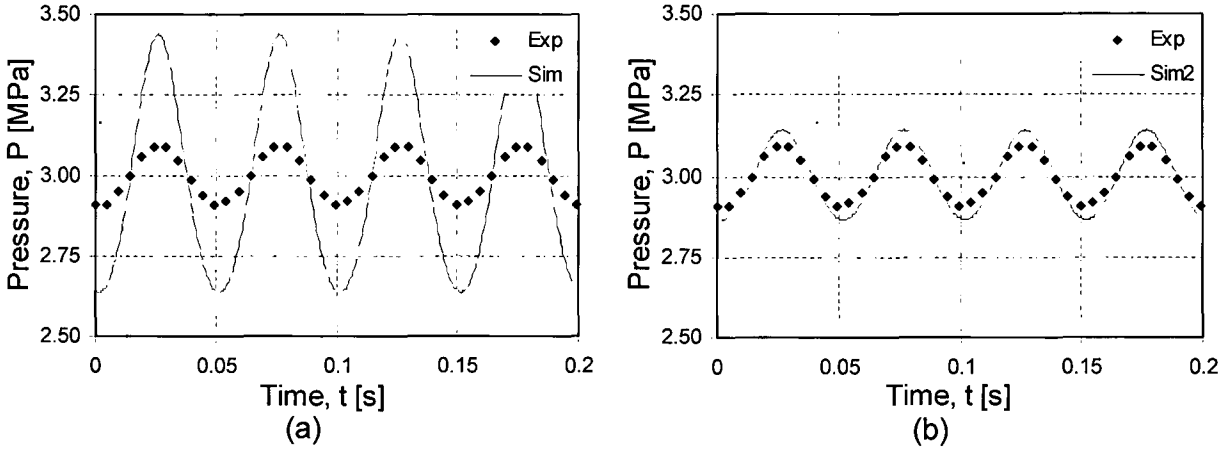


***Figure 6.3*** *Absolute pressure versus time for a frequency of 20 Hz and 10 W input power*

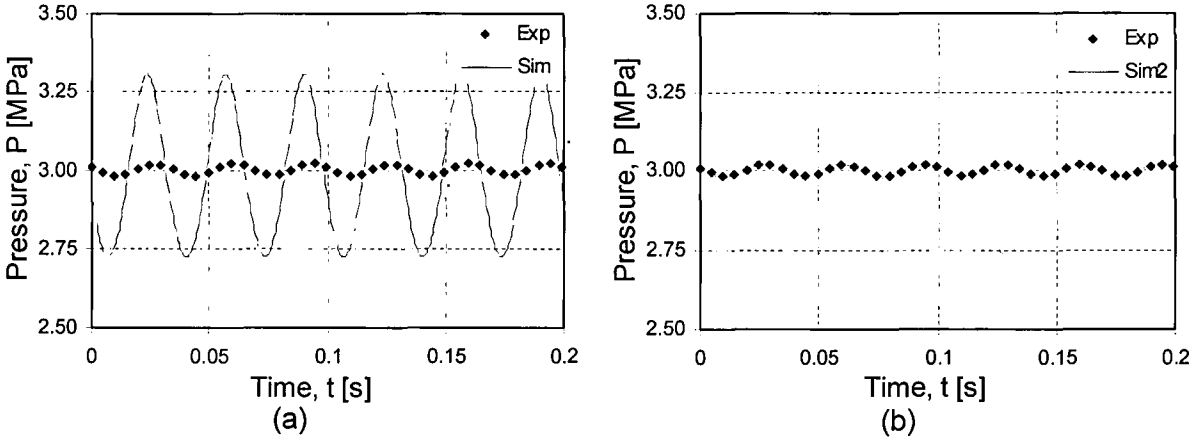


***Figure 6.4*** *Absolute pressure versus time for a frequency of 30 Hz and 10 W input power*

Figure 6.5 (a) shows the experimental results versus simulation 1 and 2 for the pressure amplitude (equation 6.1) versus frequency. The loss factor is plotted versus the frequency in figure 6.5 (b) and it can be seen that it approximates an exponential function. This supports the theory that eddy current losses are to blame for the lack of performance because it is known that eddy current losses also increases exponentially with the frequency (Hughes, 1995).

$$p_{amp} = p - p_{fill} \tag{6.1}$$

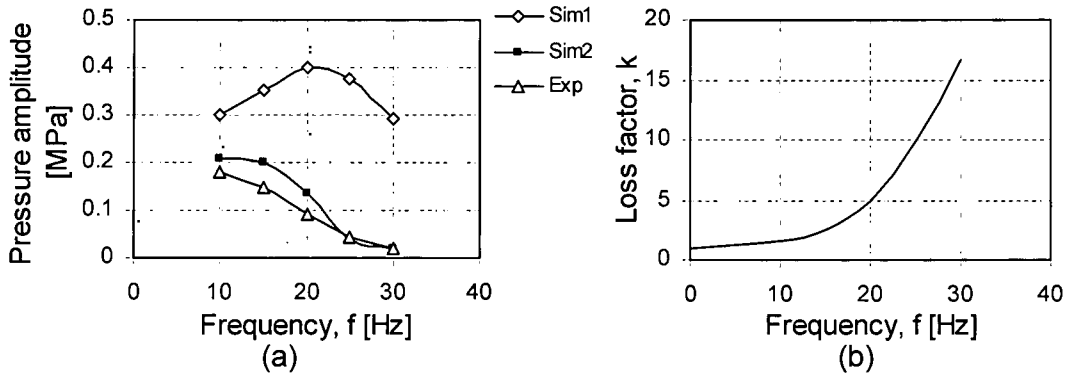


***Figure 6.5*** *Pressure amplitude (a) and loss factor (b) versus frequency*

Figures 6.6 (a) and (b) shows the results of simulation 2 together with the experimental results for the voltage and current versus frequency for an input power of 10 W. It can be concluded from these results that the simulation 2, based on an eddy current hypothesis, can model the reciprocator fairly accurate.

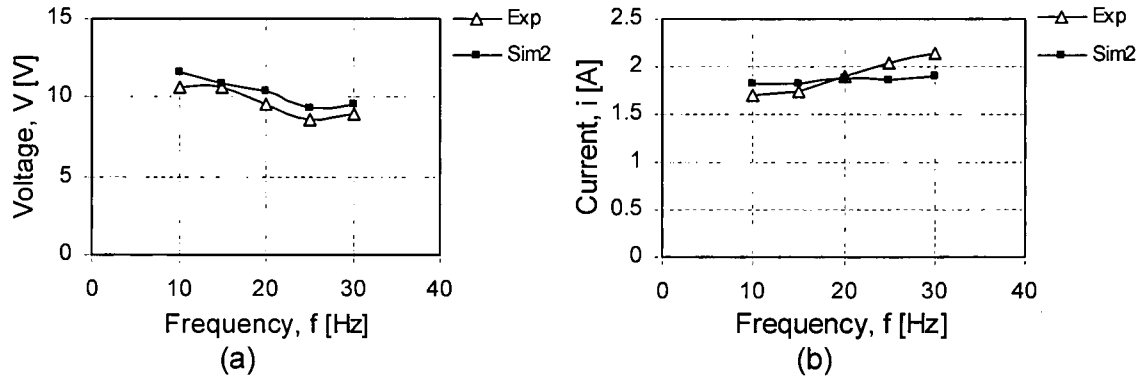


***Figure 6.6*** *Voltage amplitude (a) and current amplitude (b) versus frequency for an input power of 10 W*

### 6.1.4 Natural Frequency

All dynamic spring-and-mass systems with low damping, including the reciprocator, have a natural frequency. At this point the displacement and resulting pressure amplitude is at a maximum.

The relation for the natural frequency of the reciprocator (equation 3.21) is derived in section 3.1.6. Substituting equation 6.1 into equation 3.31 and hence an equation for the natural frequency of the reciprocator (equation 6.2) in terms of the pressure amplitude $P_{amp}$, spring constant $k_s$, displacement $x$, piston area $A_p$ and moving mass $m$. The displacement of the piston was not

measured during the closed reciprocator (Helium charged) tests and was calculated with the simulation program.

$$f_n = \frac{1}{2\pi}\sqrt{\frac{k_s + \frac{p_{amp}A_p}{x}}{m}} \tag{6.2}$$

Table 6.1 lists the variables for the calculation of the natural frequency (equation 6.2) which are the amplitude $x$ and pressure amplitude $P_{amp}$. The calculated natural frequency $f_n$ and the frequencies at which these values were generated are also listed in table 6.1.

***Table 6.1*** *Natural frequency calculation of reciprocator from simulation results*

| Frequency, $f$ | Amplitude, $x$ | Pressure amplitude, $P_{amp}$ | Natural frequency, $f_n$ |
|---|---|---|---|
| [Hz] | [mm] | [Mpa] | [Hz] |
| Simulation1 | | | |
| 10 | 1.82 | 0.3 | 23.6 |
| 15 | 2.10 | 0.35 | 23.8 |
| 20 | 2.39 | 0.4 | 23.7 |
| 25 | 2.25 | 0.38 | 23.7 |
| 30 | 1.76 | 0.29 | 23.6 |
| Simulation 2 | | | |
| 10 | 1.25 | 0.21 | 23.6 |
| 15 | 1.21 | 0.2 | 23.6 |
| 20 | 0.83 | 0.14 | 23.6 |
| 25 | 0.25 | 0.04 | 23.8 |
| 30 | 0.13 | 0.02 | 23.3 |

The calculated natural frequency $f_n$ in table 6.1 is about 23.6 Hz for both simulation 1 and 2 even though their results for the displacement and pressure amplitude differ extensively. In figure 6.5 (a), it can be seen that the pressure amplitude for simulation 1 is at a maximum in the region of 23 Hz as predicted in table 6.1. The experimental results and the results of simulation 2 in figure 6.5 (a) indicate that there is no peak performance at the calculated natural frequency of 23.6 Hz. This lack in performance of the reciprocator is blamed on the eddy current losses in the linear motor. The reason why there is no peak at 23.6 Hz is because the eddy current losses increase exponentially (figure 6.5, b) while the performance of the reciprocator due to resonance only increases linearly at best.

### 6.1.5 Magnet Optimization

The linear motor design is not optimised. The efficiency of the reciprocator could be increased while the mass of the moving coil is decreased by

optimising the magnet configuration in the magnetic circuit. A reduction in the mass of the coil in the moving plunger would decrease the vibrations and copper losses. The optimisation methodology will be explained briefly in the next paragraph.

There exists an operating point for a permanent magnet by which the energy product is maximized and where it is used most efficiently in a magnetic circuit (Nasar, 1998). The optimal operating point of a magnet in a magnetic circuit is the intersection point between the demagnetization curve (*B-H* curve) of a magnet (figure 6.7) and the hyperbola giving the energy product, $B_m H_m$.

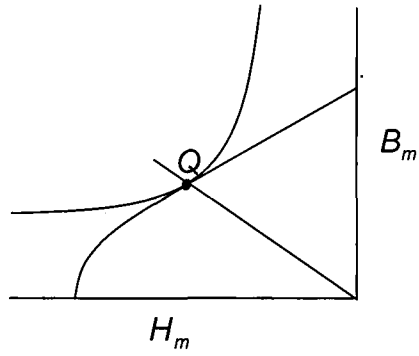


***Figure 6.7*** *Graph showing optimal operating point of a magnet*

### 6.1.6 Conclusions

The reciprocator could be modelled adequately by introducing an eddy current loss coefficient. The accuracy of the model can be determined in future studies once the issue of the eddy current losses is addressed by using the right configuration for the laminations of the moving core.

Good experimental results were obtained; which include the frequency dependant inductance and the generated emf. In the end, substantial know-how was generated in the design and manufacture of a cryocooler reciprocator.

## 6.2 Cold Finger

The mechanical design and manufacturing of the cold finger was satisfactory. The thin-walled tubes could withstand the oscillating pressures while

minimising heat flow from the hot zone to the cold zone. Figure 6.8 shows a picture of the cryocooler cold zone during operation. The thermodynamic design of the pulse tube cryocooler (cold finger) was verified with ARCOPTR (Roach, 2003) which is a simulation program developed by Ames Research Centre, NASA (Roach, 1997). The results showed that this cryocooler has the potential of reaching a minimum temperature of 60 K with a cooling power of 1 Watt. The reasons why the cryocooler only reached 180 K (see figures 5.21 and 5.22), are firstly because it was not optimized, and secondly because of the reciprocator's poor performance. Further testing and optimization is required with a more efficient reciprocator.

***Figure 6.8*** *Picture of cryocooler cold zone during operation*

# 7 REFERENCES

Barron, R F (1999) Cryogenic Heat Transfer, Taylor & Frances, Philadelphia

Boctor, S A et al. (1997) Electrical Concepts and Applications, West Publishing Company, New York

Chan, C K and Nguyen, T (1998) IMAS Pulse Tube Cooler Development and Testing, 10th International Cryocooler Conference

Choi, S, Nam, K & Jeong, S (2004) Investigation on the pressure drop characteristics of cryocooler regenerators under oscillating flow and pulsation pressure conditions, Cryogenics, Vol 44, pp 203-210

De Boer, P C T (2002) Maximum attainable performance of pulse tube refrigerators, Cryogenics, Vol 42, pp 123-125

De Boer, P C T (2002) Performance of the inertance pulse tube, Cryogenics, Vol 42, pp 209-221

De Waele, A T A M, Steijaert, P P & Gijzen, J (1997) Thermodynamic aspects of pulse tubes, Cryogenics, Vol 37, pp 313-324

Finney, L F and Thomas, R L (1990) Calculus, Addison-Wesley, New York

Helvensteijn, B P M, et al: (1998) Pressure Drop over Regenerators in Oscillating Flow, Advances in Cryogenic Engineering, Vol 43 B, pp1619-1626

Hooijkaas, H W G (2000) Miniature Stirling-Type Pulse-Tube Refrigerators, PhD Thesis, Technische Universiteit Eindhoven, Eindhoven

Hughes, E (1995) *Electrical Technology*, Addison Wesley Longman Limited, Singapore

Hughes, T J R, Liu, W K & Zimmerman, T K (1981) Lagrangian-Eulerian Finite Element Formulation for Incompressible Viscous Flows, Computer Methods in Applied Mechanics and Engineering, Vol 29, pp 329-349

Ju, Y L, et al. (2003) System design of 60 K Stirling-type coaxial pulse tube coolers for HTS RF filters, Physica C, Vol 386, pp 540-543

Ju, Y L, Yan, J & Zhou, Y (1998) Experimental study of the oscillating flow characteristics for a regenerator in a pulse tube cryocooler, Cryogenics, Vol 38, pp 649-656

Kanao K, Watanabe N, Kanazawa, Y (1994) A miniature pulse tube refrigerator for temperatures below 100K. Cryogenics, Vol 34, pp 167-170

Kays, W M and London, A L (1984) Compact Heat Exchangers, 3rd ed. McGraw-Hill, New York

Kittel, P and Kashani, A (1996) General pulse tube theory, Cryogenics, Vol 36, pp 849-857

Koh, D Y, et al. (2002) A study on the linear compressor characteristics of the Stirling cryocooler, Cryogenics, Vol 42, pp 427-432

Kuo, D T and Loc, A S (1997) Design of a 0.5 watt dual use long life low-cost pulse tube cooler, Advances in Cryogenic Engineering, Vol 43B, pp 2039-2046

Liang, J and Zhou, Y (2000) Study on miniature pulse tube cryocooler for space application, Cryogenics, Vol 40, pp 229-233

Lienerth, C, Thuimmes, G & Heiden, C (2000) Progress in Low Noise Cooling Performance of a Pulse-Tube Cooler for HT-SQUID Operation, Internal paper of ASC 2000, no 3EF04

Marquardt, E D and Radebaugh, R (2000) Pulse tube oxygen liquefier, Advanced Cryogenic Engineering, Vol 45, pp 457-464

Mills, A F (1995) Heat and Mass Transfer, Irwin, Chicago

Muralidhar, K and Suzuki, K (2001) Analysis of flow and heat transfer in a regenerator mesh using a non-Darcy thermally non-equilibrium model, International Journal of Heat and Mass Transfer, Vol 44, pp 2493-2504

Nasar, S (1998) Schaum's Outline series: Electric Machines and Electromechanics, McGraw-Hill, New York

Neveu, P and Babo, C (2000) A simplified model for pulse tube refrigeration, Cryogenics, Vol 40, pp 191-201

Organ, A J (1999) The miniature, reversed Stirling cycle cryocooler: integrated simulation of performance, Cryogenics, Vol 39, pp 253-266

Patankar, S V (1980) Numerical Heat Transfer and Fluid Flow, Hemisphere, Washington DC

Popescu, G, et al. (2001) A critical review of pulse tube cryogenerator research, International Journal of Refrigeration, Vol 24, pp 230-237

Raab, J and Abedzadeh, S (2001) TES FPC Flight Pulse Tube Cooler System, Cryocoolers, Vol 11, pp 131-138

Radebaugh, R (2000) Development of the Pulse Tube Refrigerator as an Efficient and Reliable Cryocooler, Proc. Institute of Refrigeration, Vol 96, pp 11-29

Radebaugh, R, Marquardt, J G & O'Gallagher, A (2000) Regenerator Behavior with Heat Input or Removal at Intermediate Temperatures, 11th International Cryocooler Conference

Radebaugh, R (2000) Pulse Tube Cryocoolers for Cooling Infrared Sensors, Proceedings of SPIE, The International Society for Optical Engineering, Infrared Technology and Applications XXVI, Vol 4130, pp 363-379

Redlich, R, Unger, R & van der Walt, N (1996) Linear Compressors: Motor Configuration, Modulation and Systems, 1996 International Compressor Engineering Conference, IN 47907-1077

Rijpma, A P, et al. (2000) Construction and tests of a heart scanner based on superconducting sensors cooled by small Stirling cryocoolers, Cryogenics, Vol 40, pp 821-828

Roach, P R and Kashani, A (1996) A simple modelling program for Orifice Pulse Tube Coolers, Internal Paper of NASA Ames Research Centre and Atlas Scientific, #50

Roach, P R and Kashani, A (1997) Pulse Tube Coolers with an inertance tube: Theory, modeling and practice, Advances in Cryogenic Engineering Conference

Roach, P R (2003) http://arcoptr.arc.nasa.gov./ARCOPTR-I-single.html

Scurlock, R G (1990) A matter of degrees: a brief history of cryogenics, Cryogenics, Vol 30, pp 483-500

Smith, W R (2001) One-dimensional models for heat and mass transfer in pulse-tube refrigerators, Cryogenics, Vol 41, pp 573-582

Steijaert, P P (1999) Thermodynamic aspects of pulse-tube refrigerators, PhD Thesis, Technische Universiteit Eindhoven, Eindhoven

Tanaeva, I (2004) Low-temperature Cryocooling, PhD Thesis, Technische Universiteit Eindhoven, Eindhoven

ter Brake H J M and Wiegerinck, G F M (2002) Low-power cryocooler survey, Cryogenics, Vol 42, pp 705 -718

Tward, E and Chan, C K (1999) Miniature space pulse tube cryocoolers, Cryogenics, Vol 39, pp 717-720

Uchiyama, U (2001) ALE finite element method for gas-liquid two-phase flow including moving boundary based on an incompressible two-fluid model, Nuclear Engineering and Design, Vol 205, pp 69-82

Wang, C and Thummes, G (1997) A two-stage pulse tube cooler operating below 4 K, Cryogenics, Vol 37 (3)

Weisend, J G (1998) Handbook of Cryogenic Engineering, Taylor and Francis, Philadelphia

Xu, M Y, de Waele ATAM & Ju, YL (1999) A pulse-tube refrigerator below 2K, Cryogenics, Vol 39, pp 865-869

Yaling, H, et al. (2001) Numerical simulation of convergent and divergent tapered pulse tube cryocoolers and experimental verification, Cryogenics, Vol 41, pp 699-704

Yuan S W K and Jung, H H (2000) Thermal management of computer systems using active cooling of pulse tube refrigerators, Internal paper of Cryocooler Group, BEI Technologies & Intel Corporation

Yuan, S W K and Kuo, D T (1998) Design and Preliminary Testing of BEI's CryoPulse 1000, the Commercial One-Watt Pulse Tube Cooler, 10th International Cryocooler Conference, pp 191-196

Zhu S W, et al (1997) Phase shift effect of long neck tube for the pulse tube refrigerator, Cryocoolers, Vol 9, Plenum Press, New York, pp 269-278

Zhu, S, et al. (1998) Work loss in double-inlet pulse tube refrigerators, Cryogenics, Vol 38, pp 803-807

Zhu, S and Matsubara, Y (2004) A numerical method of regenerator, Cryogenics, Vol 44, pp 131-140

Zhu, S and Matsubara, Y (2004) A numerical method of inertance tube pulse tube refrigerator, Cryogenics, Vol 44, pp 649-660

# APPENDIX A Derivation of Conservation Equations

## A.1 Continuity Equation

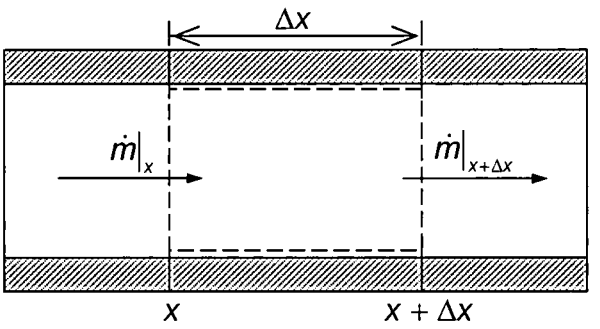


***Figure A.1*** *Continuity control volume*

The change of mass in an open control volume (figure A.1) is equal to the sum of the mass fluxes over its boundaries.

$$\frac{\Delta m}{\Delta t} = \dot{m}\big|_x - \dot{m}\big|_{x+\Delta x} \tag{A.1}$$

Substitute $m = \rho V_g$

$$\frac{\Delta(\rho V_g)}{\Delta t} = \dot{m}\big|_x - \dot{m}\big|_{x+\Delta x} \tag{A.2}$$

Substitute the mass flow rate $\dot{m} = \rho u A_f$ and the volume of the gas in the control volume $V_g = \Delta x A_f$

$$\frac{\Delta x A_f \Delta \rho}{\Delta t} = \rho u A_f\big|_x - \rho u A_f\big|_{x+\Delta x} \tag{A.3}$$

Divide by $A_f \Delta x$ and let $\Delta x \to 0$ and $\Delta t \to 0$

$$\frac{\partial(\rho u)}{\partial x} + \frac{\partial \rho}{\partial t} = 0 \tag{A.4}$$

## A.2 Momentum Equation

The change in momentum of an open control volume (figure A.2) is equal to the change in momentum flux of the control volume plus the sum of all the forces acting on the control volume.

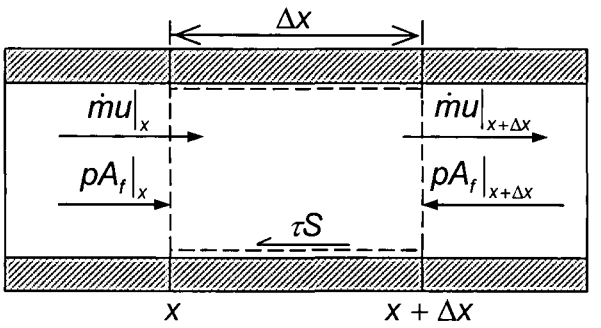


***Figure A.2*** *Momentum control volume*

Ignoring gravitation, friction and viscous forces, then for a horizontal tube:

$$\frac{\Delta mu}{\Delta t} = \dot{m}u\big|_x - \dot{m}u\big|_{x+\Delta x} + \sum F_x \tag{A.5}$$

Substitute the forces due to the pressure and friction

$$\frac{\Delta(V\rho u)}{\Delta t} = \dot{m}u\big|_x - \dot{m}u\big|_{x+\Delta x} + pA_f\big|_x - pA_f\big|_{x+\Delta x} - \tau S \tag{A.6}$$

Substitute the mass flow rate $\dot{m} = \rho u A_f$ and the volume of the gas $V = \Delta x A_f$

$$\frac{\Delta x A_f \Delta(\rho u)}{\Delta t} = A_f \rho uu\big|_x - A_f \rho uu\big|_{x+\Delta x} + pA_f\big|_x - pA_f\big|_{x+\Delta x} - \tau S \tag{A.7}$$

Divide by the volume $A_f \Delta x$ and let $\Delta x \to 0$ and $\Delta t \to 0$

$$\frac{\partial(\rho u)}{\partial t} = -\frac{\partial(\rho uu)}{\partial x} - \frac{\partial p}{\partial x} - \frac{\tau S}{V} \tag{A.8}$$

Substitute the shear stress $\tau = \dfrac{C_f \rho u|u|}{2}$

$$\frac{\partial(\rho u)}{\partial t}+\frac{\partial(\rho u u)}{\partial x}=-\frac{\partial p}{\partial x}-\frac{C_f \rho u|u| S}{2V} \tag{A.9}$$

## A.3 Conservation of Energy for Gas

Figure A.3 shows an open control volume of a gas flowing through a matrix contained in a tube. The heat exchange between the gas and the surface of the tube is denoted by $\dot{Q}_t$ and the gas and the matrix $\dot{Q}_m$. The axial heat conduction through the gas is denoted by $\dot{Q}_c$.

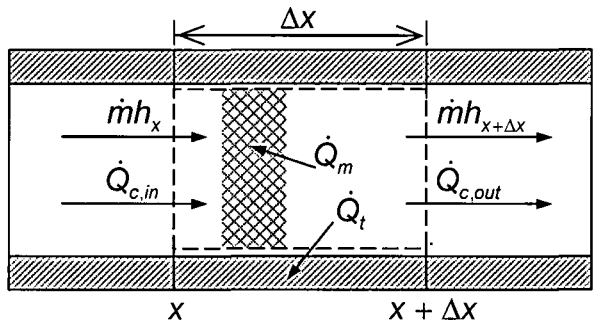


***Figure A.3*** *Energy conservation of an open control volume of the gas*

The net change of the total internal energy in the open control volume over a certain time period is the net result of all energy flows across the boundaries in that time period. Ignoring friction, potential and kinetic energy:

$$\frac{\Delta E}{\Delta t}=\sum \dot{E}_{in}-\sum \dot{E}_{out} \tag{A.10}$$

Substitute the internal energy $E=mi$ and ignoring friction potential and kinetic energy the energy flows over the boundary which is shown in figure A.3

$$\frac{\Delta(mi)}{\Delta t}=\dot{m}h\big|_x-\dot{m}h\big|_{x+\Delta x}+\dot{Q}_{c,in}-\dot{Q}_{c,out}-\dot{Q}_t-\dot{Q}_m \tag{A.11}$$

The internal and external surface areas and the cross sectional areas of the tube are shown in figure A.4.

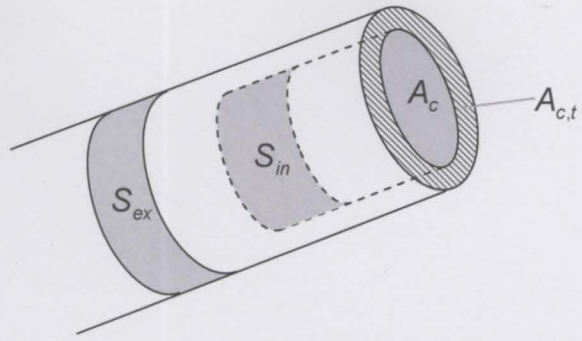


***Figure A.4*** *Nomenclature of surfaces cross sectional areas of tube.*

The heat exchange between the gas and the tube surface is

$$\dot{Q}_t = S_{in} h_{in} (T - T_t) \tag{A.12}$$

where $h_{in}$ is the heat transfer coefficient between the gas and the internal surface of the tube $S_{in} = \frac{\pi d_{in}^2}{4}$. The heat exchange between the gas and the matrix can be written, as

$$\dot{Q}_m = A_w h_m (T - T_m) \tag{A.13}$$

where $h_m$ is the heat transfer coefficient between the gas and the internal surface of the tube, $A_w$ the wetted area between the matrix and the gas. Substitute equations A.12, A.13 and the relations for the mass of the gas in the control volume $m = \rho A_f \Delta x$ (equation 3.41) and the mass flow rate $\dot{m} = \rho u A_f$ (equation 3.43)

$$\begin{aligned} \frac{\Delta x A_f \Delta(\rho i)}{\Delta t} = {} & \rho u A_f h\big|_x - \rho u A_f h\big|_{x+\Delta x} + \dot{Q}_{c,in} - \dot{Q}_{c,out} \\ & - S_{in} h_{in} (T - T_t) - A_w h_m (T - T_m) \end{aligned} \tag{A.14}$$

Divide by the volume of the gas $V = \Delta x A_f$ and let $\Delta x \to 0$ and $\Delta t \to 0$

$$\frac{\partial(\rho i)}{\partial t} = -\frac{\partial \rho u h}{\partial x} - \frac{1}{A_f}\frac{\partial \dot{Q}_c}{\partial x} - \frac{S_{in} h_{in}}{V}(T - T_t) - \frac{A_w h_m}{V}(T - T_m) \tag{A.15}$$

Substitute the relation for the internal energy $i = h - pv$ and Fourier's law of conduction $\frac{\dot{Q}_c}{A_f} = -k\frac{\partial T}{\partial x}$

$$\frac{\partial \rho(h-pv)}{\partial t} = -\frac{\partial \rho uh}{\partial x} + \frac{\partial}{\partial x}\left(k\frac{\partial T}{\partial x}\right) - \frac{S_{in}h_{in}}{V}(T-T_t) - \frac{A_w h_m}{V}(T-T_m) \quad \text{(A.16)}$$

Applying the identity for the density $\rho = \frac{1}{v}$

$$\frac{\partial \rho h}{\partial t} - \frac{\partial p}{\partial t} = -\frac{\partial \rho uh}{\partial x} + \frac{\partial}{\partial x}\left(k\frac{\partial T}{\partial x}\right) - \frac{S_{in}h_{in}}{V}(T-T_t) - \frac{A_w h_m}{V}(T-T_m) \quad \text{(A.17)}$$

Expand term on left hand side of equation A.17 and substitute the linear relation between enthalpy and temperature for helium $h = c_p T$ and the equation of state for an ideal gas $p = \rho RT$

$$\begin{aligned} &\rho c_p \frac{\partial T}{\partial t} + c_p T\frac{\partial \rho}{\partial t} - \frac{\partial \rho RT}{\partial t} \\ &= -c_p \frac{\partial \rho uT}{\partial x} + \frac{\partial}{\partial x}\left(k\frac{\partial T}{\partial x}\right) - \frac{S_{in}h_{in}}{V}(T-T_t) - \frac{A_w h_m}{V}(T-T_m) \end{aligned} \quad \text{(A.18)}$$

Expand further and rearrange

$$\begin{aligned} &(c_p - R)\rho\frac{\partial T}{\partial t} = -c_p\frac{\partial \rho uT}{\partial x} + \frac{\partial}{\partial x}\left(k\frac{\partial T}{\partial x}\right) \\ &-(c_p - R)T\frac{\partial \rho}{\partial t} - \frac{S_{in}h_{in}}{V}(T-T_t) - \frac{A_w h_m}{V}(T-T_m) \end{aligned} \quad \text{(A.19)}$$

## A.4 Conservation of Energy for the Gas Surroundings

The temperatures of the gas surroundings namely the tube wall and the matrix material of one control volume representing a regenerator or heat exchanger are assumed to be equal. Therefore the tube wall and matrix material is modelled as one lump mass subjected to heat conduction and heat transfer from the environment and the gas.

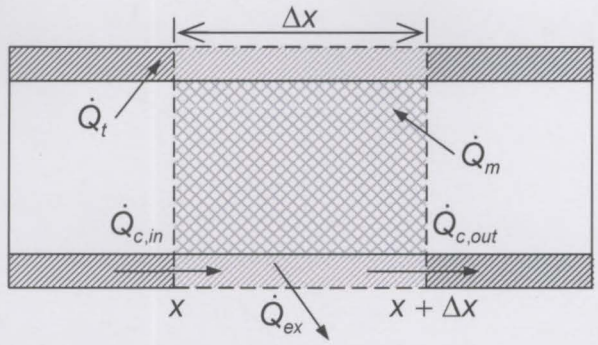


***Figure A.5*** *Energy conservation in an open control volume of the tube.*

The net change of the total internal energy in an open control volume over a certain time period is the net result of all energy flows across the boundaries in that time period. The total internal energy is the sum of the internal energies of the matrix material and the tube wall. The temperature of the tube wall and matrix is assumed to be constant in the radial direction, and hence conduction through the mesh is assumed to be zero in the axial direction.

$$\frac{\Delta E}{\Delta t} = \sum \dot{E}_{in} - \sum \dot{E}_{out} \tag{A.20}$$

The heat transferred from the tube-mesh control volume to the environment is given in equation A.21 where $S_{ex}$ is the external surface area of the tube (figure A.4) is and $h_{ex}$ is the external heat transfer coefficient between the external tube surface and the environment. The temperature of the gas surroundings is denoted by $T_{mt}$.

$$Q_{ex} = S_{ex} h_{ex} (T_{mt} - T_{ex}) \tag{A.21}$$

Substitute the internal energy $E = (m_m c_m + m_t c_t) T_{mt}$ and the energy flows over the boundary which is shown in figure A.5

$$\frac{\Delta (m_m c_m + m_t c_t) T_{mt}}{\Delta t} = \dot{Q}_{c,in} - \dot{Q}_{c,out} + \dot{Q}_t - \dot{Q}_{ex} + \dot{Q}_m \tag{A.22}$$

Substitute the mass of the tube $m_t = \rho_t V_t$ and the mass of the matrix material $m_m = \rho_m V_m$ in the control volume and equations A.12, A.13 and A.21

$$(\rho_m V_m c_m + \rho_t V_t c_t)\frac{\Delta T_{mt}}{\Delta t} = \dot{Q}_{c,in} - \dot{Q}_{c,out} + S_{in} h_{in}(T - T_{mt}) - S_{ex} h_{ex}(T_{mt} - T_{ex}) + A_w h_m (T - T_{mt}) \quad \text{(A.23)}$$

Divide by the control volume length $\Delta x$

$$((1-e_v)\rho_m A_c c_m + \rho_t A_{c,t} c_t)\frac{\Delta T_{mt}}{\Delta t} = \frac{(\dot{Q}_{c,in} - \dot{Q}_{c,out})}{\Delta x} + \pi d_{in} h_{in}(T - T_{mt}) - \pi d_{ex} h_{ex}(T_{mt} - T_{ex}) + \frac{4A_c(1-e_v)}{d_w} h_m (T - T_{mt})$$

(A.24)

Let $\Delta x \to 0$ and $\Delta t \to 0$

$$((1-e_v)\rho_m A_c c_m + \rho_t A_{c,t} c_t)\frac{\partial T_{mt}}{\partial t} = -\frac{\partial \dot{Q}_c}{\partial x} + \pi d_{in} h_{in}(T - T_{mt}) - \pi d_{ex} h_{ex}(T_{mt} - T_{ex}) + \frac{4A_c(1-e_v)}{d_w} h_m (T - T_{mt}) \quad \text{(A.25)}$$

Neglecting the conduction of heat in the mesh in the axial direction and substituting Fourier's law on conduction $\dot{Q}_c = -k_t A_{c,t} \frac{\partial T_{mt}}{\partial x}$

$$((1-e_v)\rho_m A_c c_m + \rho_t A_{c,t} c_t)\frac{\partial T_{mt}}{\partial t} = k_t A_{c,t} \frac{\partial}{\partial x}\left(\frac{\partial T_{mt}}{\partial x}\right) + \pi d_{in} h_{in}(T - T_{mt}) - \pi d_{ex} h_{ex}(T_{mt} - T_{ex}) + \frac{4A_c(1-e_v)}{d_w} h_m (T - T_{mt})$$

(A.26)

If there is no mesh in the tube then the conduction is zero and the heat transfer between the matrix and gas cancel out and equation A.25 reduces to

$$\rho_t A_{c,t} c_t \frac{\partial T_t}{\partial t} = k_t A_{c,t} \frac{\partial}{\partial x}\left(\frac{\partial T_t}{\partial x}\right) + \pi d_{in} h_{in}(T - T_t) - \pi d_{ex} h_{ex}(T_t - T_{ex}) \quad \text{(A.27)}$$

# APPENDIX B Discretization of Conservation Equations

The differential equations derived Appendix A for one dimensional compressible flow will be discretized in this section with the Gauss theorem and these equations will then be derived using the SIMPLE method introduced by (Patankar, 1980).

## B.1 Geometric Aspects

A staggered grid (figure B.1) is used to prevent pressure decoupling (Patankar, 1980). The velocities are saved on the *j* interfaces (velocity interfaces) and the pressure, density and temperature are saved on the *i* interfaces (pressure interfaces).

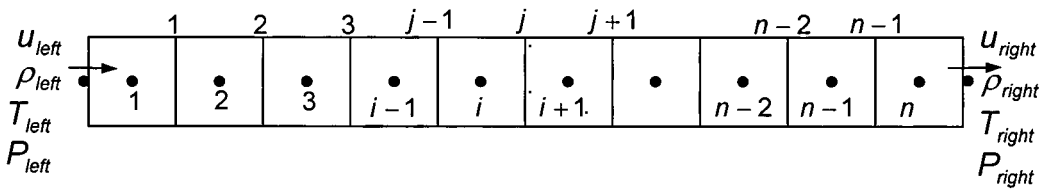


***Figure B.1*** *One dimensional staggered grid*

The volume of a conical control volume is

$$V = \frac{\pi}{12}\left[(D_x)^2 + D_x D_{x+\Delta x} + (D_{x+\Delta x})^2\right]\Delta x \tag{B.1}$$

### B.1.1 Linear Interpolation for a Non-uniform Grid

A linear interpolation function has to be used when a scalar property for instance pressure is needed on a velocity node *j* for a non-uniform grid. Take note that it is not necessary to interpolate with a function for a property on the scalar nodes from the velocity nodes because the pressure nodes are always situated in the middle of the cell and therefore central differencing can be used.

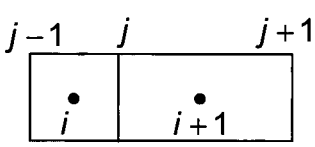


***Figure B.2*** *One dimensional non-uniform grid*

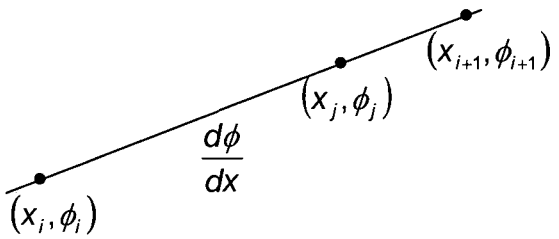


***Figure B.3*** *Linear interpolation for non-uniform grid*

*For positive flow:*

$$\frac{\phi_{i+1} - \phi_i}{x_{i+1} - x_i} = \frac{\phi_j - \phi_i}{x_j - x_i} \tag{B.2}$$

Rearranging and setting $\sigma_j = \dfrac{x_j - x_i}{x_{i+1} - x_i}$

$$\phi_j = \phi_i + \sigma_j(\phi_{i+1} - \phi_i) \tag{B.3}$$

*For negative flow:*

$$\frac{\phi_{i+1} - \phi_i}{x_{i+1} - x_i} = \frac{\phi_{i+1} - \phi_j}{x_{i+1} - x_j} \tag{B.4}$$

Rearranging and setting $\varepsilon_j = \dfrac{x_j - x_{i+1}}{x_{i+1} - x_i}$

$$\phi_j = \phi_{i+1} + \varepsilon_j(\phi_{i+1} - \phi_i) \tag{B.5}$$

### B.1.2 Flux Blending Factor

A flux blending factor $\lambda_\rho$ is introduced which "blends" the density used on a velocity interface between central differencing and up-streaming. When $\lambda_\rho = 0$ then up-streaming is used and when $\lambda_\rho = 1$ then central differencing is used. The linear interpolation for the density in positive flow can now be written as

$$\rho_j = \rho_i + \lambda_\rho \sigma_j(\rho_{i+1} - \rho_i) \tag{B.6}$$

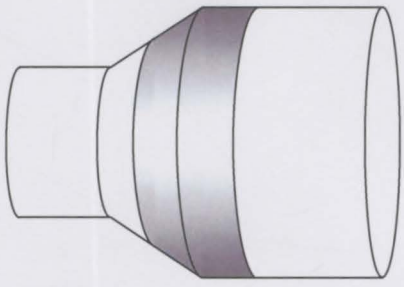

***Figure B.4*** *Area change in tube*

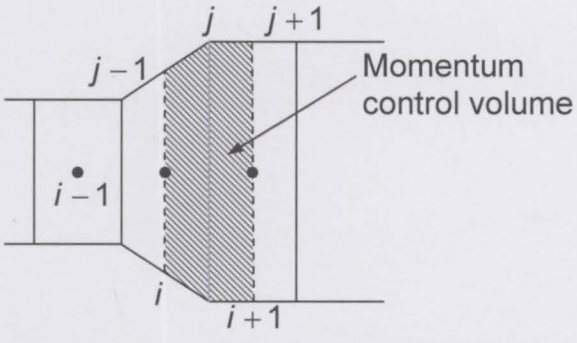


***Figure B.5*** *Grid for momentum control volume at an area change*

The surface area is equal to the sum of the surface area of a conical frustum and the surface area of a cylinder. The surface area of a conical control volume is given below

$$S_{con} = \frac{\pi}{4}(D_x + D_{x+\Delta x})\sqrt{(D_x - D_{x+\Delta x})^2 + 4\Delta x_{con}^2} \tag{B.7}$$

## B.2 Momentum Equation

The momentum equation as derived in Appendix A (equation A.9) is repeated as equation B.8.

$$\frac{\partial(\rho u)}{\partial t} + \frac{\partial(\rho u u)}{\partial x} = -\frac{\partial p}{\partial x} - \frac{C_f \rho u|u|S}{V} \tag{B.8}$$

Integrate over the volume at point *j*

$$\int_V \frac{\partial(\rho u)}{\partial t} dV + \int_V \frac{\partial(\rho u u)}{\partial x} dV = -\int_V \frac{\partial p}{\partial x} dV - \int_V \frac{C_f \rho u |u| S}{2V} dV \tag{B.9}$$

An implicit scheme is used and therefore all the variables in the discretized momentum equation are updated in the beginning of a new iteration within a time step except the $(\rho u)^{old}$ term which is kept constant. Applying the Gauss theorem (Finney and Thomas, 1990)

$$\left[\frac{\left(\rho u - \rho^{old} u^{old}\right)}{\Delta t} V\right]_j + \int_A (\rho u u) \cdot \bar{n} dA\Big|_j = -\frac{(p_{i+1} - p_i)}{(x_{i+1} - x_i)} V_j - \frac{\rho_j C_j^f u_j |u_j| S_j}{2} \tag{B.10}$$

Rearranging the first two terms of equation B.10

$$\begin{aligned} &\frac{\rho_j u_j}{\Delta t} V_j + (\rho u u A)_{i+1} - (\rho u u A)_i \\ &= \frac{\rho_j^{old} u_j^{old}}{\Delta t} V_j - \frac{(p_{i+1} - p_i)}{(x_{i+1} - x_i)} V_j - \frac{\rho_j C_j^f u_j |u_j| S_j}{2} \end{aligned} \tag{B.11}$$

### B.2.1 Positive Flow

The discretized momentum equation (equation B.11) will now be derived further for positive flow from left to right. Taking central differences for the velocity and introducing a flux blending factor $\lambda_u$ which mixes the upwind and central difference for one of the velocities. If $\lambda_u = 0$ then it is upwind and if $\lambda_u = 1$ then it is central differencing (Patankar, 1980).

$$\begin{aligned} &\frac{\rho_j V_j u_j}{\Delta t} + (\rho A)_{i+1} \frac{(u_j + u_{j+1})}{2} \left(u_j + \frac{\lambda_u}{2}(u_{j+1} - u_j)\right) \\ &- (\rho A)_i \frac{(u_{j-1} + u_j)}{2} \left(u_{j-1} + \frac{\lambda_u}{2}(u_j - u_{j-1})\right) \\ &= \frac{\rho_j^{old} V_j u_j^{old}}{\Delta t} - \frac{(p_{i+1} - p_i)}{(x_{i+1} - x_i)} V_j - \frac{\rho_j C_j^f u_j |u_j| S_j}{2} \end{aligned} \tag{B.12}$$

Rearranging

$$\left[-(\rho A)_i \frac{(u_{j-1}+u_j)}{2}\right]u_{j-1}+\left[\frac{\rho_j V_j}{\Delta t}+(\rho A)_{i+1}\frac{(u_j+u_{j+1})}{2}\right]u_j$$
$$=-\frac{\lambda_u}{4}(u_{j+1}^2-u_j^2)(\rho A)_{i+1}+\frac{\lambda_u}{4}(u_j^2-u_{j-1}^2)(\rho A)_i$$
$$\frac{\rho_j^{old}V_j u_j^{old}}{\Delta t}-\frac{(p_{i+1}-p_i)}{(x_{i+1}-x_i)}V_j-\frac{\rho_j C_j^f u_j|u_j|S_j}{2} \qquad \text{(B.13)}$$

*Momentum relaxation*

The momentum equation is now written in terms of its coefficients and in the form of

$$a_j u_{j-1}+B_j u_j+c_j u_{j+1}=D_j \qquad \text{(B.14)}$$

Moving the middle term on the LHS to the RHS and adding the term $\frac{B_j}{\alpha_m}u_j$ on both sides

$$a_j u_{j-1}+\frac{B_j}{\alpha_m}u_j+c_j u_{j+1}=D_j-B_j u_j+\frac{B_j}{\alpha_m}u_j \qquad \text{(B.15)}$$

Substitute $b_j=\frac{B_j}{\alpha_m}$

$$a_j u_{j-1}+b_j u_j+c_j u_{j+1}=D_j+(1-\alpha_m)b_j u_j \qquad \text{(B.16)}$$

Substitute $d_j=D_j+(1-\alpha_m)b_j u_j$

$$a_j u_{j-1}+b_j u_j+c_j u_{j+1}=d_j \qquad \text{(B.17)}$$

This equation can be solved implicitly with the Thomas algorithm with the coefficients *a b c* and *d* as follows

$$a_j = -(\rho A)_i \frac{(u_{j-1} + u_j)}{2}$$

$$b_j = \frac{1}{\alpha_m}\left[(\rho A)_{i+1} \frac{(u_j + u_{j+1})}{2} + \frac{\rho_j V_j}{\Delta t}\right]$$

$$c_j = 0$$

$$d_j = -\frac{\lambda_u}{4}(u_{j+1}^2 - u_j^2)(\rho A)_{i+1} + \frac{\lambda_u}{4}(u_j^2 - u_{j-1}^2)(\rho A)_i + (1-\alpha_m) b_j u_j + \frac{\rho_j^{old} V_j u_j^{old}}{\Delta t} - \frac{(p_{i+1} - p_i)}{(x_{i+1} - x_i)} V_j - \frac{\rho_j C_j^f u_j |u_j| S_j}{2} \quad \text{(B.18)}$$

*Left hand boundary conditions*

Substitute the left hand boundary conditions

$$b_1 = \frac{1}{\alpha_m}\left[(\rho A)_2 \frac{(u_1 + u_2)}{2} + \frac{\rho_1^j V_1^j}{\Delta t}\right]$$

$$c_1 = 0$$

$$d_1 = -\frac{\lambda_u}{4}(u_2^2 - u_1^2)(\rho A)_2 + \frac{\lambda_u}{4}(u_1^2 - u_{left}^2)(\rho A)_1 + \frac{\rho_1^{j,old} V_1^j u_1^{old}}{\Delta t} + (1-\alpha_m) b_1 u_1 - \frac{(p_2 - p_1)}{(x_2 - x_1)} V_1^j - \frac{\rho_1^j C_1^f u_1 |u_1| S_1}{2} + (\rho A)_1 \frac{(u_{left} + u_1)}{2} u_{left} \quad \text{(B.19)}$$

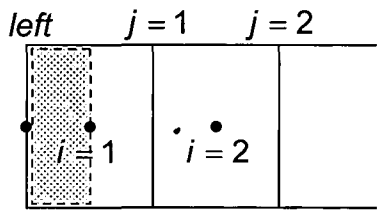


***Figure B.6*** *Momentum control volume at left hand boundary*

Rewrite equation B.13 at the left hand boundary to calculate the velocity on the left hand boundary $u_{left}$

$$-(\rho A)_{left} \frac{(u_{left-1} + u_{left})}{2} u_{left-1} + \left[(\rho A)_1 \frac{(u_{left} + u_1)}{2} + \frac{\rho_{left} V_{left}}{\Delta t}\right] u_{left}$$
$$= -\frac{\lambda_u}{4}(u_1^2 - u_{left}^2)(\rho A)_1 + \frac{\lambda_u}{4}(u_{left}^2 - u_{left-1}^2)(\rho A)_1 \quad \text{(B.20)}$$
$$+ \frac{\rho_{left}^{old} V_{left} u_{left}^{old}}{\Delta t} - \frac{(p_1 - p_{left})}{(x_1 - x_{left})} V_{left} - \frac{\rho_{left} C_{left}^f u_{left} |u_{left}| S_{left}}{2}$$

Substitute $u_{left-1} = u_{left}$

$$\left[-(\rho A)_{left}u_{left} + (\rho A)_1\frac{(u_{left}+u_1)}{2} + \frac{\rho_{left}V_{left}}{\Delta t}\right]u_{left}$$
$$= -\frac{\lambda_u}{4}\left(u_1^2 - u_{left}^2\right)(\rho A)_1 + \frac{\rho_{left}^{old}V_{left}u_{left}^{old}}{\Delta t} - \frac{(p_1 - p_{left})}{(x_1 - x_{left})}V_{left} - \frac{\rho_{left}C_{left}^f u_{left}|u_{left}|S_{left}}{2} \quad \text{(B.21)}$$

Now $u_{left}$ can be calculated explicitly

$$u_{left} = \frac{d_{left}}{b_{left}} \quad \text{(B.22)}$$

And the coefficients are

$$b_{left} = -(\rho A)_{left}u_{left} + (\rho A)_1\frac{(u_{left}+u_1)}{2} + \frac{\rho_{left}V_{left}}{\Delta t} \quad \text{(B.23)}$$

$$d_{left} = -\frac{\lambda_u}{4}\left(u_1^2 - u_{left}^2\right)(\rho A)_1 + \frac{\rho_{left}^{old}V_{left}u_{left}^{old}}{\Delta t} - \frac{(p_1 - p_{left})}{(x_1 - x_{left})}V_{left} - \frac{\rho_{left}C_{left}^f u_{left}|u_{left}|S_{left}}{2} \quad \text{(B.24)}$$

*Right hand boundary conditions*

$$a_{n-1} = -(\rho A)_{n-1}\frac{(u_{n-2}+u_{n-1})}{2}$$
$$b_{n-1} = \frac{1}{\alpha_m}\left[(\rho A)_n\frac{(u_{n-1}+u_{right})}{2} + \frac{\rho_{n-1}^j V_{n-1}^j}{\Delta t}V_{n-1}^j\right]$$
$$d_{n-1} = -\frac{\lambda_u}{4}\left(u_{right}^2 - u_{n-1}^2\right)(\rho A)_n + \frac{\lambda_u}{4}\left(u_{n-1}^2 - u_{n-2}^2\right)(\rho A)_{n-1} + \frac{\rho_{n-1}^{j,old}V_{n-1}^j u_{n-1}^{old}}{\Delta t} \quad \text{(B.25)}$$
$$+ (1-\alpha_m)b_{n-1}u_{n-1}$$
$$- \frac{(p_n - p_{n-1})}{(x_n - x_{n-1})}V_{n-1}^j - \frac{\rho_{n-1}^j C_{n-1}^f u_{n-1}|u_{n-1}|S_{n-1}}{2}$$

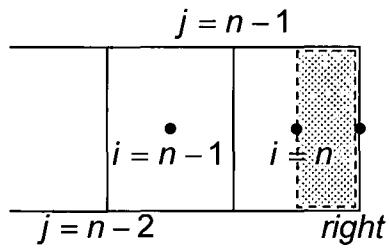


***Figure B.7*** *Momentum control volume at right hand boundary*

Rewrite equation B.13 at the right hand boundary to calculate the velocity at the right hand boundary $u_{right}$

$$
\begin{aligned}
&-(\rho A)_n \frac{(u_{n-1}+u_{right})}{2} u_{n-1} \\
&+\left[(\rho A)_{right} \frac{(u_{right}+u_{right+1})}{2} + \frac{\rho_{right} V_{right}}{\Delta t}\right] u_{right} \\
&= -\frac{\lambda_u}{4}\left(u^2_{right+1} - u^2_{right}\right)(\rho A)_{right} + \frac{\lambda_u}{4}\left(u^2_{right} - u^2_{n-1}\right)(\rho A)_n \\
&\quad + \frac{\rho^{old}_{right} V_{right} u^{old}_{right}}{\Delta t} - \frac{(p_{right} - p_n)}{(x_{right} - x_n)} V_{right} - \frac{\rho_{right} C^f_{right} u_{right} |u_{right}| S_{right}}{2}
\end{aligned}
\tag{B.26}
$$

Substitute $u_{right+1} = u_{right}$

$$
\begin{aligned}
&-(\rho A)_n \frac{(u_{n-1}+u_{right})}{2} u_{n-1} \\
&+\left[(\rho A)_{right} u_{right} + \frac{\rho_{right} V_{right}}{\Delta t}\right] u_{right} \\
&= \frac{\lambda_u}{4}\left(u^2_{right} - u^2_{n-1}\right)(\rho A)_n + \frac{\rho^{old}_{right} V_{right} u^{old}_{right}}{\Delta t} - \frac{(p_{right} - p_n)}{(x_{right} - x_n)} V_{right} - \frac{\rho_{right} C^f_{right} u_{right} |u_{right}| S_{right}}{2}
\end{aligned}
\tag{B.27}
$$

Now $u_{right}$ can be calculated explicitly

$$
u_{right} = \frac{d_{right} - a_{right} u_{n-1}}{b_{right}} \tag{B.28}
$$

and the coefficients are

$$
\begin{aligned}
a_{right} &= -(\rho A)_n \frac{(u_{n-1} + u_{right})}{2} \\
b_{right} &= (\rho A)_{right} u_{right} + \frac{\rho_{right} V_{right}}{\Delta t} \\
d_{right} &= \frac{\lambda_u}{4}\left(u_{right}^2 - u_{n-1}^2\right)(\rho A)_n + \frac{\rho_{right}^{old} V_{right} u_{right}^{old}}{\Delta t} - \frac{(p_{right} - p_n)}{(x_{right} - x_n)} V_{right} \\
&\quad - \frac{\rho_{right} C_{right}^f u_{right} |u_{right}| S_{right}}{2}
\end{aligned}
\tag{B.29}
$$

### B.2.2 Negative Flow

The discretized momentum equation (equation B.11) will now be derived further for negative flow from right to left. Repeating equation B.11

$$
\begin{aligned}
&\frac{\rho_j V_j u_j}{\Delta t} + (\rho u u A)_{i+1} - (\rho u u A)_i \\
&= \frac{\rho_j^{old} V_j u_j^{old}}{\Delta t} - \frac{(p_{i+1} - p_i)}{(x_{i+1} - x_i)} V_j - \frac{\rho_j C_j^f u_j |u_j| S_j}{2}
\end{aligned}
\tag{B.30}
$$

Taking central differencing for the velocity

$$
\begin{aligned}
&\frac{\rho_j V_j u_j}{\Delta t} + (\rho A)_{i+1} \frac{(u_j + u_{j+1})}{2}\left(u_{j+1} + \frac{\lambda_u}{2}(u_j - u_{j+1})\right) \\
&- (\rho A)_i \frac{(u_{j-1} + u_j)}{2}\left(u_j + \frac{\lambda_u}{2}(u_{j-1} - u_j)\right) \\
&= \frac{\rho_j^{old} V_j u_j^{old}}{\Delta t} - \frac{(p_{i+1} - p_i)}{(x_{i+1} - x_i)} V_j - \frac{\rho_j C_j^f u_j |u_j| S_j}{2}
\end{aligned}
\tag{B.31}
$$

Rearrange

$$\left[\frac{\rho_j V_j}{\Delta t} - (\rho A)_i \frac{(u_{j-1} + u_j)}{2}\right] u_j + \left[(\rho A)_{i+1} \frac{(u_j + u_{j+1})}{2}\right] u_{j+1}$$
$$= \frac{\lambda_u}{4}\left(u_{j+1}^2 - u_j^2\right)(\rho A)_{i+1} - \frac{\lambda_u}{4}\left(u_j^2 - u_{j-1}^2\right)(\rho A)_i + \frac{\rho_j^{old} V_j u_j^{old}}{\Delta t}$$
$$- \frac{(p_{i+1} - p_i)}{(x_{i+1} - x_i)} V_j - \frac{\rho_j C_j^f u_j |u_j| S_j}{2} \qquad \text{(B.32)}$$

Applying source term linearization, the coefficients *a b c* and *d* are as follows

$$a_j = 0$$
$$b_j = \frac{1}{\alpha_m}\left[\frac{\rho_j V_j}{\Delta t} - (\rho A)_i \frac{(u_{j-1} + u_j)}{2}\right]$$
$$c_j = (\rho A)_{i+1} \frac{(u_j + u_{j+1})}{2} \qquad \text{(B.33)}$$
$$d_j = \frac{\lambda_u}{4}\left(u_{j+1}^2 - u_j^2\right)(\rho A)_{i+1} - \frac{\lambda_u}{4}\left(u_j^2 - u_{j-1}^2\right)(\rho A)_i + \frac{\rho_j^{old} V_j u_j^{old}}{\Delta t}$$
$$+ (1 - \alpha_m) b_j u_j - \frac{(p_{i+1} - p_i)}{(x_{i+1} - x_i)} V_j - \frac{\rho_j C_j^f u_j |u_j| S_j}{2}$$

*Left hand boundary conditions*

$$b_1 = \frac{1}{\alpha_m}\left[\frac{\rho_1^j V_1^j}{\Delta t} - (\rho A)_1 \frac{(u_{left} + u_1)}{2}\right]$$
$$c_1 = (\rho A)_2 \frac{(u_1 + u_2)}{2} \qquad \text{(B.34)}$$
$$d_1 = \frac{\lambda_u}{4}\left(u_2^2 - u_1^2\right)(\rho A)_2 - \frac{\lambda_u}{4}\left(u_1^2 - u_{left}^2\right)(\rho A)_1 c + \frac{\rho_1^{j,old} V_1^j u_1^{old}}{\Delta t}$$
$$+ (1 - \alpha_m) b_1 u_1 - \frac{(p_2 - p_1)}{(x_2 - x_1)} V_1^j - \frac{\rho_1^j C_1^f u_1 |u_1| S_1}{2}$$

Discretize the momentum equation (from equation B.32) for $u_{left}$ at the left hand boundary

$$\left[\frac{\rho_{left}V_{left}}{\Delta t}-(\rho A)_{left}\frac{(u_{left-1}+u_{left})}{2}\right]u_{left}+(\rho A)_1\frac{(u_{left}+u_1)}{2}u_1$$
$$=\frac{\lambda_u}{4}(u_1^2-u_{left}^2)(\rho A)_1-\frac{\lambda_u}{4}(u_{left}^2-u_{left-1}^2)(\rho A)_{left} \qquad \text{(B.35)}$$
$$+\frac{\rho_{left}^{old}V_{left}u_{left}^{old}}{\Delta t}-\frac{(p_1-p_{left})}{(x_1-x_{left})}V_{left}-\frac{\rho_{left}C_{left}^f u_{left}|u_{left}|S_{left}}{2}$$

Substitute $u_{left-1}=u_{left}$

$$\left[\frac{\rho_{left}V_{left}}{\Delta t}-\rho_{left}A_{left}u_{left}\right]u_{left}+(\rho A)_1\frac{(u_{left}+u_1)}{2}u_1$$
$$=\frac{\lambda_u}{4}(u_1^2-u_{left}^2)(\rho A)_1+\frac{\rho_{left}^{old}V_{left}u_{left}^{old}}{\Delta t}-\frac{(p_1-p_{left})}{(x_1-x_{left})}V_{left}-\frac{\rho_{left}C_{left}^f u_{left}|u_{left}|S_{left}}{2} \qquad \text{(B.36)}$$

Now $u_{left}$ can be calculated explicitly

$$u_{left}=\frac{d_{left}-c_{left}u_1}{b_{left}} \qquad \text{(B.37)}$$

and the coefficients are

$$b_{left}=\frac{\rho_{left}V_{left}}{\Delta t}-\rho_{left}A_{left}u_{left}$$
$$c_{left}=(\rho A)_1\frac{(u_{left}+u_1)}{2}$$
$$d_{left}=\frac{\lambda_u}{4}(u_1^2-u_{left}^2)(\rho A)_1+\frac{\rho_{left}^{old}V_{left}u_{left}^{old}}{\Delta t}-\frac{(p_1-p_{left})}{(x_1-x_{left})}V_{left}-\frac{\rho_{left}C_{left}^f u_{left}|u_{left}|S_{left}}{2}$$

(B.38)

*Right hand boundary conditions*

$$a_{n-1} = 0$$

$$b_{n-1} = \frac{1}{\alpha_m}\left[\frac{\rho_{n-1}^{j} V_{n-1}^{j}}{\Delta t} - (\rho A)_{n-1}\frac{(u_{n-2}+u_{n-1})}{2}\right]$$

$$d_{n-1} = \frac{\lambda_u}{4}\left(u_{right}^2 - u_{n-1}^2\right)(\rho A)_n - \frac{\lambda_u}{4}\left(u_{n-1}^2 - u_{n-2}^2\right)(\rho A)_{n-1} + \frac{\rho_{n-1}^{j,old} V_{n-1}^{j} u_{n-1}^{old}}{\Delta t} \qquad \text{(B.39)}$$
$$- \frac{(p_n - p_{n-1})}{(x_n - x_{n-1})} V_{n-1}^{j} - \frac{\rho_{n-1}^{j} C_{n-1}^{f} u_{n-1} |u_{n-1}| S_{n-1}}{2}$$
$$+ (1-\alpha_m) b_{n-1} u_{n-1} - (\rho A)_n \frac{(u_{n-1}+u_{right})}{2} u_{right}$$

Discretize the momentum equation for $u_{right}$ at the right hand boundary

$$\left[\frac{\rho_{right} V_{right}}{\Delta t} - (\rho A)_n \frac{(u_{n-1}+u_{right})}{2}\right] u_{right} + (\rho A)_{right} \frac{(u_{right}+u_{right+1})}{2} u_{right+1}$$
$$= \frac{\lambda_u}{4}\left(u_{right+1}^2 - u_{right}^2\right)(\rho A)_{right} - \frac{\lambda_u}{4}\left(u_{right}^2 - u_{n-1}^2\right)(\rho A)_n + \frac{\rho_{right}^{old} V_{right} u_{right}^{old}}{\Delta t} \qquad \text{(B.40)}$$
$$- \frac{(p_{right} - p_n)}{(x_{right} - x_n)} V_{right} - \frac{\rho_{right} C_{right}^{f} u_{right} |u_{right}| S_{right}}{2}$$

Substitute $u_{right+1} = u_{right}$

$$\left[\frac{\rho_{right} V_{right}}{\Delta t} - (\rho A)_n \frac{(u_{n-1}+u_{right})}{2} + (\rho A)_{right} u_{right}\right] u_{right}$$
$$= -\frac{\lambda_u}{4}\left(u_{right}^2 - u_{n-1}^2\right)(\rho A)_n + \frac{\rho_{right}^{old} V_{right} u_{right}^{old}}{\Delta t} \qquad \text{(B.41)}$$
$$- \frac{(p_{right} - p_n)}{(x_{right} - x_n)} V_{right} - \frac{\rho_{right} C_{right}^{f} u_{right} |u_{right}| S_{right}}{2}$$

Now $u_{right}$ can be calculated explicitly

$$u_{right} = \frac{d_{right}}{b_{right}} \qquad \text{(B.42)}$$

and the coefficients are

$$b_{right} = \frac{\rho_{right} V_{right}}{\Delta t} - (\rho A)_n \frac{(u_{n-1} + u_{right})}{2} + (\rho A)_{right} u_{right}$$

$$d_{right} = -\frac{\lambda_u}{4}\left(u_{right}^2 - u_{n-1}^2\right)(\rho A)_n + \frac{\rho_{right}^{old} V_{right} u_{right}^{old}}{\Delta t} \qquad \text{(B.43)}$$

$$-\frac{(p_{right} - p_n)}{(x_{right} - x_n)} V_{right} - \frac{\rho_{right} C_{right}^f u_{right} |u_{right}| S_{right}}{2}$$

## B.3 Pressure Correction Equation

The velocity field that can be calculated from the previous equation satisfies the momentum equation, but not the continuity equation. This is because the pressure field was wrong. The pressure correction equation calculates a correction $p'$ to the pressure $p^*$ so that the continuity equation can be satisfied. (Patankar, 1980)

$$p = p^* + p' \qquad \text{(B.44)}$$

The momentum equation in the form which does satisfy the continuity equation

$$u_j = \frac{d_j}{b_j} - \frac{a_j u_{j-1}}{b_j} - \frac{c_j u_{j+1}}{b_j} \qquad \text{(B.45)}$$

In the beginning of each iteration the pressure correction is zero and $p = p^*$ and equation B.45 can be written as

$$u_j^* = \frac{d_j^*}{b_j} - \frac{a_j u_{j-1}^*}{b_j} - \frac{c_j u_{j+1}^*}{b_j} \qquad \text{(B.46)}$$

where its velocity field $u^*$ does not satisfy continuity. Subtracting equation B.45 from B.46 we can get the momentum equation expressed in terms of the velocity and pressure corrections $u' p'$.

$$u_j' = \frac{d_j'}{b_j} - \frac{a_j u_{j-1}'}{b_j} - \frac{c_j u_{j+1}'}{b_j} \qquad \text{(B.47)}$$

The equation for the pressure correction can now be derived insisting that the velocity field must satisfy the continuity equation.

The second and third term on the right hand side of equation B.47 is set to zero, because we only need correction terms that contains a pressure gradient. This is legitimate since we are only interested in the converged solution where all the corrections are zero. The pressure correction method is iterative and only guidance is needed on which direction the pressure should be nudged so that the continuity equation would be satisfied eventually (Patankar, 1990). The velocity correction can now be written as:

$$u_j' = \frac{d_j'}{b_j} \tag{B.48}$$

The coefficients $d_j$ and $b_j$ are

$$b_j = \frac{1}{\alpha_m}\left[(\rho A)_{i+1}\frac{(u_j + u_{j+1})}{2} + \frac{\rho_j V_j}{\Delta t}\right] \text{ if } u_j \geq 0$$
$$b_j = \frac{1}{\alpha_m}\left[\frac{\rho_i V_j}{\Delta t} - (\rho A)_i \frac{(u_{j-1} + u_j)}{2}\right] \text{ if } u_j < 0 \tag{B.49}$$
$$d_j' = -\frac{(p_{i+1}' - p_i')}{(x_{i+1} - x_i)} V_j$$

All the other terms of the $d_j'$ coefficient is left out because we are only interested din the pressure.

From the subtraction of equation B.45 from B.46 we know that

$$u_j' = u_j - u_j^* \tag{B.50}$$

Substituting B.48 into B.50

$$u_j = u_j^* + \frac{d_j'}{b_j} \tag{B.51}$$

Returning to the continuity equation which is derived in Appendix A (equation A.4)

$$\frac{\partial(\rho u)}{\partial x} = -\frac{\partial \rho}{\partial t} \tag{B.52}$$

Integrate over the volume at point *i*

$$\int_V \frac{\partial(\rho u)}{\partial x} dV = -\int_V \frac{\partial \rho}{\partial t} dV \tag{B.53}$$

Applying the Gauss theorem (Finney and Thomas, 1990)

$$\int_A (\rho u) \cdot \bar{n} dA\Big|_i = -\frac{\left(\rho_i - \rho_i^{old}\right)}{\Delta t} V_i \tag{B.54}$$

$$(\rho u A)_j - (\rho u A)_{j-1} = -\frac{\left(\rho_i - \rho_i^{old}\right)}{\Delta t} V_i \tag{B.55}$$

Substituting equation B.51 into equation B.55

$$\left(u_j^* + \frac{d_j'}{b_j}\right)(\rho A)_j - \left(u_{j-1}^* + \frac{d_{j-1}'}{b_{j-1}}\right)(\rho A)_{j-1} = -\frac{\left(\rho_i - \rho_i^{old}\right)}{\Delta t} V_i \tag{B.56}$$

The density can also be written in terms of a correction $\rho = \rho' + \rho^*$

$$\left(u_j^* + \frac{d_j'}{b_j}\right) A_j \left(\rho_j' + \rho_j^*\right) - \left(u_{j-1}^* + \frac{d_{j-1}'}{b_{j-1}}\right) A_{j-1} \left(\rho_{j-1}' + \rho_{j-1}^*\right) = -\frac{\left(\rho_i - \rho_i^{old}\right)}{\Delta t} V_i \tag{B.57}$$

Substituting $d_j'$ and $d_{j-1}'$

$$\begin{aligned} &\rho_j' A_j u_j^* - \frac{\left(p_{i+1}' - p_i'\right)}{(x_{i+1} - x_i) b_j} \rho_j^* V_j A_j + \frac{\left(p_i' - p_{i-1}'\right)}{(x_i - x_{i-1}) b_{j-1}} \rho_{j-1}^* V_{j-1} A_{j-1} \\ &- \rho_{j-1}' A_{j-1} u_{j-1}^* + \frac{\left(p_i' - p_{i-1}'\right)}{(x_i - x_{i-1}) b_{j-1}} \rho_{j-1}' V_{j-1} A_{j-1} - \frac{\left(p_{i+1}' - p_i'\right)}{(x_{i+1} - x_i) b_j} \rho_j' V_j A_j \\ &= -\rho_j^* A_j u_j^* + \rho_{j-1}^* A_{j-1} u_{j-1}^* - \frac{\left(\rho_i - \rho_i^{old}\right)}{\Delta t} V_i \end{aligned} \tag{B.58}$$

The last two terms on the LHS can be neglected because it is two corrections which are multiplied.

$$\rho_j' A_j u_j^* - \frac{(p_{i+1}' - p_i')}{(x_{i+1} - x_i)b_j}\rho_j^* V_j A_j + \frac{(p_i' - p_{i-1}')}{(x_i - x_{i-1})b_{j-1}}\rho_{j-1}^* V_{j-1} A_{j-1} - \rho_{j-1}' A_{j-1} u_{j-1}^*$$
$$= -\rho_j^* A_j u_j^* + \rho_{j-1}^* A_{j-1} u_{j-1}^* - \frac{(\rho_i - \rho_i^{old})}{\Delta t} V_i \qquad \text{(B.59)}$$

### B.3.1 For Positive Flow from Left to Right

Substitute a linear interpolation for the density with flux blending into equation B.59

$$[\rho_i' + \lambda_\rho \sigma_j (\rho_{i+1}' - \rho_i')] A_j u_j^* - \frac{(p_{i+1}' - p_i')}{(x_{i+1} - x_i)b_j}\rho_j^* V_j A_j$$
$$+ \frac{(p_i' - p_{i-1}')}{(x_i - x_{i-1})b_{j-1}}\rho_{j-1}^* V_{j-1} A_{j-1} - [\rho_{i-1}' + \lambda_\rho \sigma_{j-1}(\rho_i' - \rho_{i-1}')] A_{j-1} u_{j-1}^* \qquad \text{(B.60)}$$
$$= -\rho_j^* A_j u_j^* + \rho_{j-1}^* A_{j-1} u_{j-1}^* - \frac{(\rho_i - \rho_i^{old})}{\Delta t} V_i$$

Expanding further

$$(1 - \lambda_\rho \sigma_j)\rho_i' A_j u_j^* + \lambda_\rho \sigma_j \rho_{i+1}' A_j u_j^* - \frac{\rho_j^* V_j A_j}{(x_{i+1} - x_i)b_j} p_{i+1}' + \frac{\rho_j^* V_j A_j}{(x_{i+1} - x_i)b_j} p_i'$$
$$+ \frac{\rho_{j-1}^* V_{j-1} A_{j-1}}{(x_i - x_{i-1})b_{j-1}} p_i' - \frac{\rho_{j-1}^* V_{j-1} A_{j-1}}{(x_i - x_{i-1})b_{j-1}} p_{i-1}' - (1 - \lambda_\rho \sigma_{j-1})\rho_{i-1}' A_{j-1} u_{j-1}^* - \lambda_\rho \sigma_{j-1} \rho_i' A_{j-1} u_{j-1}^*$$

$$= -\rho_j^* A_j u_j^* + \rho_{j-1}^* A_{j-1} u_{j-1}^* - \frac{(\rho_i - \rho_i^{old})}{\Delta t} V_i \qquad \text{(B.61)}$$

Substitute $\rho' = \frac{p'}{RT}$ and rearrange

$$\left[-\frac{\rho^*_{j-1}V_{j-1}A_{j-1}}{(x_i-x_{i-1})b_{j-1}}-(1-\lambda_\rho\sigma_{j-1})\frac{A_{j-1}u^*_{j-1}}{RT_{i-1}}\right]p'_{i-1}+$$
$$\left[\frac{\rho^*_{j-1}V_{j-1}A_{j-1}}{(x_i-x_{i-1})b_{j-1}}-\lambda_\rho\sigma_{j-1}\frac{A_{j-1}u^*_{j-1}}{RT_i}+(1-\lambda_\rho\sigma_j)\frac{A_ju^*_j}{RT_i}+\frac{\rho^*_jV_jA_j}{(x_{i+1}-x_i)b_j}\right]p'_i+ \quad \text{(B.62)}$$
$$\left[\lambda_\rho\sigma_j\frac{A_ju^*_j}{RT_{i+1}}-\frac{\rho^*_jV_jA_j}{(x_{i+1}-x_i)b_j}\right]p'_{i+1}$$
$$=-\rho^*_jA_ju^*_j+\rho^*_{j-1}A_{j-1}u^*_{j-1}-\frac{(\rho_i-\rho_i^{old})}{\Delta t}V_i$$

This can be solved with the Thomas algorithm when it is in the form of $e_ip'_{i-1}+f_ip'_i+g_ip'_{i+1}=h_i$

with the coefficients

$$e_i=-\frac{\rho^*_{j-1}V_{j-1}A_{j-1}}{(x_i-x_{i-1})b_{j-1}}-(1-\lambda_\rho\sigma_{j-1})\frac{A_{j-1}u^*_{j-1}}{RT_{i-1}}$$
$$f_i=\frac{\rho^*_{j-1}V_{j-1}A_{j-1}}{(x_i-x_{i-1})b_{j-1}}-\lambda_\rho\sigma_{j-1}\frac{A_{j-1}u^*_{j-1}}{RT_i}+(1-\lambda_\rho\sigma_j)\frac{A_ju^*_j}{RT_i}+\frac{\rho^*_jV_jA_j}{(x_{i+1}-x_i)b_j} \quad \text{(B.63)}$$
$$g_i=\lambda_\rho\sigma_j\frac{A_ju^*_j}{RT_{i+1}}-\frac{\rho^*_jV_jA_j}{(x_{i+1}-x_i)b_j}$$
$$h_i=-\rho^*_jA_ju^*_j+\rho^*_{j-1}A_{j-1}u^*_{j-1}-\frac{(\rho_i-\rho_i^{old})}{\Delta t}V_i$$

### B.3.2 For Negative Flow from Right to Left:

Substitute a linear interpolation for the density with flux blending into equation B.59

$$\left[\rho'_{i+1}+\lambda_\rho\varepsilon_j(\rho'_{i+1}-\rho'_i)\right]A_ju^*_j-\frac{(p'_{i+1}-p'_i)}{(x_{i+1}-x_i)b_j}\rho^*_jV_jA_j$$
$$+\frac{(p'_i-p'_{i-1})}{(x_i-x_{i-1})b_{j-1}}\rho^*_{j-1}V_{j-1}A_{j-1}-\left[\rho'_i+\lambda_\rho\varepsilon_{j-1}(\rho'_i-\rho'_{i-1})\right]A_{j-1}u^*_{j-1} \quad \text{(B.64)}$$
$$=-\rho^*_jA_ju^*_j+\rho^*_{j-1}A_{j-1}u^*_{j-1}-\frac{(\rho_i-\rho_i^{old})}{\Delta t}V_i$$

Expanding further

$$
\begin{aligned}
&\left(1+\lambda_\rho\varepsilon_j\right)\rho'_{i+1}A_j u^*_j - \lambda_\rho\varepsilon_j\rho'_i A_j u^*_j - \frac{\rho^*_j V_j A_j}{(x_{i+1}-x_i)b_j}p'_{i+1} \\
&+\frac{\rho^*_j V_j A_j}{(x_{i+1}-x_i)b_j}p'_i + \frac{\rho^*_{j-1}V_{j-1}A_{j-1}}{(x_i-x_{i-1})b_{j-1}}p'_i - \frac{\rho^*_{j-1}V_{j-1}A_{j-1}}{(x_i-x_{i-1})b_{j-1}}p'_{i-1} \\
&-\left(1+\lambda_\rho\varepsilon_{j-1}\right)\rho'_i A_{j-1}u^*_{j-1} + \lambda_\rho\varepsilon_{j-1}\rho'_{i-1}A_{j-1}u^*_{j-1} \\
&= -\rho^*_j A_j u^*_j + \rho^*_{j-1}A_{j-1}u^*_{j-1} - \frac{\left(\rho_i-\rho_i^{old}\right)}{\Delta t}V_i
\end{aligned}
\tag{B.65}
$$

Substitute $\rho' = \dfrac{p'}{RT}$ and rearrange

$$
\begin{aligned}
&\left[\lambda_\rho\varepsilon_{j-1}\frac{u^*_{j-1}A_{j-1}}{RT_{i-1}} - \frac{\rho^*_{j-1}V_{j-1}A_{j-1}}{b_{j-1}(x_i-x_{i-1})}\right]p'_{i-1} + \\
&\left[-\left(1+\lambda_\rho\varepsilon_{j-1}\right)\frac{u^*_{j-1}A_{j-1}}{RT_i} + \frac{\rho^*_{j-1}V_{j-1}A_{j-1}}{b_{j-1}(x_i-x_{i-1})} - \lambda_\rho\varepsilon_j\frac{u^*_j A_j}{RT_i} + \frac{\rho^*_j V_j A_j}{b_j(x_{i+1}-x_i)}\right]p'_i + \\
&\left[\left(1+\lambda_\rho\varepsilon_j\right)\frac{u^*_j A_j}{RT_{i+1}} - \frac{\rho^*_j V_j A_j}{b_j(x_{i+1}-x_i)}\right]p'_{i+1} \\
&= -\rho^*_j u^*_j A_j + \rho^*_{j-1}u^*_{j-1}A_{j-1} - \frac{\left(\rho_i-\rho_i^{old}\right)}{\Delta t}V_i
\end{aligned}
\tag{B.66}
$$

This can be solved with the Thomas algorithm when it is in the form of

$$e_i p'_{i-1} + f_i p'_i + g_i p'_{i+1} = h_i$$

with the coefficients

$$
\begin{aligned}
e_i &= \lambda_\rho\varepsilon_{j-1}\frac{u^*_{j-1}A_{j-1}}{RT_{i-1}} - \frac{\rho^*_{j-1}V_{j-1}A_{j-1}}{b_{j-1}(x_i-x_{i-1})} \\
f_i &= -\left(1+\lambda_\rho\varepsilon_{j-1}\right)\frac{u^*_{j-1}A_{j-1}}{RT_i} + \frac{\rho^*_{j-1}V_{j-1}A_{j-1}}{b_{j-1}(x_i-x_{i-1})} - \lambda_\rho\varepsilon_j\frac{u^*_j A_j}{RT_i} + \frac{\rho^*_j V_j A_j}{b_j(x_{i+1}-x_i)} \\
g_i &= \left(1+\lambda_\rho\varepsilon_j\right)\frac{u^*_j A_j}{RT_{i+1}} - \frac{\rho^*_j V_j A_j}{b_j(x_{i+1}-x_i)} \\
h_i &= -\rho^*_j u^*_j A_j + \rho^*_{j-1}u^*_{j-1}A_{j-1} - \frac{\left(\rho_i-\rho_i^{old}\right)}{\Delta t}V_i
\end{aligned}
\tag{B.67}
$$

It can be seen that the right hand sides of equations B.62 and B.66 are actually the continuity equation and that the pressure correction would be zero if continuity is satisfied.

### B.3.3 Left Hand Boundary Conditions

Substitute the left hand boundary conditions into equation B.55

$$\rho_1^j u_1 A_1^j - \rho_{left} u_{left} A_{left} = -\frac{\left(\rho_1 - \rho_1^{old}\right)}{\Delta t} V_1 \tag{B.68}$$

Substitute the velocities $u_{left}$ and $u_1$ into equation B.51

$$u_1 = u_1^* + \frac{d_1'}{b_1} \tag{B.69}$$

$$u_{left} = u_{left}^* + \frac{d_{left}'}{b_{left}} \tag{B.70}$$

Substituting B.69 and B.70 into B.68

$$\rho_1^j A_1^j \left(u_1^* + \frac{d_1'}{b_1}\right) - \rho_{left} A_{left} \left(u_{left}^* + \frac{d_{left}'}{b_{left}}\right) = -\frac{\left(\rho_1 - \rho_1^{old}\right)}{\Delta t} V_1 \tag{B.71}$$

Substituting the density correction $\rho_1^j = \rho_1^{*j} + \rho_1'^j$

$$\left(\rho_1^{*j} + \rho_1'^j\right) A_1^j \left(u_1^* + \frac{d_1'}{b_1}\right) - \rho_{left} A_{left} \left(u_{left}^* + \frac{d_{left}'}{b_{left}}\right) = -\frac{\left(\rho_1 - \rho_1^{old}\right)}{\Delta t} V_1 \tag{B.72}$$

Substituting $d_1'$ and $d_{left}'$ from equation B.49

$$\left(\rho_1^{*j} + \rho_1'^j\right) A_1^j \left(u_1^* - \frac{\left(p_2' - p_1'\right) V_1^j}{\left(x_2 - x_1\right) b_1}\right) - \rho_{left} A_{left} \left(u_{left}^* - \frac{\left(p_1' - p_{left}'\right) V_{left}}{\left(x_1 - x_{left}\right) b_{left}}\right) = -\frac{\left(\rho_1 - \rho_1^{old}\right)}{\Delta t} V_1 \tag{B.73}$$

The pressure correction on the left hand boundary $p'_{left}$ is equal to zero. Cancelling the product of the two corrections and rearrange .

$$\rho_1'^j A_1^j u_1^* - \frac{\rho_1^{*j} A_1^j V_1^j}{(x_2 - x_1)b_1} p_2' + \frac{\rho_1^{*j} A_1^j V_1^j}{(x_2 - x_1)b_1} p_1' + \frac{\rho_{left} A_{left} V_{left}}{(x_1 - x_{left})b_{left}} p_1' = -\rho_1^{*j} A_1^j u_1^* + \rho_{left} A_{left} u_{left}^* - \frac{(\rho_1 - \rho_1^{old})}{\Delta t} V_1 \quad \text{(B.74)}$$

*For positive flow from left to right:*

Taking a linear interpolation for the density correction with flux blending, substitute $\rho' = \frac{p'}{RT}$ into equation B.74 and rearrange

$$\left[(1 - \lambda_\rho \sigma_1)\frac{A_1^j u_1^*}{RT_1} + \frac{\rho_1^{*j} A_1^j V_1^j}{(x_2 - x_1)b_1} + \frac{\rho_{left} A_{left} V_{left}}{(x_1 - x_{left})b_{left}}\right] p_1' + \left[\lambda_\rho \sigma_1 \frac{A_1^j u_1^*}{RT_2} - \frac{\rho_1^{*j} A_1^j V_1^j}{(x_2 - x_1)b_1}\right] p_2' = -\rho_1^{*j} A_1^j u_1^* + \rho_{left} A_{left} u_{left}^* - \frac{(\rho_1 - \rho_1^{old})}{\Delta t} V_1 \quad \text{(B.75)}$$

*For negative flow from right to left:*

Taking a linear interpolation for the density correction with flux blending, substitute $\rho' = \frac{p'}{RT}$ into equation B.74 and rearrange

$$\left[-\lambda_\rho \varepsilon_1 \frac{A_1^j u_1^*}{RT_1} + \frac{\rho_1^{*j} A_1^j V_1^j}{(x_2 - x_1)b_1} + \frac{\rho_{left} A_{left} V_{left}}{(x_1 - x_{left})b_{left}}\right] p_1' + \left[-\frac{\rho_1^{*j} A_1^j V_1^j}{(x_2 - x_1)b_1} + (1 + \lambda_\rho \varepsilon_1)\frac{A_1^j u_1^*}{RT_2}\right] p_2' = -\rho_1^{*j} A_1^j u_1^* + \rho_{left} A_{left} u_{left}^* - \frac{(\rho_1 - \rho_1^{old})}{\Delta t} V_1 \quad \text{(B.76)}$$

### B.3.4 Right Hand Boundary Conditions

Substitute the boundary conditions into equation B.55

$$\rho_{right} u_{right} A_{right} - \rho_{j-1} u_{j-1} A_{j-1} = -\frac{\left(\rho_n - \rho_n^{old}\right)}{\Delta t} V_n \tag{B.77}$$

Substitute the velocities $u_{right}$ and $u_{n-1}$ into equation B.51

$$u_{n-1} = u^*_{n-1} + \frac{d'_{n-1}}{b_{n-1}} \tag{B.78}$$

$$u_{right} = u^*_{right} + \frac{d'_{right}}{b_{right}} \tag{B.79}$$

Substituting B.78 and B.79 into B.77

$$\rho_{right} A_{right} \left( u^*_{right} + \frac{d'_{right}}{b_{right}} \right) - \rho^j_{n-1} A^j_{n-1} \left( u^*_{n-1} + \frac{d'_{n-1}}{b_{n-1}} \right) = -\frac{\left(\rho_n - \rho_n^{old}\right)}{\Delta t} V_n \tag{B.80}$$

Substituting the density correction $\rho^j_{n-1} = \rho^{*j}_{n-1} + \rho'^j_{n-1}$

$$\rho_{right} A_{right} \left( u^*_{right} + \frac{d'_{right}}{b_{right}} \right) - \left(\rho^{*j}_{n-1} + \rho'^j_{n-1}\right) A^j_{n-1} \left( u^*_{n-1} + \frac{d'_{n-1}}{b_{n-1}} \right) = -\frac{\left(\rho_n - \rho_n^{old}\right)}{\Delta t} V_n \tag{B.81}$$

Substituting $d'_{n-1}$ and $d'_{right}$ from equation B.49

$$\rho_{right} A_{right} \left( u^*_{right} - \frac{\left(p'_{right} - p'_n\right) V_{right}}{\left(x_{right} - x_n\right) b_{right}} \right) - \left(\rho^{*j}_{n-1} + \rho'^j_{n-1}\right) A^j_{n-1} \left( u^*_{n-1} - \frac{\left(p'_n - p'_{n-1}\right) V^j_{n-1}}{\left(x_n - x_{n-1}\right) b_{n-1}} \right) = -\frac{\left(\rho_n - \rho_n^{old}\right)}{\Delta t} V_n \tag{B.82}$$

The pressure correction on the right hand boundary $p'_{right}$ is equal to zero. Cancelling the product of the two corrections and rearrange

$$\frac{\rho_{right}A_{right}V_{right}}{(x_{right}-x_n)b_{right}}p'_n-\rho'^{j}_{n-1}A^j_{n-1}u^*_{n-1}+\frac{\rho^{*j}_{n-1}A^j_{n-1}V^j_{n-1}}{(x_n-x_{n-1})b_{n-1}}p'_n-\frac{\rho^{*j}_{n-1}A^j_{n-1}V^j_{n-1}}{(x_n-x_{n-1})b_{n-1}}p'_{n-1}$$
$$=-\rho_{right}A_{right}u^*_{right}+\rho^{*j}_{n-1}A^j_{n-1}u^*_{n-1}-\frac{(\rho_n-\rho_n^{old})}{\Delta t}V_n \qquad \text{(B.83)}$$

*Positive flow from left to right:*

Taking a linear interpolation for the density correction with flux blending, substitute $\rho' = \frac{p'}{RT}$ into equation B.83 and rearrange

$$\left[-(1-\lambda_\rho\sigma_{n-1})\frac{A^j_{n-1}u^*_{n-1}}{RT_{n-1}}-\frac{\rho^{*j}_{n-1}A^j_{n-1}V^j_{n-1}}{(x_n-x_{n-1})b_{n-1}}\right]p'_{n-1}+$$
$$\left[\frac{\rho^{*j}_{n-1}A^j_{n-1}V^j_{n-1}}{(x_n-x_{n-1})b_{n-1}}+\frac{\rho_{right}A_{right}V_{right}}{(x_{right}-x_n)b_{right}}-\lambda_\rho\sigma_{n-1}\frac{A^j_{n-1}u^*_{n-1}}{RT_n}\right]p'_n \qquad \text{(B.84)}$$
$$=-\rho_{right}A_{right}u^*_{right}+\rho^{*j}_{n-1}A^j_{n-1}u^*_{n-1}-\frac{(\rho_n-\rho_n^{old})}{\Delta t}V_n$$

*Negative flow from right to left:*

Taking a linear interpolation for the density correction with flux blending, substitute $\rho' = \frac{p'}{RT}$ into equation B.83 and rearrange

$$\left[\lambda_\rho\varepsilon_{n-1}\frac{A^j_{n-1}u^*_{n-1}}{RT_{n-1}}-\frac{\rho^{*j}_{n-1}A^j_{n-1}V^j_{n-1}}{(x_n-x_{n-1})b_{n-1}}\right]p'_{n-1}+$$
$$\left[\frac{\rho^{*j}_{n-1}A^j_{n-1}V^j_{n-1}}{(x_n-x_{n-1})b_{n-1}}+\frac{\rho_{right}A_{right}V_{right}}{(x_{right}-x_n)b_{right}}-(1+\lambda_\rho\varepsilon_{n-1})\frac{A^j_{n-1}u^*_{n-1}}{RT_n}\right]p'_n \qquad \text{(B.85)}$$
$$=-\rho_{right}A_{right}u^*_{right}+\rho^{*j}_{n-1}A^j_{n-1}u^*_{n-1}-\frac{(\rho_n-\rho_n^{old})}{\Delta t}V_n$$

### B.3.5 Velocity Correction

From equation B.48 we can also derive the velocity correction equation. Substitute $d_1^{'}$ in equation B.48

$$u_j^{'} = -\frac{(p_{i+1}^{'} - p_i^{'})V_j}{(x_{i+1} - x_i)b_j} \tag{B.86}$$

Left hand boundary condition

$$u_{left}^{'} = -\frac{p_1^{'}V_{left}}{(x_1 - x_{left})b_{left}} \tag{B.87}$$

Right hand boundary condition

$$u_{right}^{'} = \frac{p_n^{'}V_{right}}{(x_{right} - x_n)b_{right}} \tag{B.88}$$

## B.4 Conservation of Energy for the Gas

The energy equation for the gas (equation A.19) as derived in Appendix A is repeated in equation B90. This equation will now be discretized and the flow area of the gas $A_f$ will be depicted as $A$.

$$\begin{aligned}(c_p - R)\rho\frac{\partial T}{\partial t} &= -c_p\frac{\partial \rho u T}{\partial x} + \frac{\partial}{\partial x}\left(k\frac{\partial T}{\partial x}\right) \\ -(c_p - R)T\frac{\partial \rho}{\partial t} &- \frac{S_{in}h_{in}}{V}(T - T_t) - \frac{A_w h_m}{V}(T - T_m)\end{aligned} \tag{B.89}$$

Integrate over the volume at point $i$. The velocity $u$ and density $\rho$ is constant over the control volume

$$\begin{aligned}(c_p - R)\int_V \rho\frac{\partial T}{\partial t}dV &= -c_p\int_V \frac{\partial \rho u T}{\partial x}dV + k\int_V \frac{\partial}{\partial x}\left(\frac{\partial T}{\partial x}\right)dV - (c_p - R)\int_V T\frac{\partial \rho}{\partial t}dV \\ -\frac{Sh_{in}}{V}\int_V (T - T_t)dV &- \frac{A_w h_m}{V}\int_V (T - T_m)dV\end{aligned} \tag{B.90}$$

Applying the Gauss theorem (Finney and Thomas, 1990)

$$\begin{aligned}&(c_p - R)\int_V \rho \frac{\partial T}{\partial t} dV = -c_p \int_A \rho \bar{U} T \cdot \bar{n} dA + k \int_A \nabla T \cdot \bar{n} dA - (c_p - R)\int_V T \frac{\partial \rho}{\partial t} dV \\ &- \frac{Sh_{in}}{V}\int_V (T - T_t) dV - \frac{A_w h_m}{V}\int_V (T - T_m) dV\end{aligned} \tag{B.91}$$

Integrate over the boundaries

$$\begin{aligned}&(c_p - R)\frac{\rho_i V_i}{\Delta t}\left(T_i - T_i^{old}\right) = -c_p \rho_j u_j T_j A_j + c_p \rho_{j-1} u_{j-1} T_{j-1} A_{j-1} \\ &+ k\left(\frac{\Delta T}{\Delta x}\right)_j A_j - k\left(\frac{\Delta T}{\Delta x}\right)_{j-1} A_{j-1} - (c_p - R)\frac{V_i}{\Delta t}\left(\rho_i - \rho_i^{old}\right) T_i \\ &- S_i h_i^{in}\left(T_i - T_i^t\right) - A_i^w h_i^m \left(T_i - T_i^m\right)\end{aligned} \tag{B.92}$$

Simplifying

$$\begin{aligned}&(c_p - R)\left(2\rho_i - \rho_i^{old}\right)\frac{V_i}{\Delta t} T_i = -c_p \rho_j u_j T_j A_j + c_p \rho_{j-1} u_{j-1} T_{j-1} A_{j-1} \\ &+ k\left(\frac{\Delta T}{\Delta x}\right)_j A_j - k\left(\frac{\Delta T}{\Delta x}\right)_{j-1} A_{j-1} + (c_p - R)\frac{V_i}{\Delta t}\rho_i T_i^{old} \\ &- S_i h_i^{in}\left(T_i - T_i^t\right) - A_i^w h_i^m \left(T_i - T_i^m\right)\end{aligned} \tag{B.93}$$

### B.4.1 For Positive Flow from Left to Right

Introducing a flux blending factor $\lambda_T$ for the linear interpolation and taking central differencing for the temperature gradients on the control volume boundaries

$$\begin{aligned}&(c_p - R)\left(2\rho_i - \rho_i^{old}\right)\frac{V_i}{\Delta t} T_i + c_p \rho_j u_j A_j \left[T_i + \lambda_T \sigma_j \left(T_{i+1} - T_i\right)\right] \\ &- c_p \rho_{j-1} u_{j-1} A_{j-1}\left[T_{i-1} + \lambda_T \sigma_{j-1}\left(T_i - T_{i-1}\right)\right] \\ &- k\frac{\left(T_{i+1} - T_i\right)}{\left(x_{i+1} - x_i\right)} A_j + k\frac{\left(T_i - T_{i-1}\right)}{\left(x_i - x_{i-1}\right)} A_{j-1} \\ &= (c_p - R)\frac{V_i}{\Delta t}\rho_i T_i^{old} - S_i h_i^{in}\left(T_i - T_i^t\right) - A_i^w h_i^m \left(T_i - T_i^m\right)\end{aligned} \tag{B.94}$$

Expanding further

$$
\begin{aligned}
&-c_p\rho_{j-1}u_{j-1}A_{j-1}\left(1-\lambda_T\sigma_{j-1}\right)T_{i-1}-\frac{kA_{j-1}}{\left(x_i-x_{i-1}\right)}T_{i-1}\\
&+\left(c_p-R\right)\frac{V_i}{\Delta t}\left(2\rho_i-\rho_i^{old}\right)T_i+c_p\rho_j u_j A_j\left(1-\lambda_T\sigma_j\right)T_i-c_p\rho_{j-1}u_{j-1}A_{j-1}\lambda_T\sigma_{j-1}T_i\\
&+\frac{kA_j}{\left(x_{i+1}-x_i\right)}T_i+\frac{kA_{j-1}}{\left(x_i-x_{i-1}\right)}T_i+A_i^w h_i^m T_i+S_i h_i^{in}T_i+c_p\rho_j u_j A_j\lambda_T\sigma_j T_{i+1}-\frac{kA_j}{\left(x_{i+1}-x_i\right)}T_{i+1}\\
&=\left(c_p-R\right)\frac{V_i}{\Delta t}\rho_i T_i^{old}+S_i h_i^{in}T_i^t+A_i^w h_i^m T_i^m
\end{aligned}
\tag{B.95}
$$

The coefficients of the tri-diagonal matrix are

$$
\begin{aligned}
a_i &= -c_p\rho_{j-1}u_{j-1}A_{j-1}\left(1-\lambda_T\sigma_{j-1}\right)-\frac{kA_{j-1}}{\left(x_i-x_{i-1}\right)}\\
b_i &= \left(c_p-R\right)\frac{V_i}{\Delta t}\left(2\rho_i-\rho_i^{old}\right)+c_p\rho_j u_j A_j\left(1-\lambda_T\sigma_j\right)-c_p\rho_{j-1}u_{j-1}A_{j-1}\lambda_T\sigma_{j-1}\\
&\quad+\frac{kA_j}{\left(x_{i+1}-x_i\right)}+\frac{kA_{j-1}}{\left(x_i-x_{i-1}\right)}+A_i^w h_i^m+S_i h_i^{in}\\
c_i &= c_p\rho_j u_j A_j\lambda_T\sigma_j-\frac{kA_j}{\left(x_{i+1}-x_i\right)}\\
d_i &= \left(c_p-R\right)\frac{V_i}{\Delta t}\rho_i T_i^{old}+S_i h_i^{in}T_i^t+A_i^w h_i^m{}_i T_i^m
\end{aligned}
\tag{B.96}
$$

*Left hand boundary conditions:*

$$
\begin{aligned}
b_1 &= \left(c_p-R\right)\frac{V_1}{\Delta t}\left(2\rho_1-\rho_1^{old}\right)+c_p\rho_1^j u_1 A_1^j\left(1-\lambda_T\sigma_1\right)\\
&\quad+\frac{kA_1^j}{\left(x_2-x_1\right)}+\frac{kA_{left}}{2\left(x_1-x_{left}\right)}+A_1^w h_1^m+S_1 h_1^{in}\\
c_1 &= c_p\rho_1^j u_1 A_1^j\lambda_T\sigma_1-\frac{kA_1^j}{\left(x_2-x_1\right)}\\
d_1 &= \left(c_p-R\right)\frac{V_1}{\Delta t}\rho_1 T_1^{old}+S_1 h_1^{in}T_1^t+A_1^w h_1^m T_1^m+c_p\rho_{left}u_{left}A_{left}T_{left}+\frac{kA_{left}}{2\left(x_1-x_{left}\right)}T_{left}
\end{aligned}
\tag{B.97}
$$

*Right hand boundary conditions:*

The temperature at the right hand boundary is not known for positive flow. Substitute the linear interpolation for the temperature on the right hand boundary

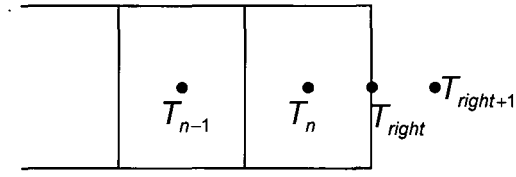


***Figure B.8*** *Grid at right hand boundary for temperature*

$$\left(\frac{\Delta T}{\Delta x}\right)_{right} = \frac{\left(T_{right+1} - T_n\right)}{\left(x_{right+1} - x_n\right)} \tag{B.98}$$

Substitute $\left(x_{right+1} - x_n\right) = 2\left(x_{right} - x_n\right)$ and $T_{right+1} = T_{right}$

$$\left(\frac{\Delta T}{\Delta x}\right)_{right} = \frac{\left(T_{right} - T_n\right)}{2\left(x_{right} - x_n\right)} \tag{B.99}$$

Substitute into equation and taking a linear interpolation with a flux blending factor for the temperature at the velocity interface

$$\begin{aligned}
&\left(c_p - R\right)\left(2\rho_n - \rho_n^{old}\right)\frac{V_n}{\Delta t}T_n + c_p\rho_{right}u_{right}A_{right}T_{right} \\
&- c_p\rho_{n-1}^{j}u_{n-1}^{j}A_{n-1}^{j}\left[T_{n-1} + \lambda_T\sigma_{n-1}\left(T_n - T_{n-1}\right)\right] \\
&- k\frac{\left(T_{right} - T_n\right)}{2\left(x_{right} - x_n\right)}A_{right} + k\frac{\left(T_n - T_{n-1}\right)}{\left(x_n - x_{n-1}\right)}A_{n-1}^{j} \\
&= \left(c_p - R\right)\frac{V_n}{\Delta t}\rho_n T_n^{old} - S_n h_n^{in}\left(T_n - T_n^{t}\right) - A_n^{w}h_n^{m}\left(T_n - T_n^{m}\right)
\end{aligned} \tag{B.100}$$

Von Neumann boundary condition is used for the temperature in the $\rho uT$ term at the right hand boundary and $T_{right}$ is substituted as

$$T_{right} = T_n\left[1 + \frac{\left(x_{right} - x_n\right)}{\left(x_n - x_{n-1}\right)}\right] - \frac{\left(x_{right} - x_n\right)}{\left(x_n - x_{n-1}\right)}T_{n-1} \tag{B.101}$$

Substitute $T_{right}$ into equation B78 and rearrange

$$a_n = -c_p\rho_{right}u_{right}A_{right}\frac{(x_{right}-x_n)}{(x_n-x_{n-1})} - c_p\rho_{n-1}^j u_{n-1}^j A_{n-1}^j(1-\lambda_T\sigma_{n-1}) + \frac{k(A_{right}-2A_{n-1}^j)}{2(x_n-x_{n-1})}$$

$$b_n = (c_p-R)(2\rho_n-\rho_n^{old})\frac{V_n}{\Delta t} + c_p\rho_{right}u_{right}A_{right}\left[1+\frac{(x_{right}-x_n)}{(x_n-x_{n-1})}\right]$$

$$- c_p\rho_{n-1}^j u_{n-1}^j A_{n-1}^j\lambda_T\sigma_{n-1} - \frac{k(A_{right}-2A_{n-1}^j)}{2(x_n-x_{n-1})} + S_n h_n^{in} + A_n^w h_n^m$$

$$d_n = (c_p-R)\frac{V_n}{\Delta t}\rho_n T_n^{old} + S_n h_n^{in} T_n^t + A_n^w h_n^m T_n^m$$

(B.102)

It is clear from the equation above that the conduction terms cancel out when $A_{n-1}^j = A_{right}$

### B.4.2 For Negative Flow from Right to Left

Using linear interpolation for the temperature and introducing a flux blending factor $\lambda_T$

$$\begin{aligned}&(c_p-R)(2\rho_i-\rho_i^{old})\frac{V_i}{\Delta t}T_i + c_p\rho_j u_j A_j\left[T_{i+1}+\lambda_T\varepsilon_j(T_{i+1}-T_i)\right]\\&- c_p\rho_{j-1}u_{j-1}A_{j-1}\left[T_i+\lambda_T\varepsilon_{j-1}(T_i-T_{i-1})\right]\\&- k\frac{(T_{i+1}-T_i)}{(x_{i+1}-x_i)}A_j + k\frac{(T_i-T_{i-1})}{(x_i-x_{i-1})}A_{j-1}\\&= (c_p-R)\frac{V_i}{\Delta t}\rho_i T_i^{old} - S_i h_i^{in}(T_i-T_i^t) - A_i^w h_i^m(T_i-T_i^m)\end{aligned} \qquad \text{(B.103)}$$

Expanding further

$$c_p\rho_{j-1}u_{j-1}A_{j-1}\lambda_T\varepsilon_{j-1}T_{i-1} - \frac{kA_{j-1}}{(x_i - x_{i-1})}T_{i-1}$$
$$+ (c_p - R)(2\rho_i - \rho_i^{old})\frac{V_i}{\Delta t}T_i - c_p\rho_{j-1}u_{j-1}A_{j-1}(1+\lambda_T\varepsilon_{j-1})T_i - c_p\rho_j u_j A_j\lambda_T\varepsilon_j T_i$$
$$+ \frac{kA_j}{(x_{i+1} - x_i)}T_i + \frac{kA_{j-1}}{(x_i - x_{i-1})}T_i + A_i^w h_i^m T_i + S_i h_i^{in} T_i + c_p\rho_j u_j A_j(1+\lambda_T\varepsilon_j)T_{i+1} - \frac{kA_j}{(x_{i+1} - x_i)}T_{i+1}$$
$$= (c_p - R)\frac{V_i}{\Delta t}\rho_i T_i^{old} + S_i h_i^{in} T_i^t + A_i^w h_i^m T_i^m$$
(B.104)

The coefficients of the tri-diagonal matrix are:

$$a_i = c_p\rho_{j-1}u_{j-1}A_{j-1}\lambda_T\varepsilon_{j-1} - \frac{kA_{j-1}}{(x_i - x_{i-1})}$$
$$b_i = (c_p - R)(2\rho_i - \rho_i^{old})\frac{V_i}{\Delta t} - c_p\rho_{j-1}u_{j-1}A_{j-1}(1+\lambda_T\varepsilon_{j-1}) - c_p\rho_j u_j A_j\lambda_T\varepsilon_j$$
$$+ \frac{kA_j}{(x_{i+1} - x_i)} + \frac{kA_{j-1}}{(x_i - x_{i-1})} + A_i^w h_i^m T_i + S_i h_i^{in} \qquad \text{(B.105)}$$
$$c_i = c_p\rho_j u_j A_j(1+\lambda_T\varepsilon_j) - \frac{kA_j}{(x_{i+1} - x_i)}$$
$$d_i = (c_p - R)\frac{V_i}{\Delta t}\rho_i T_i^{old} + S_i h_i^{in} T_i^t + A_i^w h_i^m T_i^m$$

*Left hand boundary conditions:*

The temperature at the left hand boundary is not known for negative flow. Substitute the linear interpolation for the temperature on the left hand boundary

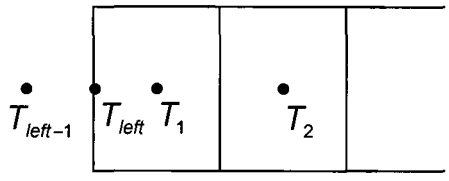


***Figure B.9*** *Grid at left hand boundary for temperature*

$$\left(\frac{\Delta T}{\Delta x}\right)_{left} = \frac{(T_1 - T_{left-1})}{(x_1 - x_{left-1})} \qquad \text{(B.106)}$$

Substitute $(x_1 - x_{left-1}) = 2(x_1 - x_{left})$ and $T_{left-1} = T_{left}$

$$\left(\frac{\Delta T}{\Delta x}\right)_{left} = \frac{(T_1 - T_{left})}{2(x_1 - x_{left})} \tag{B.107}$$

Substitute into equation and taking a linear interpolation with a flux blending factor for the temperature at the velocity interface

$$\begin{aligned}&(c_p - R)(2\rho_1 - \rho_i^{old})\frac{V_1}{\Delta t}T_1 + c_p\rho_1^j u_1 A_1^j [T_2 + \lambda_T \varepsilon_1 (T_2 - T_1)] - c_p \rho_{left} u_{left} A_{left} T_{left} \\ &- k\frac{(T_2 - T_2)}{(x_2 - x_1)}A_1^j + k\frac{(T_1 - T_{left})}{2(x_1 - x_{left})}A_{left} \\ &= (c_p - R)\frac{V_1}{\Delta t}\rho_1 T_1^{old} - S_1 h_1^{in}(T_1 - T_1^t) - A_1^w h_1^m (T_1 - T_1^m)\end{aligned} \tag{B.108}$$

Substitute $T_{left}$ into equation B82 and rearrange

$$T_{left} = T_1\left[1 + \frac{(x_1 - x_{left})}{(x_2 - x_1)}\right] - \frac{(x_1 - x_{left})}{(x_2 - x_1)}T_2 \tag{B.109}$$

The coefficients of the tri-diagonal matrix are

$$\begin{aligned}b_1 &= (c_p - R)(2\rho_1 - \rho_i^{old})\frac{V_1}{\Delta t} - c_p\rho_1^j u_1 A_1^j \lambda_T \varepsilon_1 + \frac{k(A_{left} - 2A_1^j)}{2(x_2 - x_1)} \\ &\quad - c_p \rho_{left} u_{left} A_{left}\left[1 + \frac{(x_1 - x_{left})}{(x_2 - x_1)}\right] + S_1 h_1^{in} + A_1^w h_1^m \\ c_1 &= \frac{k(A_{left} - 2A_1^j)}{2(x_2 - x_1)} + c_p\rho_1^j u_1 A_1^j (1 + \lambda_T \varepsilon_1) + c_p \rho_{left} u_{left} A_{left}\frac{(x_1 - x_{left})}{(x_2 - x_1)} \\ d_1 &= (c_p - R)\frac{V_1}{\Delta t}\rho_1 T_1^{old} + S_1 h_1^{in} T_1^t + A_1^w h_1^m T_1^m\end{aligned} \tag{B.110}$$

*Right hand boundary conditions:*

The temperature on the right hand boundary $T_{right}$ is known

$$a_n = -\frac{kA_{j-1}}{(x_n - x_{n-1})} + c_p \rho_{n-1}^{j} u_{n-1} A_{n-1}^{j} \lambda_T \varepsilon_{n-1}$$

$$b_n = (c_p - R)(2\rho_n - \rho_n^{old})\frac{V_n}{\Delta t} - c_p \rho_{n-1}^{j} u_{n-1} A_{n-1}^{j}(1 + \lambda_T \varepsilon_{n-1}) + \frac{kA_{right}}{2(x_{right} - x_n)} + \frac{kA_{j-1}}{(x_n - x_{n-1})} + S_n h_n^{in} + A_n^{w} h_n^{m} \quad \text{(B.111)}$$

$$d_n = (c_p - R)\frac{V_n}{\Delta t}\rho_n T_n^{old} + S_n h_n^{in} T_n^{t} + A_n^{w} h_n^{m} T_n^{m} - c_p \rho_{right} u_{right} A_{right} T_{right} + \frac{kA_{right}}{2(x_{right} - x_n)} T_{right}$$

## B.5 Conservation of Energy for Gas Surroundings

The energy equation for gas surroundings consisting of the tube wall and the mesh matrix (equation A.25) is derived in section Appendix A and is now repeated as equation B.112. The cross sectional area of the tube $A_{c,t}$ will be depicted as $A_t$

$$((1-e_v)\rho_m A_c c_m + \rho_t A_t c_t)\frac{\partial T_{mt}}{\partial t} = k_t A_t \frac{\partial}{\partial x}\left(\frac{\partial T_{mt}}{\partial x}\right) + \pi d_{in} h_{in}(T - T_{mt}) - \pi d_{ex} h_{ex}(T_{mt} - T_{ex}) + \frac{4A_c(1-e_v)}{d_w} h_m (T - T_{mt}) \quad \text{(B.112)}$$

Taking the volume integral at point $i$

$$((1-e_v)\rho_m A_c c_m + \rho_t A_t c_t)\int_V \frac{\partial T_{mt}}{\partial t} dV_{mt} = k_t A_t \int_V \frac{\partial}{\partial x}\left(\frac{\partial T_{mt}}{\partial x}\right) dV_{mt} + \int_V \pi d_{in} h_{in}(T - T_{mt}) dV_{mt} - \int_V \pi d_{ex} h_{ex}(T_{mt} - T_{ex}) dV_{mt} + \int_V \frac{4A_c(1-e_v)}{d_w} h_m (T - T_{mt}) dV_{mt}$$

(B.113)

Applying the Gauss theorem (Finney and Thomas, 1990)

$$\left(\left(1-e_v\right)\rho_m A_c c_m + \rho_t A_t c_t\right)\int_V \frac{\partial T_{mt}}{\partial t} dV_{mt} = k_t A_t \int_V \left(\frac{\partial T_{mt}}{\partial x}\right)\cdot \bar{n} dA$$
$$+ \int_V \pi d_{in} h_{in}\left(T - T_{mt}\right) dV_{mt} - \int_V \pi d_{ex} h_{ex}\left(T_{mt} - T_{ex}\right) dV_{mt} + \int_V \frac{4A_c\left(1-e_v\right)}{d_w} h_m\left(T - T_{mt}\right) dV_{mt}$$

(B.114)

Integrate over the boundaries

$$\left(\left(1-e_i^v\right)\rho_i^m A_i^c c_m + \rho_i^t A_i^t c_t\right)\frac{\left(T_i^{mt} - T_i^{mt,old}\right)}{\Delta t} V_i^{mt} = k_i^t A_i^t A_j^t \left(\frac{\Delta T_{mt}}{\Delta x}\right)_j - k_i^t A_i^t A_{j-1}^t \left(\frac{\Delta T_{mt}}{\Delta x}\right)_{j-1}$$
$$+ \pi d_i^{in} h_i^{in}\left(T_i - T_i^{mt}\right) V_i^{mt} - \pi d_i^{ex} h_i^{ex}\left(T_i^{mt} - T_i^{ex}\right) V_i^{mt} + \frac{4A_i^c\left(1-e_i^v\right)}{d_i^w} h_i^m\left(T_i - T_i^{mt}\right) V_i^{mt}$$

(B.115)

Divide by the volume $V_{mt}$ and expand further

$$\left(\left(1-e_i^v\right)\rho_i^m A_i^c c_m + \rho_i^t A_i^t c_t\right)\frac{\left(T_i^{mt} - T_i^{mt,old}\right)}{\Delta t} = \frac{k_t A_i^t A_j^t}{V_i^{mt}} \frac{\left(T_{i+1}^{mt} - T_i^{mt}\right)}{\left(x_{i+1} - x_i\right)} - \frac{k_t A_i^t A_{j-1}^t}{V_i^{mt}} \frac{\left(T_i^{mt} - T_{i-1}^{mt}\right)}{\left(x_i - x_{i-1}\right)}$$
$$+ \pi d_i^{in} h_i^{in}\left(T_i - T_i^{mt}\right) - \pi d_i^{ex} h_i^{ex}\left(T_i^{mt} - T_i^{ex}\right) + \frac{4A_i^c\left(1-e_i^v\right)}{d_i^w} h_i^m\left(T_i - T_i^{mt}\right)$$

(B.116)

Rearrange

$$-\frac{k_i^t A_i^t A_{j-1}^t}{V_i^{mt}\left(x_i - x_{i-1}\right)} T_{i-1}^{mt} + \frac{\left(\left(1-e_i^v\right)\rho_i^m A_i^c c_m + \rho_i^t A_i^t c_t\right)}{\Delta t} T_i^{mt} + \pi d_i^{in} h_i^{in} T_i^{mt} + \pi d_i^{ex} h_i^{ex} T_i^{mt}$$
$$+ \frac{k_i^t A_i^t A_j^t}{V_i^{mt}\left(x_{i+1} - x_i\right)} T_i^{mt} + \frac{k_i^t A_i^t A_{j-1}^t}{V_i^{mt}\left(x_i - x_{i-1}\right)} T_i^{mt} + \frac{4A_i^c\left(1-e_i^v\right)}{d_i^w} h_i^m T_i^{mt} - \frac{k_i^t A_i^t A_j^t}{V_i^{mt}\left(x_{i+1} - x_i\right)} T_{i+1}^{mt}$$
$$= \frac{\left(\left(1-e_i^v\right)\rho_i^m A_i^c c_m + \rho_i^t A_i^t c_t\right)}{\Delta t} T_i^{mt,old} + \pi d_i^{in} h_i^{in} T_i + \pi d_i^{ex} h_i^{ex} T_i^{ex} + \frac{4A_i^c\left(1-e_i^v\right)}{d_i^w} h_i^m T_i$$

(B.117)